LBL-20295

Picosecond Dynamics of Reactions in the Liquid Phase: Studies of Iodine Photodissociation and Development of New Laser Techniques

Mark Alan Berg

Ph.D. Thesis

LBL--20295

DE86 002895

Lawrence Berkeley Laboratory
University of California
Berkeley, California 94720

September 1985

DISCLAIMER

This report was prepared as an account of work sponsored by an agency of the United States Government. Neither the United States Government nor any agency thereof, nor any of their employees, makes any warranty, express or implied, or assumes any legal liability or responsibility for the accuracy, completeness, or usefulness of any information, apparatus, product, or process disclosed, or represents that its use would not infringe privately owned rights. Reference herein to any specific commercial product, process, or service by trade name, trademark, manufacturer, or otherwise does not necessarily constitute or imply its endorsement, recommendation, or favoring by the United States Government or any agency thereof. The views and opinions of authors expressed herein do not necessarily state or reflect those of the United States Government or any agency thereof.

DISTRIBUTION OF THIS DOCUMENT IS UNLIMITED

Picosecond Dynamics of Reactions in the Liquid Phase: Studies of Iodine Photodissociation and Development of New Laser Techniques

Mark Alan Berg

Abstract

Iodine photodissociation and recombination was studied as a model for processes common to chemical reaction in the liquid phase. Picosecond transient absorption measurements from 1000-295 nm were used to monitor the dynamics in a variety of solvents. Most of the atoms which undergo geminate recombination were found to do so in <15 ps, in agreement with the results of existing molecular dynamics simulations. Vibrational relaxation times vary from ~15 ps near the middle of the ground state well to ~150 ps for complete relaxation to v=0. The prediction of strong resonant vibrational energy transfer to chlorinated methane solvents was not supported, but some evidence for this mechanism was found for alkane solvents. Current theory is unable to explain the large variation (65-2700 ps) of the excited A'-state lifetime in various solvents.

A 10-Hz amplified, synchronously-pumped dye laser used to perform these experiments is described and characterized. Stimulated electronic Raman scattering was used to shift the amplified pulses to the vibrational infrared. Pulses were shifted to 3040-1950 cm^{-1} with a maximum of 11 μJ/pulse. The same technique was also used to shift both broad bandwidth and narrow bandwidth pulses with a much broader tuning range of 3450-900 cm^{-1} and up to 120 μJ/pulse. Difference frequency mixing of a picosecond pulse with a nanosecond dye laser pulse was used

to produce picosecond pulses in the far-infrared (20-200 cm^{-1}). Quantum efficiencies of 0.1-0.3% were observed over the entire frequency range. Features unexplainable with simple non-linear optical theory were observed, in particular large pulse-to-pulse energy fluctuations.

Charles B. Harris.
9/18/85

ACKNOWLEDGEMENTS

Most of this work was done in a close and productive collaboration with Alexander Harris. Charles Harris directed the research described in this thesis and focussed the research on important problems, while allowing the independence needed for a complete education. J. Keenan Brown assisted with the infrared work and developed the computer hardware and software used in many of the experiments. He also provided particularly helpful ideas on the calculation of the transient iodine vibrational distribution from the data. Rosanne Sension gave advice on the calculation of Franck-Condon factors for iodine. Tom Kenny and Paul Richards collaborated in the development of the picosecond far-infrared generation. The National Science Foundation supported this study through a graduate fellowship during 1979-82. This work was also supported in part by the National Science Foundation and the Director, Office of Energy Research, Office of Basic Energy Sciences, Chemical Sciences Division of the U. S. Department of Energy under Contract No. DE-AC03-76SF00098.

TABLE OF CONTENTS

INTRODUCTION..... 1

I. DESIGN AND CHARACTERIZATION OF AN AMPLIFIED SYNCHRONOUSLY-PUMPED DYE LASER

A. Introduction..... 5

B. Amplifier Theory..... 7

C. Detailed Design and Operating Parameters..... 12

D. Characterization..... 18

References..... 24

Figures..... 26

II. IODINE PHOTODISSOCIATION AND RECOMBINATION IN SOLUTION: PICOSECOND DYNAMICS AND COMPARISON TO LIQUID-PHASE REACTION THEORY

A. Introduction..... 35

B. Experimental..... 40

C. Results..... 44

Slow Decays: A'-State Trapping..... 45

Intermediate Decays: X-State Vibrational Dynamics..... 49

Rapid Decays: B-State Predissociation Dynamics..... 52

Separation of Absorption Components..... 54

Summary of the Model..... 56

D. Comparison to Previous Results..... 58

E. Comparison with Theoretical Models..... 62

Recombination Dynamics..... 63

Vibrational Relaxation: Classical Analysis and the Relaxation Mechanism..... 65

Vibrational Relaxation: Quantum Spectral Analysis..... 70

Lifetime of the A' State..... 74

Predissociation..... 76

F. Conclusion..... 78

Appendix A. Subtraction of the A'-State Absorption..... 80

Appendix B. Transition Strength Calculations..... 80

Appendix C. Vibrational Population Distribution Calculation..... 102

References..... 110

Tables..... 117

Figures..... 120

III. GENERATION OF PICOSECOND AND NANOSECOND PULSES IN THE VIBRATIONAL INFRARED BY STIMULATED ELECTRONIC RAMAN SCATTERING IN CESIUM VAPOR

A. Introduction..... 147

B. Narrowband Nanosecond Pulses..... 150

C. Broadband Nanosecond Pulses..... 152

D. Picosecond Pulses..... 154

References..... 157

Figures..... 160

IV. GENERATION OF PICOSECOND PULSES IN THE FAR-INFRARED BY DIFFERENCE FREQUENCY MIXING OF VISIBLE PULSES..... 168

References..... 174

Figures..... 176

INTRODUCTION

The attempt to understand the elementary processes a molecule undergoes during a chemical reaction lies at the heart of physical chemistry. Reactions in the liquid phase are less well understood than gas-phase reactions, because of the greater conceptual problems of dealing with many-body dynamics, and because of the technical difficulty in working on very fast timescales. Here a very simple model reaction, iodine photodissociation and recombination, has been investigated and a fairly detailed understanding of the reaction pathway developed. The results also provide one of the few experimental tests for theories of liquid-phase reaction dynamics. These experiments were possible largely due to the development of a source of high quality picosecond light pulses. Work was also done on techniques to extend this source to the vibrational infrared and far-infrared portions of the spectrum. It is hoped that these techniques will aid not only in studying liquid-phase dynamics, but also in many other areas of both chemistry and physics.

In the study of liquid-phase reaction dynamics, progress is tightly linked to technical developments, specifically the generation of high-quality, picosecond laser pulses. Ideally the pulses should not only be shorter than the phenomena of interest, but also be narrow and tunable in frequency, high in energy, stable pulse-to-pulse, and reliable. Currently the system best meeting these criteria is an amplified synchronously-pumped dye laser. Although the basic scheme of amplification has already been published, these systems are new enough that the details of design and operation needed for optimal performance are not firmly established. For this reason, the system used for these

experiments is described and characterized in some detail in Chapter 1.

The experiments on iodine photodissociation are described in Chapter 2. These consist of time-resolved absorption measurements from 1000-295 nm following photodissociation in a number of different solvents. The experiments provide information on solvent-induced predissociation, geminate recombination, vibrational relaxation, and electronic relaxation. This system is the only liquid-phase reaction for which the relationship of these processes has been determined. Furthermore, experimental data on any of the processes individually is scant. Thus, these experiments provide a rare opportunity to test theories of liquid-phase dynamics. The comparison of the data to these theories is contained in Section E of Chapter 2.

Although observations at visible wavelengths have provided a large amount of information on iodine photodissociation, a great deal more information on this and many other problems is potentially available in other regions of the spectrum. However, the sources of picosecond and even nanosecond light pulses are much scarcer outside the visible region. For this reason, two methods of converting visible pulses to other spectral regions were developed. Chapter 3 discusses stimulated electronic Raman scattering in cesium vapor, which was used to shift picosecond, narrow-bandwidth nanosecond, and broad-bandwidth nanosecond pulses into the vibrational infrared. The nanosecond shifting was distinguished by an exceptionally wide tuning range (2040-1950 cm^{-1}) and by its use of pump pulses in the red, which is the frequency region most easily generated. Picosecond pulses were also shifted, but over a much narrower frequency range. Absorption by cesium dimers and two-photon ionization by atoms and dimers are suggested as the major factors

limiting performance.

Chapter 4 discusses the generation of far-infrared (FIR, 20-200 cm^{-1}) picosecond pulses by difference frequency mixing of a picosecond and a nanosecond light pulse. Simple theory predicts nearly 100% conversion to the FIR at the intensities used. In practice, typical conversions of 0.1-0.3% were observed. The conversion efficiency shows surprisingly little variation with the frequency generated. The FIR also had large pulse-to-pulse energy fluctuations, which are contrary to simple theory. Despite these limitations, the lack of fast pulsad sources in this spectral region makes these results quite interesting.

The material in Chapter 1 is not available in the liturature, whereas accounts of the experiments described in Chapters 2-4 have been published.[1-5]

References

1. M. Berg, A. L. Harris, and C. B. Harris, Phys. Rev. Lett. 54, 951 (1985).

2. A. L. Harris, M. Berg, and C. B. Harris, J. Chem. Phys., in press.

3. A. L. Harris, J. K. Brown, M. Berg, and C. B. Harris, Opt. Lett. 9, 47 (1984).

4. M. Berg, A. L. Harris, J. K. Brown, and C. B. Harris, Opt. Lett. 9, 50 (1984).

5. M. Berg, C. B. Harris, T. W. Kenny, and P. L. Richards, Appl. Phys. Lett. 47, 206 (1985).

CHAPTER I

DESIGN AND CHARACTERIZATION OF AN AMPLIFIED SYNCHRONOUSLY-PUMPED DYE LASER

A. Introduction

For most picosecond experiments, it is desirable to have a laser which not only produces short pulses, but which is also tunable, stable pulse-to-pulse, has a high repetition rate and is easy to operate. For many experiments, high peak power is also needed to produce non-linear optical effects and to produce a high concentration of transient species. A synchronously-pumped dye laser meets all these criteria except high power. Pulses of 1-2 ps can be routinely generated at 80 MHz and are easily tuned through the yellow to near-infrared portions of the spectrum. However, the energy is typically only 1.0-0.1 nJ/pulse, and so it is desirable to amplify the pulses. The amplification of 10^6-10^7 required for many applications is very high compared to that of typical laser amplifiers. The design of an amplifier with very high gain which also preserves the desirable properties of the dye laser presents unique difficulties.

The feasibility of such an amplifier was first demonstrated by Migus, et al.[1] and duplicated with minor variations by others.[2] The design described here is based on a slightly different system developed by Koch, et al.[3,4] Since these systems have only been in use for a short time, the details of design needed for optimal performance and a

thorough characterization of their operation is not available in the literature. This chapter includes such information for the laser system used in the experiments described in the remainder of this thesis.

The system is centered around a syncronously-pumped dye laser (Fig. 1). The dye laser is pumped by ~100 ps pulses from a mode-locked Ar^+ laser. When the cavity length of the dye laser is precisely matched to that of the Ar^+ laser, 1-2 ps pulses are produced at 82 MHz. The theory and operation of synchronously-pumped dye lasers has been well documented[5-13] and the entire system is commercially available. The only unusual feature of this application is that high power from the dye laser is not needed. This allows the laser to be run near threshold, so that short pulses are easily obtained.

An amplified, Q-switched Nd:YAG laser provides the power for the amplifier. The YAG laser produces 250 mJ of 532 nm light in a 10-ns pulse. A Molectron MY-34 laser is used, because of its nearly gaussian beam profile, which is transfered to the amplified pulse. The 10-Hz repetition rate of this laser determines the repetition rate of the entire amplifier.

The amplifier itself consists of three similiar stages (Fig. 1). As in Koch, et al.'s design, each stage is longitudinally pumped, that is the pump beam is parallel or nearly parallel to the amplified beam.[3,4] Other design have used transverse pumping, in which the pump beam is perpendicular to the amplified beam.[1,2] In the present system, dichroic mirrors are used to collinearly combine and later seperate the YAG and the picosecond pulses. The third cell is different from the first two in that the YAG and dye pulses travel in opposite directions.

Between each pair of amplification cells, the picosecond pulse is

focused into a jet containing a dye which strongly absorbs at the wavelength being amplified. These jets prevent fluorescence from one amplification cell from being amplified in the next cell. The picosecond pulse has sufficient intensity to saturate the dye's absorption, allowing most of the picosecond pulse to be transmitted. By absorbing the leading edge of the picosecond pulse, these saturable absorbers also shorten the pulse and thereby counteract lengthening effects in the amplification cells.

This chapter begins with a general desciption of the theory of dye amplifiers needed to understand the design of the amplifier (Section B). A more complete and quantitative discussion of the theory of the amplifier's operation can be found in the thesis of A. L. Harris.[14] Section C is a detailed desciption of the amplifier construction and design. The characterization of the final amplified pulse is contained in Section D.

B. Amplifier Theory

Because of the large difference in the widths of the YAG pulse (10 ns) and the picosecond pulse (1 ps), the pumping of the amplification dye and the extraction of the stored energy by the picosecond pulse can be treated seperately. In the pumping process, the YAG pulse excites the dye molecules over a 10-ns period. The YAG pulse is intense enough to strongly saturate the dye absorption, therby stabilizing the amplifier against fluctuations in the YAG energy. The fluorescence lifetime of the dyes normally used are ~5 ns, so the dye

could in principle store a major fraction of the energy in the YAG pulse.

In practice the amount of stored energy, and therefore the gain, is limited by amplified spontaneous emmision (ASE).[15] As the gain of an amplifier is increased, eventually the spontaneous emmision (fluorescence) from dye molecules at one end of the amplifier is amplified enough to seriously deplete the excited dye population. The amount of energy which can be stored is maximized by optimizing the cell length, the cell diameter, and the dye concentration.[14] Still, for practical parameters, an amplification of 10^6-10^7 cannot be obtained in a single cell. Multiple cells are necessary, and the ASE must be stopped from travelling between cells.

Several schemes have been used to block ASE between the amplifier cells, while allowing the picosecond pulse to pass. A recent commercial amplifier uses spatial filtering, which passes the picosecond pulse, while reducing the more highly divergent fluorecence. The major problem with this technique is that it does not shorten the picosecond pulse to compensate the broadening which occurs in the amplifier. Absorbing glass filters have also been used to block ASE.[1] The picosecond pulse bleaches the absorption and passes through. The absorption of the leading edge of the pulse helps to shorten it. Unfortunately the absortion of the glass only recovers slowly, so ASE is transmitted for a significant time after the picosecond pulse passes. Furthermore, the glass is susceptible to permanent damage from the high intensities used. The present system uses a jet of a dye solution as a saturable absorber.[1-4] The pulse shortening effect is still obtained, but dyes with relaxation times of 30 ps are available. Furthermore, a liquid

cannot suffer permanent optical damage. The major drawback of the saturable absorber jet is that complete transmission cannot be obtained in practice. The dye can be readily bleached from 10^{-4} to 20% transmission, but for unknown reasons, higher transmission is not obtainable. This fact has a profound effect on the design of the amplifier as will be discussed further on.

The other major consideration in the amplifier design is the difference between the small signal and large signal regimes. In the small signal regime, the signal (here the picosecond pulse) is small enough that the fraction of dye molecules de-excited is low. This is similiar to the Beer's law limit in absorption. In this limit amplification is exponential with distance, and the gain can be very high (10^5-10^6) in a typical cell. The amplification is also linear with the signal intensity so there is no change in the pulse shape. Unfortunately, the fraction of the energy stored in the dye which is transfered to the picosecond pulse is small. Furthermore, the gain is expcnentially dependent on the excited dye population and therfore highly dependent on the YAG pulse energy. This introduces a significant source of pulse-to-pulse instability.

The other extreme is the large signal or saturated regime. Here a significant fraction of the dye population is de-excited by the picosecond pulse. The gain is reduced and becomes non-linear with the signal intensity. The pulse is reshaped, since the leading edge experiences a high gain typical of the small signal limit, while the peak experiences a lower gain. The pulse broadening due to this effect is reduced by the sharpening of the leading edge of the pulse in the saturable absorber. The trailing edge of the pulse is not as strongly

broadened because the excited state population is depleted by the main peak of the pulse.

The advantage of the saturated regime is that the dye's stored energy can be efficiently extracted. The sub-linear dependence of the output energy on the input energy also stabilizes the output energy. Each stage in the current amplifier is saturated to some degree. A balance must be found in which the amplifier is sufficiently saturated for efficiency and stability, but not saturated enough to broaden the pulse excessively.

The large saturable absorber losses and the properties of large and small signal amplification dictate the overall design of the amplifier. Because of the saturable absorber losses, most of the final energy of the pulse must be deposited in the final stage. Consequently nearly all of the pump energy must go into the last cell; in the present case 90% of the YAG pulse pumps the third cell. To acheive sufficently saturated operation for efficiently energy extraction from the last stage, a fairly large input pulse is needed. The first two cells function primarily as preamplifiers to generate this pulse.

The first stage is primarily in the small signal limit, giving it a very high gain. This gain is needed to reach an intensity which can saturate the first saturable absorber. This stage is not efficient, but efficiency is unimportant since so little of the pump energy is invested here. The second stage is more strongly saturated than the first, so its gain is lower. The second stage is sufficiently saturated that the losses in the first saturable absorber are unimportant. If the input pulse to the second stage were increased by a factor of five by eliminating the saturable absorber losses, the output energy would only

increase slightly. This stage produces a pulse with sufficient energy to efficiently extract energy from the last cell.

These considerations show why the amplifier cannot be scaled up by adding another saturable absorber jet and a fourth amplifier cell at the output. The high losses in the additional saturable absorber would mean that most of the pump energy devoted to the third cell would have been wasted. Designs which incorporate four amplifier cells essentially have an extra preamplifier on the input to assist in getting enough intensity to saturate the first saturable absorber.[2] Other, less effective methods are used to isolate the ASE from this extra cell.

The other major design choice was the use of longitudinal pumping for all three cells. Systems have been successfully built which transversly pump the first cell.[1,2] The large amount of energy deposited in the last cell requires the pumping of a large volume which is best done longitudinally. In the present design, the first two cells are longitudinally pumped for several reasons. First, longitudinal pumping produces a more uniform beam profile, particularly when the pump beam has a good profile. Secondly, transverse pumping requires the dye concentration to be set so as to match the pump absorption depth to the pump diameter. Longitudinal pumping allows the dye concentration to be set independently to optimize the stored energy. Also, longitudinal pumping can use longer cells and therefore larger beam diameters. The small beams used in transverse pumping, as well as the need to work at the very edge of the dye cell, makes cell damage a greater problem. These factors also make allignment more difficult with transverse pumping.

The basic theory of dye amplification combined with practical

considerations has determined the general design of an efficient, high-gain amplifier. In the following section, the specific design and operating parameters of the system constructed are described.

C. Detailed Design and Operating Parameters

A modelocked Spectra-Physics 171-07 Ar^+ laser was used to pump the dye laser. This model is capable of producing 7 W of CW power at 5145 Å, which is much more than was actually needed. The standard modelocking crystal and mount were used, but seperate electronic components were purchased to reduce cost and improve quality. A highly stable modelocking frequency near 40.8 MHz was generated by a PTS 160 frequency synthesizer.[5] An ENI 300L 40-dB RF power amplifier in conjunction with a 20-dB attenuator produced sufficient RF power for modelocking. Normally 800 mW of RF was applied to the prism. Although the exact power level is not critical, 800 mW gives better results than the 200-400 mW used in some commercial systems. A Bird Model 43 directional power meter was found to be very useful in finding the resonant frequency of the crystal. Normally the minimum reflected power, which occurs at resonance, was about 20 mW. The modelocking crystal was mounted in a temperature-controlled oven maintained several degrees above room temperature.

The unusual freature of the Ar^+ laser's operation is that it was run at a relatively low power of 350-400 mW, instead of the more typical 1 W. Under these conditions, it was found that the pulses were shortest with the high reflectivity output mirror normally used for CW

operation. At energies near 1 W, a lower reflectivity mirror is normally used. When operating at low powers and with the low reflectivity mirror, it appears that the intracavity pulse is not intense enough to deplete the gain . Gain depletion is frequently an important pulse shortening mechanism in modelocked lasers.

Pulsewidth and stability were also dependent on proper adjustment of the cavity length. The frequency was always set to the modelocking prism's resonance and the length adjusted to match it. When the cavity was too short, a satellite pulse trailing the main pulse by ~200 ps was easily detectable with a fast photodiode and sampling scope. When the cavity was too long, there was only a broadening of the pulse, which was not always detectable with the fast photodiode. However, if the cavity was shortened, the average power decreased slowly, indicating more effective modulation. The cavity was normally shortened until just before the point at which a satellite pulse formed and the power jumped up. A pulse width of 110-120 ps was typically found on the sampling scope/photodiode combination. Since this system has a response time of ~60 ps, the true pulse width is probably <100 ps.

Adjustment of the cavity length as described not only optimizes the pulse width, but also improves the stability of the laser. Typically the noise was <3% peak-to-peak. Some 360-Hz ripple from the power supply was noticable, particularly at very low powers.

The dye laser used was a standard Coherent folded cavity laser. Only Rhodamine 6G was used in this laser. The laser could be tuned from 572-605 nm, with a peak at 574 nm. This is blue shifted from the normal CW tuning curve. Most often the laser was operated at 590 nm, which has only 1/2-1/3 the maximum power. The output power was typically

15-20 mW; operation below 10 mW becomes very unstable. At these low powers, the dye laser cavity length could be adjusted to just eliminate satellite pulses, while maintaining a narrow, smooth autocorrelation without evidence of a coherence spike. The full width at half maximum of 2.0-2.5 ps implied a pulse width of about 1.5 ps. A two-plate birefringent filter gave the best spectrum as is discussed in the next section.

The Q-switched Nd:YAG laser which pumped the amplifier was a Molectron MY-34 and was operated in an entirely standard fashion. The pulse energy was 250 mJ at 532 nm. The oscillator gain was adjusted to give a symmetrical three-peaked temporal shape. The width of the main peak was 8-10 ns. The timing of the YAG pulse was synchronized to the picosecond pulse train to better than 1 ns by external electronics which are described in the thesis of A. L. Harris.[14] The synchronization can be destroyed if the Q-switch permits some lasing before it is opened. This problem seem to have been eliminated with the introduction of humidity insensive polarizers in the oscillator.

The amplifier itself consisted of three stages. The first two stages had a common dye circulation system, while the third cell had a seperate circulator. The circulation systems were constructed so that the dye solution only came into contact with highly inert materials: stainless steel, glass, teflon, polyethylene, and polypropylene. This prevents corrosion, reduces dye degredation, and prevents contamination from old dyes adsorbed into the materials. Each system consisted of a pump, a reservoir and a filter. Centrifugal pumps worked best as they provide a high flow rate. The total volume of each dye system was ~2 liters.

The three dye cells were all nearly identical. The middle of each cell was glass to allow visual overlap of the beams and to monitor the dye fluorescence. The 2"-diameter, anti-refection coated windows were held in stainless steel end caps. The dye solution flowed in across the face of each window to help prevent deposits of degraded dye on the windows. The flow exited at the top center of the cell to aid in removing air bubbles. The windows were tilted at 20° from the normal to prevent reflection along the beam path. Each cell had a clear diameter of 1". The first two cells were 10 cm long and the third was 20 cm long. Originally all three cells were 10 cm, but the third cell was lengthened to try to increase the stored energy. The improvement was slight.

Ten percent of the YAG beam was split off from the main beam by an uncoated glass surface at 45° to the beam (Fig. 1). This beam was reduced and re-collimated by a telescope to a 2-mm diameter and split by a dielectric beamsplitter. Forty percent (10 mJ) pumped the first cell; sixty percent (27 mJ) pumped the second cell. The remaining 90% (225 mJ) was used at its full 6-mm diameter to pump the third cell. The YAG polarization was vertical to the table and parallel to the dye laser polarization. The gain is dramatically reduced for perpendicular polarization.

The third cell was pumped opposite to the direction of the dye beam for two reasons. Most importantly residual 532 nm light was prevented from contaminating the output beam. Also, more energy was deposited at the output end of the cell, where it can be effectively extracted. The small timing change introduced by this arrangement does not seem to be important.

The dye concentration for each of the cells was set to absorb 90-95% of the YAG beam. In the third cell this can simply be set by adding dye until the power does not increase. Greater care must be used in adjusting the dye concentration in the first two cells. If the concentration is too high, the ASE gain becomes too large. Even though little ASE is seen without the picosecond pulse, when the picosecond pulse is present, a significant amount of ASE developes before the saturable absorbers relax. This problem can be detected by monitoring the spectrum of the amplifier output. As the dye concentration of the first two cells is raised too high, a broad spectral component due to the ASE is formed. This problem can also lead to very high (>2 mJ), but spurious, measurements of the output energy.

The tuning ranges for the amplification dyes are relatively narrow (Fig. 2). The ranges are also peaked at fairly short wavelengths, as is typical of high intensity pumping. The choice of water or methanol as a solvent introduces significant shifts in the tuning range, which are helpful in covering the entire wavelength range. Methanol generally produces higher energies, but water produces a better beam profile. The turbulence of the dye solution flowing through the third cell causes a speckled beam profile, and this effect is stronger with methanol. A better beam profile results in better focussing, which compensates for lower energy in some applications (Chapt. III). The turbulence is difficult to remove, because a good dye flow was needed to prevent even more severe distortions of the beam from thermal inhomogeneities in the dye solution.

A final problem related to the amplification dye is photochemical decomposition from the YAG beam. This problem is compounded by the

relatively small amount of dye which is in the system, due to the low concentrations used. Even with stable dyes, the dye must be changed every day or two. The decomposition rates observed are much higher than liturature values[16] and may result from solvent impurities. Unfortunately, the volume of solvent needed prohibits the use of higher quality solvents. Kiton Red 620 is the most stable dye, while Rhodamine 640 is 9 times less stable. Rhodamine 6G is intermediate in stability. In aqueous solution, the addition of soaps is frequently recommended to prevent aggregation.[17] However at the low concentrations used here, soap has no affect on the dye efficiency, but it stongly reduces the dye lifetime. The addition of a triplet quencher (COT) and the removal of oxygen do not have any effect on the dye lifetime.

In contrast, the saturable absorber dyes are stable over years of use. Both Malachite Green and the very similar Crystal Violet have been used with marginally better results with Crystal Violet. Since Crystal Violet also absorbes more stongly in the spectral region of interest, it was used most of the time. Both dyes have a relaxation time of ~30 ps in ethylene gylcol.[18] Less viscous solvents give a faster relaxation time,[19] but at the expense of less stable jets. The dyes were made into highly concentrated solutions in ethylene glycol and used in a standard, Brewster angled jet designed of the type used in dye lasers. At low signal levels, an absorption of $\sim 10^{-4}$ was measured. At high intensities, the transmision saturated at only 15-25%. Calculations suggest that the transition should be easily saturated to near 100% transmission at the intensities used.

In the second saturable absorber, the intensity at the focus of the telescope is high enough to cause dielectric breakdown in the jet. The

breakdown occurs in pure ethylene glycol, with insignificant changes with the addition of the dye. Breakdown is characterized by sparking in the jet, a sharp decrease in transmission, and degredation of the beam quality. The jet was normally positioned in front of the focus, just before the point at which breakdown occurs.

The input to the first cell was a pulse of approximately 0.2 mJ in a 2-mm beam. It was amplified by a factor of 7500 to give a 1.5 μJ pulse. Only the center of the beam was well amplified, so the beam diameter was slightly reduced. The beam was re-expanded by the 20 mm: 50 mm telescope around the first saturable absorber jet. The ~80% loss in this jet brought the pulse energy down to 0.2 μJ as it entered the second cell. There it was amplified to ~50 μJ. The 25 mm: 80 mm telescope on the second saturable absorber jet expanded the beam to 6 mm in the third cell. Losses in the jet reduce the energy to ~10 μJ entering the third cell, where it was amplified to a final energy near 1 mJ (Fig. 2).

D. Characterization

The output of the amplifier is a 6-mm diameter beam consisting of a single picosecond pulse every 0.1 second. The beam is round and uniform in intensity, except for the solvent dependent speckle mentioned in the previous section. The spatial speckle is random from pulse-to-pulse and presumably causes some fuzziness when the beam is focused. This effect is difficult to observe, however, because the beam cannot be focused in air without causing dielectric breakdown. The breakdown causes a faint

spark at the focus and severly degrades the beam profile. Even unfocused the beam can cause serious damage, such as a permanent darkening of ordinary BK-7 optical glass. The damage mechanism may involve a two-photon absorption, since silica, which is transparent at the two-photon energy, is not darkened.

In normal operation there is very little energy in the beam aside from the picosecond pulse. Unamplified dye laser pulses are so strongly absorbed in the amplifier that they cannot be detected at the output. The nanosecond ASE from the third cell is intense, but it diverges so strongly that it is easy to seperate from the collimated picosecond pulse. ASE originating from the first or second cells can be well collimated, but such ASE is very dim or non-existant in normal operation. More insidious is ASE formed during the time the saturable absorbers are bleached, since it does not occur when the picosecond pulse is not present. As discussed in the previous section, this ASE can be detected spectrally and elliminated by reducing the dye concentration in the first two cells.

The pulse energy obtainable at various wavelengths is summarized in Figure 2. Tuning further to the blue is limited by the availability of dichroic mirrors capable of seperating the dye laser wavelength from the YAG wavelength. Further tuning to the red should be possible with appropriate dyes. The energies given were routinely obtained during experiments where careful attention was paid to the pulse energy. When less time was spent on pulse energy, routine energies fell below 1 mJ. The energy is sensitive the relative timing of the YAG pulse and the picosecond pulse. Adjustment of the timing to within 1 ns is sufficient to bring the amplified pulse energy to within 10% of it maximum. The

optimal timing for the picosecond pulse is 1-2 ns after the peak of the YAG pulse, depending on the dye, since the dye integrates the YAG energy for some time period.

The stability of the system is generally good. The pulse-to-pulse energy stability was normally ±10% rms. The synchronously-pumped dye laser normally operates for months with only minor adjustment. The amplifier itself must be alligned daily and sometimes during the day. It seem that the major source of mis-allignment is the YAG laser, which often needs small adjustments during the day.

Two important properties of a laser pulse are the pulse width and the spectral width. Ideally the spectral with should be the minimum width consistant with the pulse width; the pulse is then called "bandwidth limited". The pulse width is normally derived from an autocorrelation measurement.[20,21] Ideally the full width at half maximum (FWHM) of the autocorrelation can be related to the FWHM of the pulse by a numerical factor which depends on the pulse shape.[21] For example, for a gaussian pulse the autocorrelation should be a factor of $2^{1/2}$ broader than the pulse itself. For each pulse shape there is also a minimum product of the pulse FWHM and the spectral FWHM (the bandwidth product). Unfortunately, one pulse shape is sometimes assumed in calculating the pulse width and another in calculating the bandwidth product. It is more practical to calculate the bandwidth product as the product of the autocorrelation FWHM and the spectral FWHM. This product is 0.62 for a bandwidth limited gaussian and can be as small as 0.1 for other pulse shapes.

An additional complication is the occurance of a "coherence spike" on the autocorrelation when the pulse is not bandwidth limited. In this

case the width of the autocorrelation at 1/4 of maximum is approximately related to the pulse width, while the width at 3/4 of maximum is approximately related to the coherence time. It has been suggested that autocorrelation measurements often suffer from this problem, even when a coherence spike is not readily resolvable.[22,23]

The spectrum of the amplified pulse is strongly dependent on the bandwidth of the tuning element in the dye laser. Figure 3 shows spectra of the amplified pulse with a one-plate birefringent filter in the dye laser. The average spectrum is broad, but smooth. Examination of spectra of individual pulses shows severe modulation, which is random shot-to-shot. This feature is most likely originally present in the pulse from the dye laser and implies that the pulse is not bandwidth limited. In fact, the product of the autocorrelation FWHM and the average spectrum FWHM is 1.1, whereas it should be <0.62. However, the product of autocorrelation width at 1/4 maximum and the average width of the spectral modulation is 0.66, a reasonable value. Similiarly, the product of the autocorrelation width at 3/4 width with the average spectral width is 0.40, another reasonable value. Thus it appears that the pulse envelope is about 1.6 ps as measured by the 3/4-maximum width of the autocorrelation, and that this width corresponds to the width of the modulation of the spectrum. However, the pulse has severe noise with a time scale of 0.5 ps as measured by the 3/4-maximum width of the autocorrelation, and this noise determines the overall spectral width. When the cavity length of the dye laser is misadjusted, the spectrum can also show strong, periodic modulations which have been attributed to etalon effects.[6] These are also indications of poor pulse quality.

The situation is much different when a two-plate birefringent

filter, which has a narrower bandwidth, is used in the dye laser. With this filter, the single pulse spectrum is single peaked over 80% of the time (Fig. 4b). The product of the average width of single pulse spectra and the autocorrelation FWHM is 0.51, a number consistant with a bandwidth limited pulse. The average spectrum (Fig. 4a) is slightly broader than the average width of the single pulse spectra because there is some pulse-to-pulse shifting of the peak wavelength. Thus, the two-plate filter produces a much more bandwidth limited pulse than the one-plate filter.

Although the spectrum with the two-plate filter is generally well behaved, there is some broadening during the amplification (Fig. 5). If the YAG beam to the third cell is blocked, the spectrum in Figure 5b is obtained. The spectrum is somewhat broader than the input spectrum, but pulse shortening discussed below. With the amplifier in full operation however, a shoulder developes on the long-wavelength side of the spectrum (Fig. 5c). Single-pulse spectra show that this shoulder often forms a distinct second peak (Fig. 4b). These effects are characteristic of self-phase modulation, which presumably occurs as the high intensity amplified pulse travels through the third cell.[24] The presence of modulation only on the long-wavelength side of the spectrum indicates that it is caused by a slowly relaxing mechaism, most likely the rotational reoriention of the dye solvent.

Two unusual spectral features are not charteristic of normal operation, but may be seen when operating under unusual circumstances. First, when the dye laser is operated with the two-plate filter on the blue edge of the tuning curve, a spectrum with strong, periodic modulation can be produced (Fig. 6). Even more peculiarly, the

autocorrelation also developes strong, periodic modulations. The second spectral feature occurs when the dye laser cavity length is severly misadjusted. A second distinct spectral peak developes and becomes stronger as the mismatch increases. Finally when modelocking ceases, only the second peak remains.

The amplified pulse autocorrelation with the two-plate filter is shown in Figure 7. It has a FWHM of 1.49 ps indicating a pulse width of 1 ps, if a gaussian pulse shape is assumed. The autocorrelation is actually narrower than the autocorrelation of the input pulse, especially in the wings. The input pulse autocorrelation measures 1.25, 2.3, and 4.46 ps at the 3/4, 1/2, and 1/4 maximum respectively, while the corresponding measurments for the amplified pulse are 1.0, 1.5, and 2.65 ps. Narrow wings in the autocorrelation suggest that the pulse is bandwidth limited and that the FWHM of the autocorrelation is meaningful. The narrowing with respect to the input pulse suggests either that the pulse shape changes dramaticly during amplification and/or that the amplified pulse is shorter and more bandwith limited than the input pulse. The pulse shortening and re-shaping are presumably caused by clipping of the leading edge by the saturable absorbers and clipping of the falling edge from gain depletion, in conjunction with the pulse broadening effects of gain saturation. An overall shortening of the pulse is consistant with the spectral broadening discussed above. As the input pulse is broadened by misadjusting the cavity length of the dye laser, the amplified pulse autocorrelation broadens in rough proportion.

References

1. A. Migus, C. V. Shank, E. P. Ippen, and R. L. Fork, IEEE J. Quantum Electron. QE-18, 101 (1982).
2. S. R. Rotman, C. Roxlo, D. Bebelaar, T. K. Yee, and M. M. Salour, Appl. Phys. B 28, 319 (1982).
3. T. L. Koch, L. C. Chiu, and A. Yariv, Opt. Commun. 40, 364 (1982).
4. T. L. Koch, L. C. Chiu, and A. Yariv, J. Appl. Phys. 53, 6047 (1982).
5. N. J. Frigo, T. Daly, and H. Mahr, IEEE J. Quantum Electron. QE-13, 101 (1977).
6. R. K. Jain and C. P. Ausschnitt, Opt. Lett. 2, 117 (1978).
7. C. P. Ausschnitt and R. K. Jain, Appl. Phys. Lett. 32, 727 (1978).
8. J. P. Ryan, L. S. Goldberg, and D. J. Bradley, Opt. Commun. 27, 127 (1978).
9. A. I. Ferguson, J. N. Eckstein, and T. W. Hänsch, J. Appl. Phys. 49, 5389 (1978).
10. D. M. Kim, J. Kuhl, R. Lambrich, and D. von der Linde, Opt. Commun. 27, 123 (1978).
11. C. P. Ausschnitt, R. K. Jain, and J. P. Heritage, IEEE J. Quantum Electron. QE-15, 912 (1979).
12. D. B. McDonald, D. Waldeck, and G. R. Fleming, Opt. Commun. 34, 127 (1980).
13. J. Herrmann and U. Motschmann, Appl. Phys. B 27, 27 (1982).
14. A. L. Harris, Ph.D. thesis (University of California, Berkeley, California, 1985).
15. U. Ganiel, A. Hardy, G. Neumann, and D. Treves, IEEE J. Quantum

Electron. QE-11, 881 (1975); A. Migus, J. L. Martin, R. Astier, and A. Orzag, in Picosecond Phenomena II, edited by R. M. Hochstrasser, W. Kaiser, and C. V. Shank (Springer-Verlag, New York, 1980), p. 59.

16. E. P. Ippen, C. V. Shank, A. Dienes, IEEE J. Quantum Electron. QE-7, 178 (1971).

17. J. Selwyn and J. I. Steinfeld, J. Phys. Chem. 76, 762 (1972).

18. D. Waldeck, private communication.

19. V. Sundström, T. Gillbro, and H. Bergström, Chem. Phys. 73, 439 (1982).

20. D. J. Bradley and G. H. C. New, Proc. IEEE 62, 313 (1974).

21. E. P. Ippen and C. V. Shank in Ultrashort Light Pulses, edited by S. L. Shapiro (Springer, NY, 1977), p. 88.

22. D. B. McDonald, J. L. Rossel, G. R. Fleming, IEEE J. Quantum Electron. QE-17, 1134 (1981).

23. D. P. Millar and A. H. Zewail, Chem. Phys. 72, 381 (1982).

24. F. Shimizu, Phys. Rev. Lett. 19, 1097 (1967).

Figure Captions

Fig. 1. Schematic diagram of the amplified, syncronously-pumped dye laser.

Fig. 2. Amplified pulse energy at various wavelengths for different dye/solvent combinations. ● - methanol solutions, ▲- water solutions. a) R 590, b) R 610, c) KR 620, d) R 640.

Fig. 3. Spectra of the amplified picosecond pulse using a one-plate birefringent filter in the dye laser. Calibration lines are marked by an X. The spectra are centered at 599 nm. a. average of ~100 pulses. b. single pulse.

Fig. 4. Spectra of the amplified picosecond pulse using a two-plate birefringent filter in the dye laser. The full widths at half maximum are marked. Calibration lines are marked by an X. The spectra are centered at 582 nm. a. average of ~100 pulses. b. single pulse.

Fig. 5. Spectral broadening through the amplifier. Calibration lines are marked by an X. The spectra are centered at 582 nm. The full widths at half maximum are marked. a. average spectrum after the dye laser. b. average spectrum without pumping the third stage. c. average spectrum after complete amplification.

Fig. 6. Spectrum of the synchronously-pumped dye laser at a wavelength which displays unusual modulation. A multi-peaked autocorrelation was

observed at the same time. The peak spacing is 10.7 cm^{-1}. A two-plate birefringent filter was used in the dye laser. The spectra is centered at 572 nm. Calibration lines are marked by an X.

Fig. 7. Autocorrelation trace of the amplified pulse. The FWHM of 1.49 ps implies a pulse width of 1 ps assuming a Gaussian pulse shape.

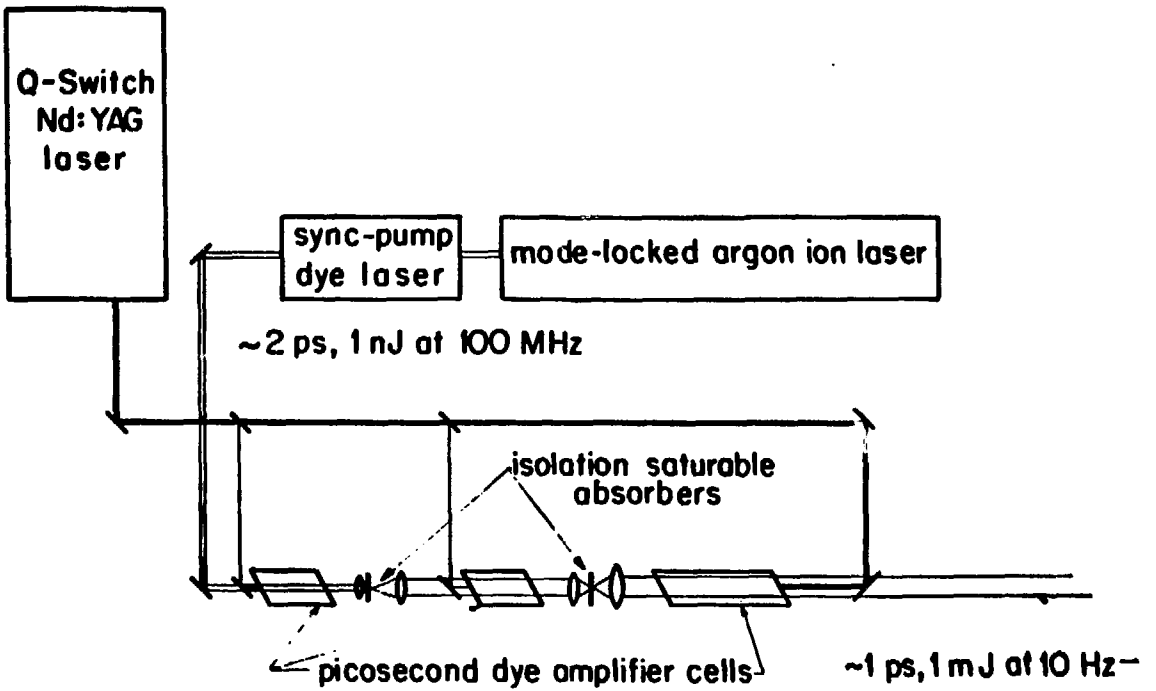
Q-Switch
Nd:YAG
laser
sync-pump
dye laser
mode-locked argon ion laser
~2 ps, 1 nJ at 100 MHz
isolation saturable
absorbers
picosecond dye amplifier cells
~1 ps, 1 mJ at 10 Hz

Fig. 1

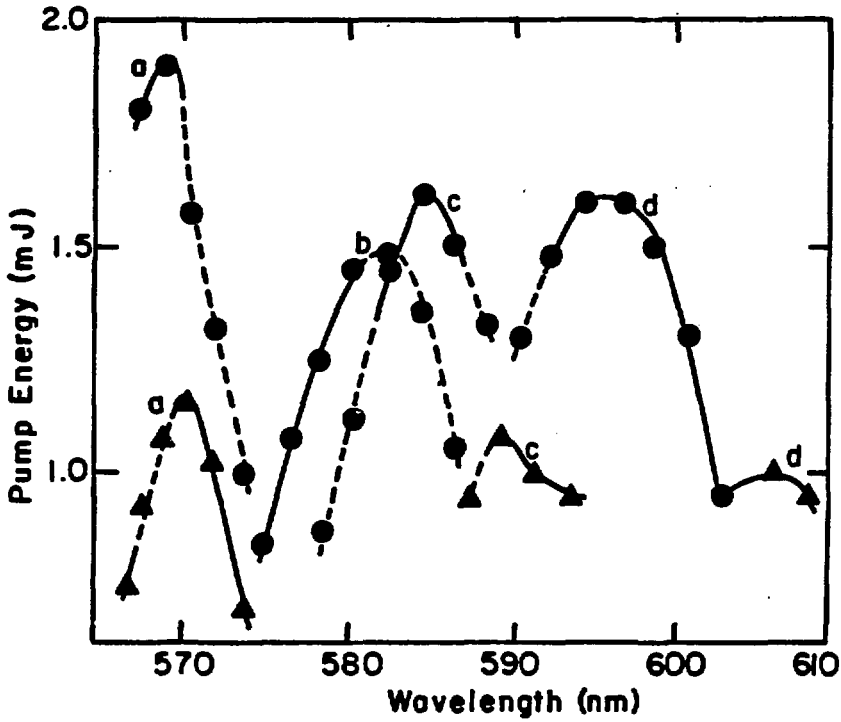
2.0
1.5
1.0
Pump Energy (mJ)
570
580
590
600
610
Wavelength (nm)
a
b
c
d
a
c
d

Fig. 2

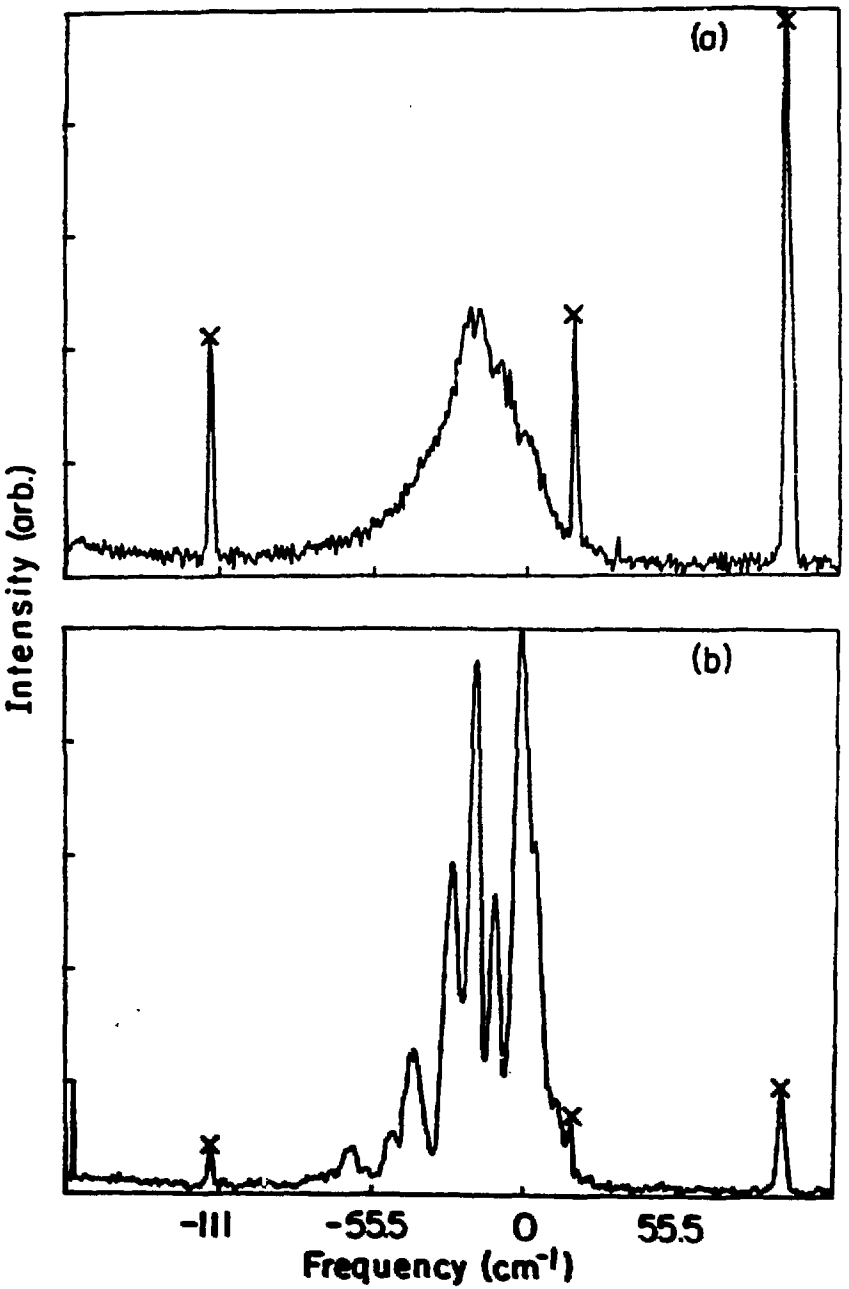

Fig. 3

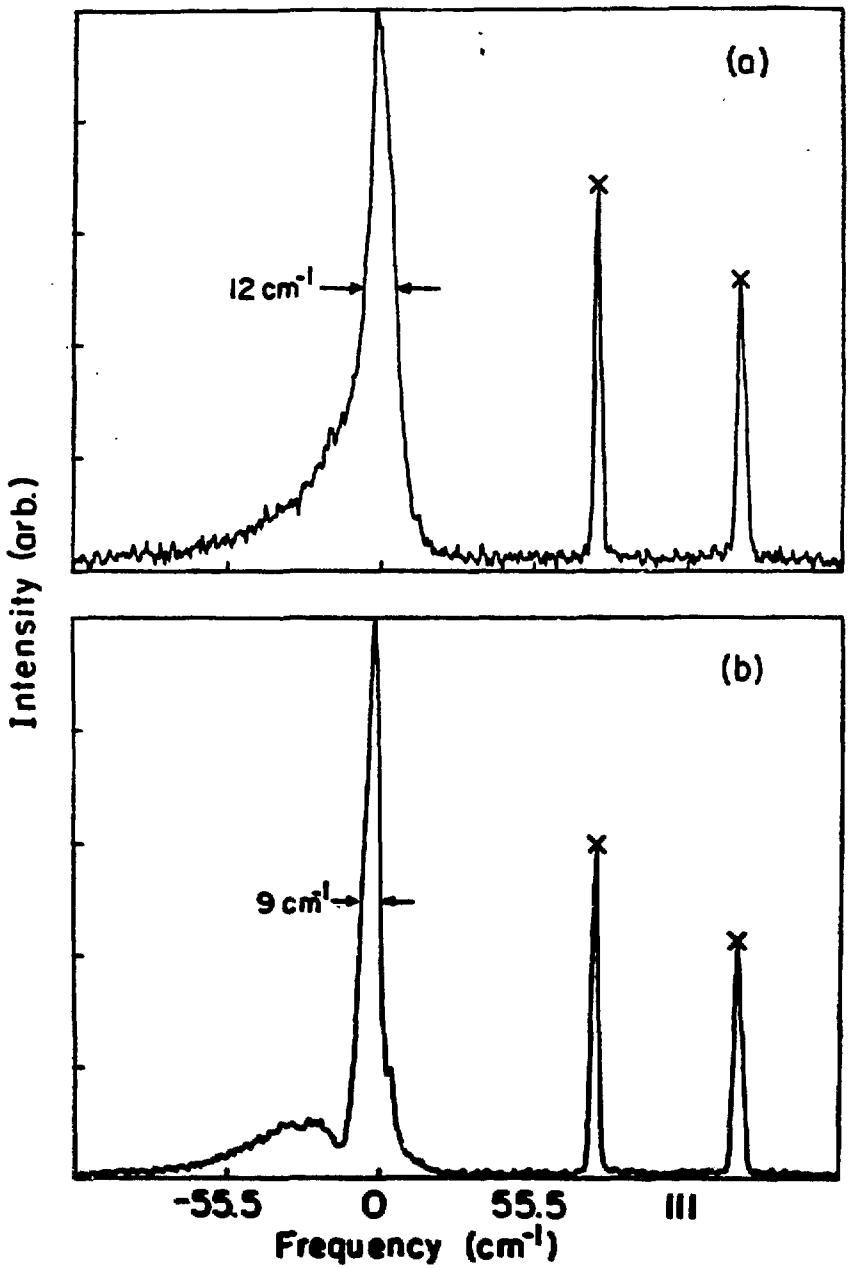

Fig. 4

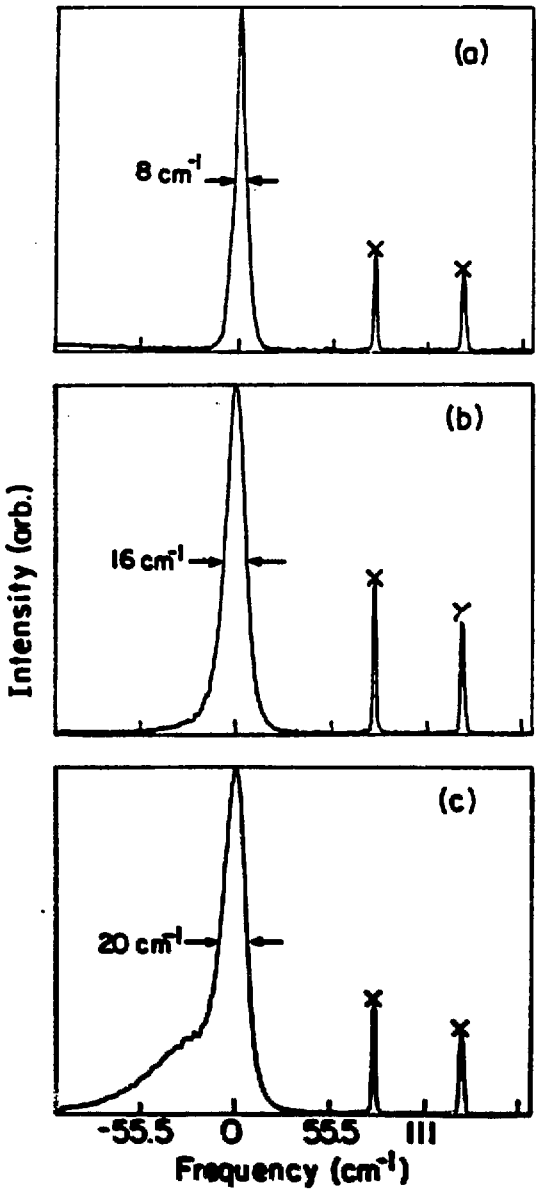
(a)
8 cm⁻¹
(b)
16 cm⁻¹
(c)
20 cm⁻¹
Intensity (arb.)
-55.5
0
55.5
111
Frequency (cm⁻¹)

Fig. 5

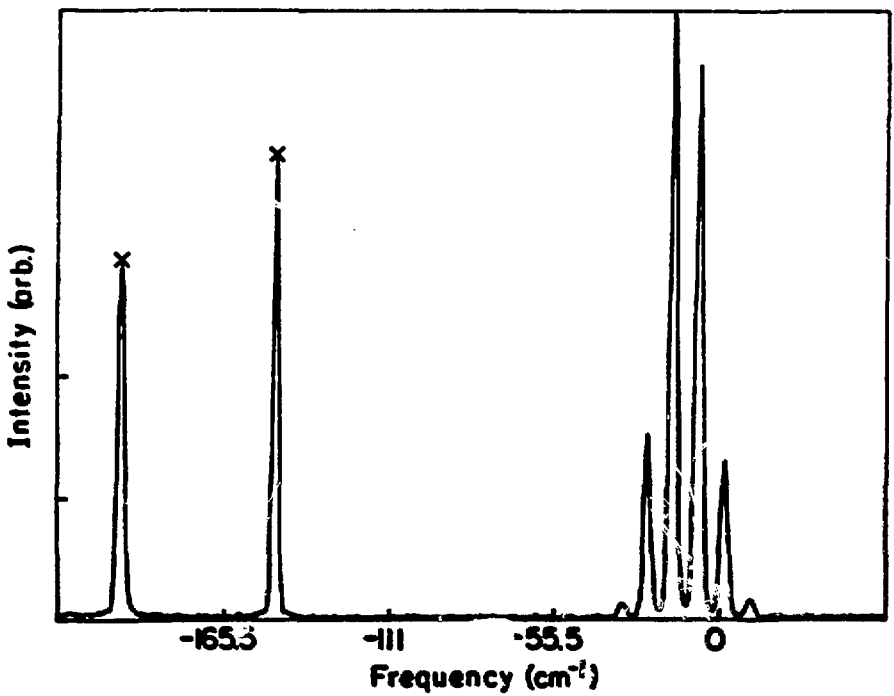

Fig. 6

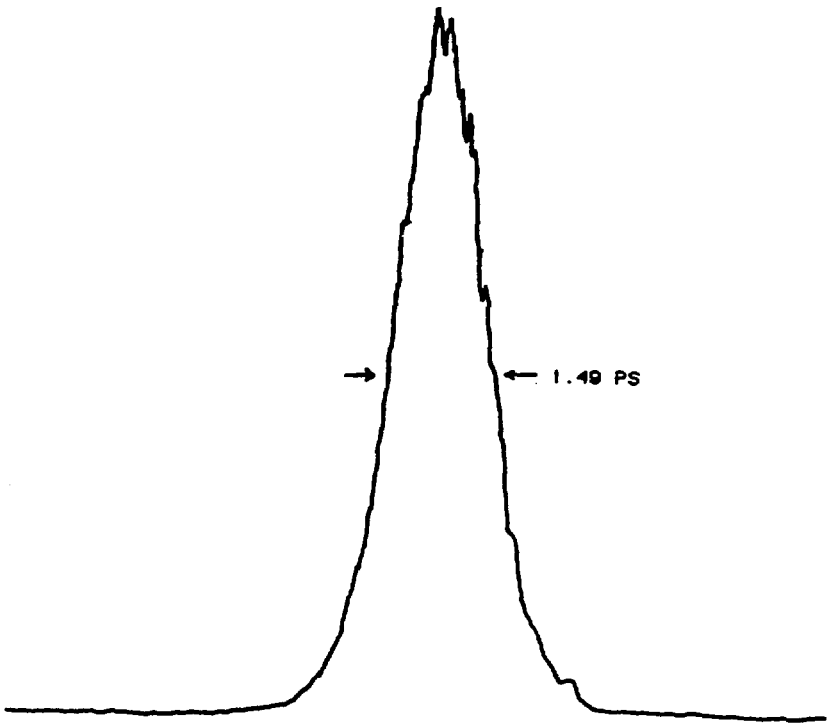

Fig. 7

CHAPTER II.

IODINE PHOTODISSOCIATION AND RECOMBINATION IN SOLUTION: PICOSECOND DYNAMICS AND COMPARISON TO LIQUID-PHASE REACTION THEORY

A. Introduction

Elementary reactions in the liquid-phase are not only much faster than gas-phase reactions, but also involve qualitatively new effects. The best known of these is the "cage effect" or more precisely geminate recombination.[1] Fragments from a molecular dissociation, which would seperate in the gas phase, hit the surrounding solvent and rebound toward each other. There is a high probability that the fragments in the liquid will recombine instead of seperating. In addition, vibrational relaxation, which must occur to complete a reaction, may be affected by the correlated forces occuring in a liquid. These effects are poorly understood, particularly for the excited vibrational levels, which participate in chemical reactions. Finally, the rapid perturbations in the liquid can cause rapid, non-radiative electronic state changes, which can affect the reaction dynamics.

The iodine photodissociation/recombination reaction has served as a primary model system for the study of such effects in liquid-phase chemical reactions. Because it is a diatomic, the dynamics are simpler to treat theoretically. Also, the spectroscopy is well understood. Fortunately, dissociative transitions are easily reached with available lasers. However, despite this apparent simplicity and a long history of

study,[2] disagreement about the timescales and importance of the most basic steps in this reaction has arisen. Conflicts in both interpretation[3,4] and in experimental results[5-11] have occured. A series of picosecond absorption experiments were undertaken to help clarify the situation. It was found that geminate recombination occurs at least an order of magnitude faster than proposed by some.[3,5] Furthermore, the relative roles of solvent-induced vibrational relaxation, predissociation, and electronic relaxation are also determined. The experiments were performed in a series of alkane and chlorinated methane solvents to explore the range of possible behaviors and to provide a means of testing predicted trends in solvent effects. In particular, the prediction of an important role for resonant vibration-to-vibration energy transfer was tested and was found to be unable to explain many of the results. Several theoretical approaches to understanding the microscopic motions of reactive atoms and the energy relaxation of the recombined molecule were also evaluated through comparisons with the experimentally derived dynamics.

The first extensive studies of the iodine photodissociation reaction were carried out by Noyes and coworkers, who studied the quantum yield of unrecombined atoms with a scavenger technique and interpreted the results with simple diffusion models.[14-19] More recently, laser techniques have been used to study both the yield of unrecombined atoms and the rate of non-geminate recombination over a wide range of densities.[20-23] These studies do not, however, provide direct information about the dynamics of geminate recombination.

The first time-resolved measurements of geminate iodine recombination were made by Chuang, Hoffman and Eisenthal.[2] The iodine

was primarily excited to the bound B state (Fig. 1) by a pulse of 532 nm light, and the subsequent reaction was monitored by measuring the absorption at the same wavelength. The B state was found to undergo rapid (<20 ps) solvent-induced predissociation. The predissociation may occur to any of several dissociative states, but it has recently been argued that the $a(1_g)$ state is probably responsible for most collision-induced predissociation (Fig. 1).[24] Following predissociation, the molecular absorption was found to partially return in 140 ps in CCl_4 and 70 ps in hexadecane.[25] These absorption recoveries were interpreted as a direct measurement of the recombination of iodine atoms with their original partner. Similar measurements in a series of n-alkane solutions[26,27] and in liquid xenon[28] have been interpreted in the same way.

Nesbitt and Hynes subsequently suggested that the recovery of the green absorption might be due to slow vibrational relaxation rather than geminate recombination.[3] They pointed out that the Franck-Condon factors for absorption at 532 nm from the iodine molecule's X state are strong only for the lowest vibrational levels. If vibrational relaxation of the recombined iodine molecule were slow, the absorption recovery at 532 nm would also be slow, even if the recombination process itself were fast. Calculations by Nesbitt and Hynes and others have shown that relaxation times of 100 ps to 1 ns are plausible.[3,29-31] Molecular dynamics simulations have explicitly predicted that absorption should first appear in the near infrared when the molecule is highly vibrationally excited and that it should shift smoothly to shorter wavelengths as the molecule vibrationally relaxes (Fig. 1).[9,10,31]

Two nearly simultaneous experimental efforts to confirm the

predicted red absorptions have obtained conflicting results. Bado et al. observed transient absorptions from 595-640 nm in alkane and haloalkane solvents which shifted to shorter wavelengths in an ~100 ps period.[7-10] They concluded that the absorptions were due to vibrationally relaxing molecules and that geminate recombination is faster than vibrational relaxation. Kelley et al. also observed transient absorptions from 590 to 750 nm in alkane and chloroalkane solvents, but found no spectral shift with time.[4,5] They assigned the red absorption to recombined molecules trapped in the A or A' states (Fig. 1). Based on the lack of a spectral shift, they concluded that vibrational relaxation is fast and that geminate recombination requires ~100 ps as originally proposed.

The present data taken in a number of inert solvents extend from 295 nm to 1000 nm with higher time resolution and signal-to-noise ratio than previously available. These data resolve two components in the red absorption, one of which will be assigned to vibrationally relaxing X-state molecules and one to molecules trapped in the A' state. Newly observed absorptions in the UV provide direct information on the vibrational relaxation and predissociation rate of the initially populated B state. Although the absorption decays in different classes of solvent initially appear quite different, it will be shown that they can all be explained in terms of a single model.

This model for the origin of various absorption components clarifies the physics of the various reaction steps and for the first time provides a firm experimental basis for a theoretical understanding of the reaction dynamics. First, the reaction model implies that geminate recombination is predominantly completed in <15 ps in all of

these solvents, and that slow vibrational and electronic energy relaxation account for the subsequent slow (100 ps - 3 ns) transient recovery. Molecular dynamics simulations are shown to be consistent with the existence of a rapid recombination process, while hydrodynamic models have little predictive value. Secondly, the evolution of the vibrationally relaxing X-state population is extracted from the absorption data with the use of calculated spectra from vibrationally excited molecules. The suggested role of vibration-to-vibration energy transfer to the solvent is not supported by the data in chlorinated methane solvents, although this mechanism may play a role in the alkane solvents. Finally, solvent variations in the iodine molecule's electronic-state lifetimes are not accounted for by present theories.

The later sections summarize the reaction model and make quantitative comparisons with theories designed to account for the dynamics of the individual reactions steps. Those sections are intended to be self-contained so that readers less interested in experimental and spectroscopic details may read further beginning at section III E. The organization of the paper is as follows: section II discusses the experimental methods, and section III assigns the components of the absorption data. Section IV compares the present results with the sometimes contradictory earlier work. Finally, section V examines the ability of available reaction models to account for the dynamics of the reaction steps as observed in this work.

B. Experimental

The iodine reaction was initiated with light at 590 nm, a wavelength which gives 87% excitation to the predissociative B state and 7% and 6%, respectively to the directly dissociative $^1\Pi_u$ and A states (Fig. 1).[32] At 590 nm, molecules are primarily excited from the v=1,2 levels of the X state to the v=12-14 levels of the B state (Fig. 1).[33] Light pulses at 590 nm were generated by the amplified synchronously-pumped dye laser described in Chapter I. The amplified pulse of 0.8 mJ was approximately one picosecond long and had shot-to-shot energy fluctuations of ±10% rms.

The transient absorption apparatus used from 350-1000 nm is diagrammed in Fig. 2. The amplified pulse was first split by a beamsplitter; 50% formed the excitation pulse and 50% was used to generate a probe continuum. The excitation pulse passed through a computer controlled delay line and through filters which blocked interfering emission at long wavelengths from the last amplification cell. The excitation polarization was controlled with a half-wave plate.

A white light continuum, extending from 310 to >1000 nm, was generated by focussing the probe beam with a 6-cm focal length lens into a 5-cm cell of water. The continuum was recollimated and a bandpass filter ($\Delta\lambda$ ~10 nm) selected a single probe wavelength. This light was spatially filtered to improve its spatial quality and focussing properties. Two uncoated silica flats each reflected 10% of this beam to form the reference and sample probe beams. The second flat also served to collinearly recombine the excitation and probe beams. A 20-cm

focal length lens focussed both beams into the sample which was placed 16 cm behind the lens. The two beams formed nearly identical 800 μm spots (50% transmission diameter) in the sample.

For absorption measurements at 295 nm a different arrangement was used (not shown). The entire laser pulse was reduced by a telescope to a collimated 2-mm beam and passed through a 1-mm KDP doubling crystal. The beam was then re-expanded and the ~10% which had been converted to 295 nm was separated by a dichroic filter. The visible beam passed through a variable delay line. After a small portion of the UV was split off as a reference beam, the UV probe and visible excitation pulse were collinearly recombined on a second dichroic and focussed through the sample with the same geometry described above.

With either arrangement, the excitation pulse was blocked after the sample with a combination of dielectric interference and absorbing glass filters. Both the reference and the sample probe beams were measured by identical 1-cm diameter photodiodes (EG&G DT-110). The current pulses from the photodiodes were digitized in 10-bit current-integrating gated A/D converters, which were interfaced to a minicomputer. The reference and sample signals were ratioed to correct for shot-to-shot variations in the probe intensity and then averaged. A 1-ps time resolution in this experiment is indicated by both autocorrelation measurements of the initial laser pulse (see Chapter I) and by the fastest risetimes observed in the experiment.

The absorption changes were often small because the excitation density could not be further increased without generating a small amount of continuum in the sample, which interfered with measurements at the probe wavelengths. Thus, special care was needed in these experiments

to reduce noise. Experiments were performed with one probe wavelength at a time, because the dynamic range of multichannel detectors restricts the signal-to-noise attainable. Because of spectral fluctuations of the probe continuum within the pass band of the wavelength selecting filter, any optical element with a slope in its absorption had to be duplicated in both the sample and reference beams. In particular, identical samples and filters were placed in both beams. With proper precautions, the ratio of sample to reference intensities could be measured in a single shot with a fractional error (s.d./mean) of as low as 2×10^{-3}. Typical decay curves containing 200-300 delay points were scanned 4-5 times averaging 10-25 laser shots at each delay. The scans were then averaged to give a total of 50-100 laser shots per delay point, which reduced the noise to a few parts in 10^4. Thus even with transmission changes of only 1%, signal-to-noise ratios of 30-100 could be achieved in 1-2 hrs of data collection.

Data was taken for iodine solutions in CCl_4, $CHCl_3$, CH_2Cl_2, hexane, nonane, hexadecane, and cyclohexane. Alkane and chloroalkane solvents were chosen because of their low propensity for complex formation with iodine molecules or atoms, and the absence of contact charge-transfer absorption from molecules in the spectral region examined.[35-40] All solvents were Burdick and Jackson chromatography grade. Less pure spectral grade solvents showed additional ultraviolet absorption features attributed to iodine-impurity interactions.[35,41] The iodine crystals (Mallinckrodt analytical reagent grade, >99.8% I_2) were used as received. Iodine concentrations were set to give an absorbance of 0.40 ± 0.01 at 590 nm in the 5 mm sample cell (~5 mM). Reducing the concentration by a factor of five caused no change in the decay curves

in hexane and CCl_4 at either 635 nm or 295 nm. However, raising the concentration by a factor of five did cause some changes at 295 nm. These artifacts could have been caused by excited state quenching[6] or by the presence of dimers.[42] At the concentrations used, the excitation density is low enough that the non-geminate recombination time can be calculated to be >1 μs,[43] which can be entirely neglected on the time scale of these experiments.

The excitation intensity was relatively reproducible from day to day; the maximum absorption change on identical curves run on different days was reproducible to about ±30%. Thus, absorbance changes at different wavelengths and in different solvents may be roughly compared. Exceptions are the data at 295 nm which are estimated to be uncertain by a factor of two relative to the continuum probe data because of the different experimental setup. Several curves were also taken with 3x and 5x lower excitation intensity to insure that no intensity dependent effects were present.

Transient absorption curves were taken at 1000 nm, 860 nm, 710 nm, 635 nm, 500 nm, 350 nm, and 295 nm in most solvents. In addition, absorption measurements were made at 370 nm, 400 nm, and 760 nm in CCl_4 and at 400 nm in hexane. Attempts were made to collect data at 430 nm, but the absorption changes were too small for meaningful results to be obtained. Both perpendicular and parallel polarization measurements were made for most wavelength/solvent combinations. No polarization effects were seen. At some wavelengths, a nonlinear interaction, which occurred when pump and probe pulses were temporally overlapped, caused an artifact near zero time when both polarizations were parallel. The artifact was greatly reduced by using perpendicular polarizations.

C. Results

In this section, the results are discussed beginning with the slowest transient absorption components and ending with the fastest. The slow, intermediate, and fast transient components in each solvent will be assigned to the recombined molecule's A'-state, X-state, and B-state dynamics, respectively. In order to allow quantitative investigation of the faster X-state and B-state dynamics, the slower A'-state component will be subtracted from the data. Finally, a reaction model is summarized, and an upper bound on the geminate recombination time is inferred.

The transient absorption curves in the chlorinated methanes, the straight alkanes, and cyclohexane initially appear distinct, based on their overall kinetic behavior. In the chlorinated alkanes (Figs. 3-5), the absorption decays extend beyond 900 ps and clearly have two components, while in the alkanes (Figs. 6-8) the absorption decays are complete within 200 ps and two components are not as clearly separated at the red wavelengths. Cyclohexane differs from the straight alkanes in that it has unusual double peaked absorption curves which are not seen in the other solvents (Fig. 8). As will be seen, however, all these differences can be explained in terms of a change in the relative time scales of the decay processes.

Slow Decays: A'-State Trapping

The first transient absorption feature to consider is a slowly decaying component which appears at red (635-1000 nm) and UV (400-295 nm) wavelengths. In the chlorinated methane solvents, this component is slow enough (>500 ps decay time) to be well-resolved from other, faster decaying components (see e. g. Fig. 3). The decay time of this component is the same in both the red and UV and is wavelength independent within each region. This indicates that the slowly decaying absorption component is due to a single state or to a closely coupled set of states. In the alkane solvents, a slow UV decay component is again well-resolved from an early time transient (see e.g. Fig 6), and it has a spectrum similar to the slow UV component in the chlorinated methane solvents. This absorption is assigned to the same state seen in the chlorinated methanes, even though its decay time is much faster (~65 ps decay time). A corresponding component with the same decay time found in the UV also appears in the alkane red absorptions, although this component is not as well separated from the early components as it is in the chlorinated methane solutions. The data thus indicate that following photodissociation in all of these solvents, a state is populated which absorbs at both red and UV wavelengths.

Kelley et al. have previously observed the long decay component in the red, although they could not resolve it from the other absorption components in the alkane solutions.[4,5] They assigned the absorption to iodine molecules trapped in either the A or A' state (Fig. 1). These are the only two excited states which correlate with two ground state atoms and which are bound by significantly more than kT (1640 cm^{-1}

A state, 2500 cm^{-1} A' state).[44-46] This assignment is supported by the identification of trapping to both the A and A' states following photodissociation of iodine in matrices.[47] Since the same state appears to be responsible for both the red and UV absorptions, the UV absorptions can also be assigned to the A or A' state.

To more clearly illustrate the points just discussed, representative data is shown in Figs. 3-8. Figure 3 shows the long A/A'-state decay component in CCl_4 solution at red wavelengths, as well as an early time (<200 μs) transient, which is discussed in the next section. The red absorption behavior is similar in other chlorinated methane solvents as Fig. 4 shows for 635 nm absorption. Figure 5b illustrates the slow UV absorption component in CCl_4 solution. As previously noted, this component has the same decay time as the long component in the red absorption. In the chlorinated methanes, the most accurate A/A'-state lifetimes were obtained at 635 and 710 nm (Table 1). It was assumed that the absorptions decay exponentially to zero as found by Kelley et al.[4] Within both the UV and red regions, the A/A'-state absorption is strongest at short wavelengths and weaker at long wavelengths. An experimental A/A'-state absorption spectrum in CCl_4 was determined by fitting exponential curves to the long time decays and extrapolating to zero time (see Fig. 11).[48]

The UV absorption of the A/A' state in hexane appears as the longer decay component at 295 nm and 350 nm in Fig. 6a. A small component at 400 nm is discussed in Sec. IIIB. Similar absorptions were observed in the other alkane solvents. The corresponding red absorption component in hexane is illustrated in Fig. 7. The red absorption data show two decay components, the longer of which matches the A/A'-state decay time

found in the UV (solid curves at 710 and 860 nm). Since the early red absorption recovers more slowly at shorter wavelengths (Figs. 3,7, and 8), the 65 ps A/A'-state decay is not resolved at 635 nm. Because of the difficulty of separating the red absorption components in the alkanes, the 350 nm absorptions give the best A/A'-state lifetimes in those solvents (Table 1). As in the chlorinated methane solvents, the A/A'-state absorption is weaker at longer wavelengths within both the red and UV regions. The overall similarity of the behavior at different wavelengths identifies the longer absorption component in both the alkanes and chlorinated methanes as arising from the same source despite the disparity in the lifetimes.

In addition to the transient UV absorption components, a long, non-decaying UV absorption occurs in alkane solvents (Fig. 6b and Table 2). This absorption offset probably results from solvent-contact charge-transfer transitions of free iodine atoms which have escaped recombination.[39] The charge-transfer absorption spectrum is known and is strongly solvent dependent. The UV free atom offset should not be substantial in chlorinated methane solvents except at 295 nm.[39] In fact, long time offsets must be assumed at 295 nm in the chlorinated methane solvents to match the A/A'-state lifetime found at other wavelengths (Table 2).

At wavelengths near the peak of the molecular ground state absorption (450-570 nm), there is a net absorption decrease (bleach) following photodissociation, due to the loss of ground state molecules. In chlorinated methane solvents, Kelley et al. showed that the absorption recovery has a component with the same lifetime as the A/A' state.[4] This occurs because the A/A' state decays back to the

X state causing a return of the ground state molecular absorption. In addition, a partial bleach remains at long times, because a fraction of the atoms do not geminately recombine. In the chlorinated methane solutions, the recovery extends beyond the delay range used in this experiment (Fig. 9), so that independent measurements of both the decay time and the long time bleach are not possible. However, the data is consistent with the A/A'-state lifetimes determined at other wavelengths, if a moderate long time offset is assumed (Table 2). The bleach component due to trapping in the A/A' state is a large fraction of the total bleach implying that 50% or more of the recombined molecules are initially trapped in this excited electronic state. In the alkane solutions, the shorter time recovery component which obscures the A/A'-state 635 nm absorption also obscures the bleach recovery from A/A'-state decay (Fig. 10). However, the data in these solvents is consistent with part of the recovery being due to A/A'-state decay. The long time bleach due to escaped atoms is easily measured in the alkanes and is included in Table 2.

The question of whether the A state, A' state, or both is being monitored can now be adressed. If the rate of exchange between the A and A' states is fast in the liquid, nearly all the population would reside in the lower A' state. On the other hand, if the exchange between A and A' states is slow and their decay rates back to the X state are not identical, a multi-exponential X-state recovery would be expected. Since the UV absorption, red absorption, and green bleach all show the same single exponential behavior, it appears that only one excited trap state is important.

The identity of this state is indicated by an ultraviolet

absorption in gas-phase iodine which has recently been assigned to the D'←A' transition (Fig. 1).[49] The liquid phase D'←A' spectrum can be approximated by assuming that it has the same gas-to-liqid shift and broadening as the D'←X transition (Fig. 11).[50] In the UV, the agreement between the predicted and experimental spectra (Fig. 11) shows that the long time absorption can be reasonably assigned to the D'←A' transition. The red absorption must also originate from the A' state, since only one trap state is important. Several final states with the proper energy and symmetry for red absorptions from the A' state exist, but it is not possible to decide which is the most important.[44] Abul-Haj and Kelley also conclude that the red absorptions are due to the A' state using somewhat different arguments.[6] Although this assignment is not definitive, only the A' state will be referred to in the following sections.

Intermediate Decays: X-State Vibrational Dynamics

In addition to the A'-state absorption, all the absorption curves show other features occurring at earlier times. At the red wavelengths (635-1000 nm), there is a component which both rises and decays quickly at long wavelengths, but which becomes slower at shorter wavelengths (Figs. 3 and 4). In the alkanes, this component is resolved at longer wavelengths, but at 635 nm its recovery is slow enough that it is difficult to distinguish from the A'-state absorption (Figs. 7, 8). The wavelength dependence of the rise and decay times implies a time dependent absorption spectrum which is initially peaked at long

wavelengths, but shifts to shorter wavelengths with time.

Just such a shifting absorption spectrum has been predicted to result from vibrationally excited molecules in the X state.[3,9,10,31] By a classical Franck-Condon argument, the maximum absorption strength occurs for a wavelength corresponding to a vertical transition between classical turning points. Since the X-state absorption is dominated by the B←X transition, the wavelength of maximum absorption for a given vibrational level can be related to the difference between the X and B potential curves (Figs. 1, 16). Thus when atoms first recombine in the X state and are highly vibrationally excited, their absorption will lie at wavelengths >1 μm. As they relax, the absorption maximum moves to shorter and shorter wavelengths, until it matches the normal ground state absorption when the molecules are completely relaxed. Since this is exactly the behavior experimentally observed, the early time component of the red absorptions can be assigned to molecules which initially recombine on the X state, but which are still vibrationally excited.

These arguments also imply that there should be a branch of the absorption spectrum of the vibrationally excited molecules on the short wavelength side of the ground state absorption spectrum.[31] This absorption arises from the vertical transitions starting on the inner turning point (Fig. 1) and will be weak since the molecule classically spends less time at this turning point. A weak absorption component with the correct timescale is seen at 400 nm in CCl_4 and hexane solutions (see e.g. Fig. 12). At the other UV wavelengths, absorption from excited vibrational levels is masked by other, stronger absorptions. Based on the classical Franck-Condon model and a knowledge

of the potential curves, an absorption at 400 nm arises primarily from vibrational levels between the levels responsible for 635 and 710 nm absorption and would be expected to show a time behavior intermediate between the behavior at these two wavelengths. This is, in fact, the case.

The effects of vibrational relaxation are also seen in the recovery of absorption at 500 nm. The curves for the chlorinated methane solutions (Fig. 9) show a short time component which recovers just after the vibrational component of the 635 nm absorption decays (Fig. 4). In previous work, this component has been interpreted as a direct measure of the cage recombination time.[2,4,26-28] However, the smooth progression of times for vibrational relaxation measured in the red to the time measured in the green indicates that this component actually represents the final stage of vibrational relaxation of those molecules which originally recombined on the X state. In the alkane solvents (Fig. 10), the A'-state electronic relaxation and the last stages of X-state vibrational relaxation occur on such similar timescales that separate recovery components are not distinguishable.

It is now possible to understand the origin of the unusual double peaked absorption curves seen in cyclohexane (Fig. 8). At the longest wavelengths, the curves are similiar to those in linear alkanes, with a slow component which has a decay time matching the A'-state lifetime deduced from the UV data. However, the vibrational component is slower than in the linear alkanes. At 710 and 635 nm, the vibrational relaxation component in cyclohexane is slow enough that it recovers more slowly than the A'-state lifetime. This leads to double peaked absorption curves in which the first peak results from the A'-state

absorption and the second peak from absorption due to lower vibrational levels of the X state.

Rapid Decays: B-State Predissociation Dynamics

The remaining features of the decay curves occur within the first 20 ps. First, although a large fraction of the bleach occurs with the pulsewidth-limited risetime, the maximum bleach does not occur until 20-50 ps later (Figs. 9, 10). It has been previously hypothesized that the bleach maximum is delayed because the initially populated B state has some absorption near 500nm.[2] This residual absorption would not disappear until the B state predissociates. The present data show that the bleach rise occurs in two stages, as required by this hypothesis.

During the same time period, there is a very strong absorption from 400-350 nm (Figs. 5a, 6a). The absorption rises quickly at all wavelengths, but the risetime is pulsewidth-limited only at 400 nm. In CCl_4, the absorptions at 400, 370 and 350 nm have progressively longer rise and decay times; hexane shows a similiar shift between 350 and 400 nm. At 350 nm, the other solvents have a delay in maximum absorption and a short decay component similar to that seen in CCl_4 and in hexane. Based on the pulse-limited rise at 400 nm, this absorption can be assigned to the first state populated, the B state. The decay time is then consistent with the predissociation timescale deduced from the 500 nm bleach recovery. The final state for the UV absorption would be either the β or the E states[51,52] (Fig. 1), both of which are at the correct energy and have the correct symmetry for an allowed transition

from the B state.

The wavelength dependence of the UV absorption kinetics are explained by vibrational relaxation within the B state. Using the same Franck-Condon arguments used to explain the effects of X-state vibrational relaxation, it can be seen that the absorption will be shifted to longer wavelengths in higher B-state vibrational levels (Fig. 1). Thus, the initially populated vibrational levels (v~12-14) will absorb strongly at 400 nm, and the absorption will decline both from predissociation and from relaxation to lower vibrational states. The absorption at 350 nm is strongest for low lying vibrational states, however, so the absorption does not reach a maximum until there has been some vibrational relaxation. The curves at 295 nm also show a small early component (Fig. 5, 6). Although in general it is similar to the early absorption seen from 350-400 nm, it appears to be somewhat too long (20-35 ps) to arise from the B state. At present the origin of this absorption is still uncertain.

In chlorinated solvents, the red absorptions (635-1000 nm) also show an early time (<20 ps) component. This component is clearest in the high resolution data in Fig. 15. This component becomes stronger at longer wavelengths, so it is undetectable at 635 nm, clearly resolvable at 760 nm, and dominant at 1000 nm. At 1000 nm, this component is so strong and the vibrational relaxation component so fast, that a faint, but reproducible, shoulder on the CCl_4 data is the only clue that two components exist. It is difficult to obtain precise information on this absorption, because it is so strongly mixed with the rise of the vibrational and A'-state components. However, its rapid rise and decay suggest that it arises from the B state.

Separation of Absorption Components

The slowly recovering absorption from A'-state molecules and escaped atoms complicate quantitative analysis of the faster X- and B-state dynamics. For this reason, the slower contributions were subtracted from the data. The A'-state decay times and absorption magnitudes, as well as the offsets from escaped atoms are fixed by the long time portions of the data (Tables 1 and 2). An exception occurs with alkane solvents at 500 nm, and in some cases at 635 nm, where the A'-state and X-state contributions are not well resolved. In these cases, subtractions were not performed.

The primary complication to the subtraction was the assignment of a risetime to the A'-state absorption. For simplicity, the rise was assumed to be exponential, although it probably has a more complicated functional form. The fast, smooth rising edge at 635 nm suggests an A'-state rise time which is definitely slower than 8 ps, but which is not much slower than 15 ps (Fig. 13). In addition, rise times as long as 20 or 25 ps are too slow to meet the beginning of the single exponential portion of the A'-state absorptions at 350 nm (Figs. 13 and 14). In particular, the absence of a dip in the 350 nm absorptions as the A' state rises indicates that this rise time cannot be much slower than the decay time of the B-state absorption at 350 nm (10-15 ps). Using these considerations, an A'-state rise time of 10-12 ps was found for all solvents.

Once the risetime, t_r, decay time, t_d, A'-state absorption magnitude, A, and long time offset, C, have been determined, the function:

$$A \exp(-t/t_d) - (A + C) \exp(-t/t_r) + C \quad (1)$$

which represents the A'-state and unrecombined atom contribution to the absorption was subtracted from the data. The curves in Figs. 4 and 7, as well as curves b and a in Figs. 13 and 14 respectively, are representative of the A'-state component which was subtracted. Although the results of the subtraction are somewhat sensitive in the first 10-15 ps to the assumptions made, they seem to be a reasonable, first-order separation of the decay components. Further details of this subtraction are found in Appendix A.

Typical subtraction results at red wavelengths are shown in Fig. 15 for CCl_4 solutions. The overall wavelength dependence of the vibrational absorption is clear, as well as the early time peak which may be due to absorption from the B state. Similar results (not shown) isolate the B-state component of the UV absorption. To quantify the X-state vibrational and B-state predissociation dynamics, the delay from zero time to the maximum and to the point where the absorption has decayed to 1/e of its maximum have been tabulated (Table 3). This method of characterization is not unique and caution must be exercised in comparing to other authors.[23]

Summary of the Model

A model which accounts for the absorption data can now be summarized. Initially, iodine molecules are placed in vibrationally excited levels of the B state (Fig. 1). There is an immediate drop in the absorption at 500 nm, since the B state has a smaller absorption cross section than the ground state at this wavelength (Figs. 9, 10). At the same time there is the immediate appearance of a new absorption band in the UV arising from the B state (Figs. 5, 6). As the B state predissociates and vibrationally relaxes during the next 10-15 ps, the absorption at 500 nm decreases even further, while the B-state UV absorption shifts to longer wavelengths and decays. Once the molecules have dissociated, the solvent dynamics forces them on to one of three routes: they may escape through the solvent to remain unrecombined, they may recombine on an excited state potential and become trapped in the A or A' states, or they may recombine on the X state. Those which have recombined on the X state vibrationally relax. Relaxation proceeds quickly through the upper part of the well, but more slowly near the bottom of the well, so that complete relaxation requires ~100 ps. As the relaxation proceeds, the X-state absorption spectrum shifts from the near IR toward the normal ground state absorption spectrum which peaks at ~520 nm. As the vibrational relaxation is completed, a portion of the ground state absorption at 500 nm recovers in ~100 ps (Figs. 9, 10). A'-state molecules can then be seen by their absorptions in both the red and UV portions of the spectrum (Figs. 3-8). In a time which varies from 60-3000 ps, these states decay back to the X state, causing the decay of A'-state absorptions and a return of the ground

state absorption at 500 nm. Those atoms which escape their original partner recombine on a microsecond time scale, and contribute to the long time ultraviolet absorption and to the long time absorption bleach at 500 nm.

Now that all the absorption features have been considered, it can be seen that the cage recombination of the dissociated atoms must proceed rapidly. As discussed in the last section, if there were a long delay between the predissociation of the B state and recombination, there would be a dip in the UV absorption between the time that the B-state molecules had disappeared and the A'-state molecules had reformed (Figs. 13, 14). In addition, the rapid rise on the absorption curves at 635 and 710 nm implies a rapid filling of the A'-state. Although there may be some contribution to the red rise from an early transient, it seems unlikely that the A'-state rises much slower than the red absorptions and that the additional transient adds on to give such a smooth curve (see Fig. 13). Finally, if molecules were reforming at the top of the X state over a long time period, it would not be possible to see a rapid decay of the population in the higher 8). Based on all these arguments, a limit of <15 ps can be placed on the time in which the majority of cage recombination occurs. This is nearly an order of magnitude faster than the time suggested by earlier experimental interpretations[2,4,26-28] and by some diffusional theories.[2,53,54]

D. Comparison to Previous Results

Previous observations of the bleach recovery and the red absorptions have disagreed with each other on both the experimental results and their interpretation.[2,4-10,26-28] The results presented here for the A'-state lifetime in chlorinated methanes are in good agreement with the results of Kelley et al.[4] Their initial results did not detect the vibrational component in the red absorptions, probably due to lower time resolution and signal-to-noise. More recently however, our reports of a vibrational component[12,13] have been confirmed in that laboratory.[6] In the alkanes, Kelley et al. reported A'-state lifetimes based on red decay curves in which the vibrational component was not resolved and they mentioned difficulties with signal size in these solvents. Thus, the somewhat shorter times reported here are probably more accurate, since they were derived from high signal-to-noise ultraviolet absorptions free from vibrational components.

The results of Bado et al. in the chlorinated methanes[7,8], however, are quite different than those reported here. Recent experiments by Abul-Haj and Kelley indicate that these discrepencies are not due to the different excitation wavelengths used.[6] The decay times of the red absorptions, although longer than in the alkanes, are not as long as reported here. Several factors in their experimental technique could have caused this discrepency. First, very concentrated iodine solutions, near saturation, were used, and we have seen distortions of UV absorption curves attributable to high I_2 concentrations. Abul-Haj and Kelley have also observed quenching of the A' state at high concentration attributed to $I_2^*(A') + I_2 \rightarrow I_4^*$.[6] In addition, I_2 dimers

and higher complexes form under these conditions.[42] Secondly, the long decay components seen in some solvents would not completely relax in the time between pulses (4 ns) in Bado et al.'s experiments. Finally, the formation of I_3^* has been observed at high sample concentrations within tens of nanoseconds after photodissociation,[5] and may cause artifacts when high pulse repetition rates are used.

In contrast to the data in chlorinated solvents, the more rapid alkane data of Bado et al.[7,8] are not significantly different from those presented here, if consideration is given to their lower time resolution (~30 ps). We resolve two components in the red absorption, one due to vibrationally relaxing X-state molecules, and the other due to A'-state molecules, which would be unresolvable in Bado et al.'s experiment. However, the vibrational component gives the overall curve a strongly wavelength dependent character, which accounts for their interpretation that the red absorption is entirely due to vibrationally relaxing X-state molecules. Although we are in agreement with the conclusions of Bado et al. on the importance of ground state vibrational relaxation, their data must be viewed with some reservation until the possible roles of I_3^*, I_4^*, and I_2-dimers in those experiments has been determined.

Chuang et al. reported a slight polarization anisotropy during the rise of the 532 nm bleach in hexadecane, which was attributed to rotational reorientation.[2] We have not reproduced this result. A rotational diffusion model predicts a reorientation time of 2.7 ps/cP for iodine.[55] Using zero-frequency solvent viscosities,[56] the reorientation times should range from 0.8 ps in hexane to 8.2 ps in hexadecane. Motion on the fast end of this range would be unresolved with the present time resolution, but motion on the slow end should be

for number sequence only

easily seen. However, the relaxation times predicted in high viscosity solvents such as hexadecane may be too long. The rotation may be sensitive to the high frequency viscosity, which can be expected to be lower than the bulk viscosity in long chain solvents. Thus it seems most likely that the reorientation time for the iodine is only 1-2 ps and that the polarization anisotropy cannot be seen with the current time resolution.

In several papers, attempts have been made to extract the quantum yield of non-geminately recombining atoms by comparing the maximum of the bleach in molecular absorption in the green to the long time loss of absorption.[2,4,26] This procedure assumes that no molecular states are absorbing when the bleach maximum is reached. With the present model for the reaction kinetics, this assumption is not necessarily justified, since at the bleach maximum molecules may be in the A or A' states, may not have completely predissociated, or may have vibrationally relaxed sufficiently to start reabsorbing. In addition, the strong solvent variation of the peak bleach strength reported in one paper are in disagreement with the values found here.[26]

E. Comparison with Theoretical Models

The preceeding sections have used the transient absorption data to develop a detailed qualitative picture of the photodissociation/recombination reaction. Using this model, quantitative data can be extracted on the elementary reaction steps. These results can be compared to existing theories for liquid-phase reaction dynamics and may help direct future theoretical developments. First, the experimental upper bound on the geminate recombination time is very useful in assessing the large amount of theoretical work on this process. Second, the time dependent absorption data on the vibrationally relaxing X-state population provides quantitative information on vibrational relaxation through a wide range of vibrational levels. On a rough level, solvent comparisons of the absorption data itself give evidence on the likely pathways for relaxation. For a more precise examination of vibrational relaxation, an approximate derivation of the actual population distribution from the absorption data is developed. Both the solvent dependent relaxation rates and the population distribution are compared with quantitative models of vibrational relaxation in this system. Finally, the two electronic relaxation processes, A'-state relaxation and B-state predissociation, are examined and compared with the few available theoretical models for electonic relaxation.

Recombination Dynamics

The aspect of iodine photodissociation which has received the most theoretical attention is the geminate recombination of dissociated atoms. Two methods have been used: hydrodynamic models which use only a few equations to represent the solvent's influence;[2,27,53,54,57-62] and molecular dynamics simulations, which calculate the exact motions of many solvent molecules.[63-65] It is interesting to ask whether the conclusion that recombination occurs in <15 ps is consistent with theoretical results and whether some theoretical approaches are more useful in understanding this result.

Hydrodynamic models have been popular, partly because of their computational ease and also because it is relatively easy to form simple, physical interpretations of the results. However, there are serious questions, both theoretical and practical, about the application of these equations to the dissociation dynamics of small molecules such as iodine. One objection is that the iodine mass is comparable to that of the solvent, while Langevin and related equations require that the solvent be light compared to the iodine.[66] In addition, the hydrodynamic equations only hold when the solute-solvent force correlation time is much shorter than the correlation time of the solute velocity. This condition is violated during the initial high velocity separation of the dissociating atoms. Even the MTGLE method, which attempts to reduce this problem, must introduce ad hoc "cage breakout" assumptions.[60] Thus hydrodynamic models cannot be applied to the early portions of the dissociation process, but are usually applied to the dynamics after the velocities have thermalized. Thus, the major part of

the recombination process may occur before the hydrodynamic models become applicable.

There are also serious practical problems in using hydrodynamic models to predict the time scale of geminate recombination. The results are very sensitive to the initial conditions, which are determined by the complicated early time dynamics. In addition, the other parameters commonly introduced, such as the solute atom diffusion constant and its distance dependence, the reaction diameter and the intrinsic reaction rate constant, are not independently known or are poorly defined. A wide range of recombination times can be obtained with reasonable parameters; estimates of the 50% recombination time have appeared from 1-150 ps.[53,57] Thus, hydrodynamic models do not provide a reliable prediction of the recombination time scale.

Molecular dynamics simulations of the photodissociation process provide a more promising approach to understanding geminate recombination. Although simulations to date have been limited to a small number of solvent molecules and to short simulation times, useful information has been obtained. The most striking conclusion is that geminate recombination should occur rapidly. Bunker and Jacobsen found that approximately 85% of the atoms recombined within 4 ps in their simulations.[63] In Murrell et al.'s work, 80% of all recombinations occurred in <5 ps over the entire range of densities examined.[64] Similarly, Lipkus et al. found that on the X-state potential, 50% of all recombinations were complete in <1 ps for all densities considered.[65] On the A-state potential, they found that the recombination lifetime was ~10 ps. Thus for recombination on both the X state and the A state, partitioning between free atoms and recombined molecules occurred on a

time scale of <10 ps. In support of these simulations, the quantum yields of escaped atoms as a function of density calculated from these simulations agree well with experimental measurements.[64,65]

These results indicate that the major portion of the recombination occurs on a short enough time scale that the use of hydrodynamic models is suspect. In addition, molecular dynamics, in contrast to hydrodynamics, makes a reasonably definitive prediction that recombination should occur in <10 ps. One reservation to these conclusions is that the role of multiple potential surfaces has not been included in the simulations. A recent model has found that the presence of multiple potential surfaces in iodine may slow the recombination rate by a factor of five, because the atoms may frequently recombine on one of the seven unbound potential surfaces.[67] Even considering the possible slowing effects of multiple surfaces however, the >100 ps recombination times previously reported[4,26,28] were hard to reconcile with the molecular dynamics results, while the time of <15ps deduced from the current measurements indicates that the molecular dynamics results are quite reasonable.

Vibrational Relaxation: Classical Analysis and the Relaxation Mechanism

Vibrational relaxation in liquids is poorly understood, especially between excited vibrational levels. The time dependent absorption spectrum of vibrationally excited iodine molecules is a rare source of information on this problem. In this section, a simple classical model of absorption from excited vibrational levels is used to compare

vibrational relaxation in different solvents. The results cast doubt on the theoretical prediction that vibration-to-vibration (V-V) transfer to the solvent dominates relaxation in the lower portion of the X-state well. It is suggested that vibration-to-rotation (V-R) mechanisms should be included or that vibration-to-translation (V-T) transfer has been underestimated. The following section discusses corrections to the classical model and performs a more precise analysis of vibrational relaxation in CCl_4 solution.

In a classical Franck-Condon picture, only vertical transitions between turning points are allowed (Fig. 1). Since the B←X transition dominates iodine's visible absorption, the difference potential as a function of X-state vibrational energy can be used to associate an X-state vibrational energy with each absorption wavelength (Fig. 16). Using this classical approximation, Fig. 17 shows the vibrational dynamics derived from the absorption component due to vibrationally excited molecules. In all of the solvents studied, the vibrational relaxation time is substantial; 50-200 ps are required to reach the ground vibrational level. Relaxation through the upper half of the potential, however, is fairly rapid with the peak absorption from levels with ~6000 cm^{-1} of vibrational energy appearing in 10-15 ps and decaying to 1/e of their peak value by 20-30 ps after photodissociation. Among the chlorinated solvents, the absorption at 710 nm (v~9, E_{vib}~1800 cm^{-1}) peaks and decays most slowly in CCl_4, somewhat faster in $CHCl_3$, and is almost a factor of three faster in CH_2Cl_2. In the alkane solvents, the three linear alkanes show virtually identical relaxation rates, while cyclohexane is substantially slower.

Nesbitt and Hynes have calculated the relaxation rate for iodine in

CCl_4 using a classical trajectory simulation and assuming uncorrelated binary collisions with the solvent.[3] They found that V-T transfer is relatively rapid in the upper part of the potential, but that relaxation to the ground vibrational level takes more than one nanosecond if the solvent has no internal vibrations. Brooks, Balk, and Adelman reach a similiar conclusion using an MTGLE model.[29] When near-resonant vibration-to-vibration (V-V) energy transfer to the 217 cm^{-1} mode of CCl_4 was included, Nesbitt and Hynes showed that the relaxation in lower levels proceeded more rapidly, with ground state recovery in ~100 ps. Using molecular dynamics simulations, Bado et al. have also predicted a strong dependence of the vibrational relaxation rate on near-resonant energy transfer to the vibrational modes of the solvent.[31]

The present measurements in chlorinated solvents do not behave according to simple V-V energy transfer predictions. The lowest frequency modes in CCl_4, $CHCl_3$, and CH_2Cl_2 are 217 cm^{-1}, 261 cm^{-1}, and 282 cm^{-1} respectively.[68] The iodine molecular vibrational frequency is 213 cm^{-1} in the ground vibrational level and decreases to 170 cm^{-1} at 6000 cm^{-1} above the ground level.[69] Thus the energy gaps for V-V transfer in the lower half of the well are 4-47 cm^{-1} in CCl_4, 48-91 cm^{-1} in $CHCl_3$, and 69-112 cm^{-1} in CH_2Cl_2. These changes between the solvents are large compared to the 20-25 cm^{-1} resonant transfer width.[70] Thus the V-V relaxation times would be expected to increase in the orde. $CH_2Cl_2 > CHCl_3 > CCl_4$. A calculation of resonant energy transfer rates[70] using the expression which Nesbitt and Hynes applied to CCl_4,[3] confirms that the expected V-V rates should be 3-4 times slower in $CHCl_3$ and 8-10 times slower in CH_2Cl_2 through the entire lower half of the X-state potential. In contrast with this prediction, the vibrational relaxation

time is actually slowest in CCl_4, slightly faster in $CHCl_3$ and dramatically faster in CH_2Cl_2 (Fig. 17). This suggests either that V-V transfer is not important in any of the chlorinated methane solvents or at least that other mechanisms dominate the rates in $CHCl_3$ and CH_2Cl_2.

One alternative mechanism is vibration-to-rotation (V-R) transfer. In the gas phase, V-R transfer is greatly enhanced in small hydrogen containing molecules, because of their low moment of inertia. In fact, the self-relaxation in gas-phase CH_2Cl_2 has been found to be dominated by V-R transfer.[71] Moore has proposed a simple model which treats V-R transfer in the same manner as V-T transfer, except the rotational velocity of the hydrogen atom is substituted for the translational velocity of the entire molicule.[71] The relevent parameter in this model is an effective rotational mass, defined as the lowest moment of inertia divided by the longest moment arm squared. As with V-T transfer, "lighter" molecules increace the relaxation rate. In the present case, the rotational masses are 142, 60, and 8.5 amu in CCl_4, $CHCl_3$, and CH_2Cl_2 respectively.[72,73] The low rotational mass compared to the total mass for $CHCl_3$ and particularly for CH_2Cl_2 suggests that V-R transfer is more effective than V-T transfer. Furthermore, the trend in the rotational masses matches the trend in relaxation rates. These facts indicate that transfer of vibrational energy to rotation-like motion of the solvent may determine the iodine relaxation rates in these systems.

Also, the role of V-T transfer in lower vibrational levels should not be entirely rejected on the basis of theoretical modeling. The ability to predict liquid-phase vibrational relaxation rates, especially between excited vibrational levels, is not well established. In

addition, models of V-T transfer are extremely sensitive to the interaction potentials assumed.[74]

In contrast with the results in chlorinated methane solvents, the vibrational relaxation rate in alkane solvents behaves more nearly as expected for V-V transfer. As Bado et al. have pointed out, the ring structure in cyclohexane substantially reduces the density of low frequency torsional and vibrational modes in comparison with the linear alkanes.[7] With fewer low frequency modes in proximity to the iodine vibrational frequency, the vibrational relaxation in the lower part of the well should be slower in cyclohexane than in normal hexane. This is the observed behavior. In the straight chain alkanes, the relaxation rate does not vary with the length of the alkane chain. This may occur because the number of low frequency modes which can effectively interact with the iodine does not change with chain length, since the number of low frequency modes per unit volume is approximately constant.

The contrasting results for vibrational relaxation rates in these different solvents demonstrate that the role of V-V transfer is not yet understood. Studies in simpler solvents such as Xe and CO_2 should help to clarify the role of V-T and V-R transfer and thereby contribute to an understanding of V-V transfer. The bleach recovery in fluid Xe has been previously observed,[28] but preliminary measurements in this laboratory show different dynamics. More work is necessary to understand vibrational relaxation dynamics in this simple solvent.

C. Vibrational Relaxation: Quantum Spectral Analysis

So far the vibrational absorptions have been discussed assuming that the absorption at a given wavelength can be directly associated with the population at a particular level of vibrational excitation. This assumption is based on a crude, classical Franck-Condon model and oversimplifies the true quantum mechanical spectrum. In order to assess the importance of quantum effects, a calculation of the absorption strength for a given wavelength versus the amount of vibrational energy in the X state was performed. Franck-Condon factors and R-centroids were calculated for the B←X, $^1\Pi_u$←X, and A←X transitions. A continuous spectrum was obtained for each X-state vibrational level by assuming that each transition was broadened to a 200 cm^{-1} gaussian line in the liquid phase. Broadening of this magnitude is consistent with the absence of vibrational structure in the visible absorption spectrum. The final results are only weakly sensitive to the extent or the form of the broadening function. The strong R-centroid dependence of the B←X transition moment was included.[75] Further details on the calculation are given in Appendix B. Figure 18 shows examples of the results.

The quantum mechanical transition strengths have several features in common at all wavelengths. The transition strengths all have a strong peak which lies slightly higher in vibrational energy than the classical prediction, because the main peak of the vibrational wavefunction lies inside the classical turning point. On the high vibrational energy side of this peak there is a long, slowly decaying tail, due to overlap of the oscillatory portions of the wavefunctions. Because of this tail, the absorption at a given wavelength should start

to rise before the population has relaxed as far as the point of classical absorption. By the same reasoning, the absorption bleach will begin to recover before the population reaches the bottom of the potential well. In contrast, the transition strength drops sharply on the low vibrational energy side of the main peak, due to the rapid drop in the wavefunction outside the classically allowed region. This implies that the absorption decay at each wavelength is a reasonably accurate indication of the population which has relaxed below the classical absorption point. Finally, the width of the main peak in the transition strengths broadens as the wavelength of the transition increases.

Incorporating the more accurate quantum transition strengths into the analysis of the vibrational absorptions can be done as follows. The spectrum at each time can be represented as:

$$A(\lambda,t) = \int_0^\infty dE\ S(\lambda,E)\ P(E,t) \qquad (2)$$

where $A(\lambda,t)$ is the absorption data at a given wavelength, λ, and delay time, t; $P(E, t)$ is the population as a function of vibrational energy, E; and $S(\lambda, E)$ is the transition strength. Exactly inverting this expression to find P from S and A is difficult when P and S are arbitrary functions and A is only sampled at a few values of λ. However, consideration of the actual characteristics of P and S allows an approximate inversion of this formula which includes the major corrections from the quantum calculation.

The energy scale is first broken into segments, each of which isolates the transition strength peak for one wavelength. In CCl_4

enough wavelengths were measured that these regions cover the energy region from 0-8000 cm^{-1}. Next, at each probe wavelength the function S is approximated by a function S' which is constant over each energy region (Fig. 18). If the analysis is restricted to times when all the population has relaxed below 8000 cm^{-1}, S' can be set equal to zero above 8000 cm^{-1}. Equation 2 now gives

$$A(\lambda,t) \sim \sum_{j=1}^{n} S_j'(\lambda) \int_{E_{j-1}}^{E_j} dE\ P(E,t) \tag{3}$$

or

$$A_\lambda(t) \sim \sum_{j=1}^{n} S_{\lambda j}'\ P_j(t) \tag{4}$$

where $S_{\lambda j}'$ is the value of S' at wavelength λ in energy region j, E_j is the upper edge of energy region j (E_0=0), and:

$$P_j(t) = \int_{E_{j-1}}^{E_j} dE\ P(E,t)$$

If the energy regions are well chosen, S' duplicates the important features of S, and this approximation can be expected to be a good one. If at each time A is known at n values of λ, and n energy regions are selected, the problem reduces to a set of n equations in n variables, which can be solved by standard matrix techniques (Eq. 4). Several factors which are important in obtaining a good inversion are discussed in detail in Appendix C.

Figure 19 shows the results of applying this procedure to the CCl_4

data. The average population density for each energy region is plotted at the center of that region. Prior to 50 ps, reliable results cannot be obtained, partly because some of the population has not relaxed below 8000 cm^{-1}, and partly because of interference from other early time absorptions. From 50–200 ps, the total population remains constant to within 10% even though there is no explicit constraint on the population from one time point to the next. It is encouraging that this simple inversion produces reasonable results and particularly that it conserves total population. Its success indicates that the assignment of the early absorption features to vibrational relaxation in the X state is quantitatively consistent with the absorption data at all wavelengths.

Nesbitt and Hynes have calculated the time-dependent I_2 vibrational population distribution using a binary collision model.[3] From the calculated distribution, they depredicted the recovery of the ground state absorption, which can be compared directly to the experimental results at 500 nm (Fig. 15). The calculated recovery has the correct qualitative features, but is faster than the actual decay. A more complete comparison can be made by directly comparing their population distribution (Ref. 4, Fig. 10) and the experimentally derived distribution (Fig. 19). The experimental distribution at 50 ps has relaxed further than the calculated distribution. This indicates that relaxation is faster than predicted through the upper part of the well. On the other hand, the experimental distribution still has a significant unrelaxed tail at 150 ps when the model system is completely relaxed. Thus relaxation of the last ~2000 cm^{-1} proceeds more slowly than predicted. These discrepancies indicate a weaker dependence of relaxation rate on vibrational level and less of a "bottleneck" effect

than that found in Nesbitt and Hynes's model. This bottleneck arose because V-T transfer was predicted to slow below v~60, while V-V transfer was not predicted to become efficient until below v~40 (Ref. 3, Fig. 9). The disagreement of the calculated and experimental distributions suggests that the relative roles of V-T and V-V transfer at various levels of vibrational energy are not yet understood.

In order to assess the importance of different quantum corrections to the transition strengths, the population distribution at 50 ps was also calculated with the classical model and with a model incorporating the quantum mechanical peak shifts and broadening, but without the high energy tail (Fig. 20). Although the classical model correctly gives the general features of the population distribution, a more sophisticated treatment is needed for even semi-quantitatively correct results. In particular, ignoring the high vibrational energy tail in the transition strengths causes an overestimation of the population at lower vibrational levels.

Lifetime of the A' State

The lifetime of the A' state varies dramatically in the solvents studied, from 500-2700 ps in chlorinated solvents to 65 ps in alkane solvents. In models of the A'-state lifetime, it has been generally assumed that the molecule must be activated high in the well to a region near the curve crossing with the X state in order to relax. Thus, changes in the A'-state lifetime may result from either changes in the height of the crossing point or from changes in activation rate. Kelley

et al. proposed that the A'-state well depth varies as a result of changes in the molecular solvation energy as compared to the atomic solvation energy.[4] They further proposed that the solvation energy is largely due to charge-transfer interactions, and that the well depth can be related to the ionization potential of the solvent. As a result the A'-state lifetime should be related to the ionization potential of the solvent, and in fact the A'-state lifetimes are roughly ordered according to the ionization potentials. One difficulty with this proposal is that although charge-transfer transition wavelengths have been related to the solvent ionization potential, this relationship is based on the energy of the upper ion-pair state. The connection between solvent ionization potential and the lower-state solvation energy is not clear.[35] It is even less clear how the difference between molecular and atomic solvation energies is affected by the solvent's ionization potential. As a test of the model it can be assumed that the activation energy (well depth) depends linearly on the solvent ionization potential and that the rate follows an Arrhenius law. With these assumptions, the log of the lifetimes should be linearly related to the solvent ionization potential. Figure 21 shows that the correlation is poor, so that the solvent ionization potential does not appear to be the most important parameter in determining the A'-state lifetime.

Dawes and Sceats[62] have proposed that the electronic state curve crossing rate and the diffusive motion up the well to the crossing region are solvent dependent. Using a simple model for both the diffusive motion and the curve crossing, they conclude that the rate is transport limited. Thus the lifetime should decrease in lower viscosity solvents. The model predicts A'-state lifetimes which are much longer

than the experimental results. If it is assumed that our assignment is incorrect and that the A state is actually being observed, the predicted timescale is more reasonable (Fig. 22). Still, the simulation results do not fit well. An approximate, analytical model predicts the general trend for the chlorinated solvents, but this agreement is hard to interpret, since the analytical model is justified based on its ability to match the simulation results. An even larger problem is the fact that the lifetimes in the alkane solutions are all approximately the same, even though the viscosity changes by a factor of ten. Dawes and Sceats have proposed that the frequency dependence of the viscosity may be important and that the high frequency viscosity would be similiar in all the alkanes.[62] In any case it is clear that the zero frequency shear viscosity does not correlate with the A'-state lifetime. At this stage, it appears that none of the essential features which determine the A'-state lifetime are well understood.

Predissociation

The early component of the UV absorptions (Fig. 5a, 6a) is due to absorption from the excited B state. The absorption decay at any given wavelength is due to both vibrational relaxation and predissociation. The situation is complicated by the fact that the predissociation rate is likely to depend on the vibrational level.[76,77] Thus it is not possible to accurately separate these two contributions to the decay. However, a rough timescale of 10-15 ps for predissociation can be obtained. There are no dramatic changes in different solvents.

There is virtually no theoretical work on liquid-phase predissociation to compare to, but comparisons can be made to gas-phase measurements.[76-78] For the vibrational levels initially excited in this experiment, the probability of predissociation per gas-phas kinetic collision is 0.8-0.2 for Xe, which is similiar in size and mass to CCl_4.[76] By comparison, the liquid-phase lifetime of ~10 ps, corresponding to ~100 "collisions",[3] is suprisingly long. The observed lifetime may be explained by a large drop in the predissociation probability for vibrational levels below v~7.[76] It is clear that further work is nessesary to understand this phenomenon.

F. Conclusion

A detailed picture of the steps involved in a simple dissociation/recombination reaction has been developed from picosecond absorption studies extending from the near infrared into the UV. The data present convincing evidence that the geminate recombination of dissociated atoms is fast (<15 ps). This conclusion is consistent with molecular dynamics simulations. In contrast it is argued that hydrodynamic approaches to geminate recombination involve questionable theoretical assumptions and produce few useful predictions. Many theories have predicted a long time tail in the recombination probability. However, the current model is able to explain all the available absorption data assuming that all the recombination is rapid. While a long time tail in the recombination probability cannot be rigorously excluded, there is no evidence to suggest that if one exists, it accounts for more than a minor fraction of the total recombination.

Vibrational and electronic relaxation of the recombined molecule have been found to be much slower than the initial recombination. The evolution of the vibrationally excited population distribution has been approximated using realistic, quantum mechanical spectra of vibrationally excited molecules. Neither the population distribution nor comparisons of vibrational relaxation rates in different solvents provide evidence for resonant energy transfer to solvent vibrational modes in chlorinated solvents, in contrast with predictions. On the other hand, resonant vibrational energy transfer may be more important

in alkane solvents. In addition, the few models available to describe A'-state electronic relaxation are unable to explain the 40-fold range of lifetimes observed in different solvents. No theories have yet directly adressed the B-state electronic relaxation rate and its relative lack of solvent dependence.

In conclusion, this study has presented a detailed qualitative picture of iodine photodissociation and has made significant steps toward a quantitative understanding of the reaction processes. However, the study of molecular dissociation and recombination in liquids is still a fertile area for further theoretical and experimental work. Large scale molecular dynamics simulations should help to give a better understanding of the solvent's role in geminate recombination. Basic developments are required in the theory of solvent-induced predissociation and electronic curve crossing. The development of these theories will benefit from new temperature and density dependent studies on iodine photodissociation. Experimental work is also needed in simple mono- and di-atomic solvents to understand the relative roles of V-V and V-T vibrational energy transfer. In addition, experiments with excitation to the directly dissociative A state (~680 nm, see Fig. 1) should allow direct observation of the geminate recombination event. It may be hoped that the deeper understanding of the iodine photodissociation reaction which will emerge from further work will provide a basis for a general understanding of liquid-phase chemical dynamics.

Appendix A. Subtraction of the A'-State Absorption

Since the recombination dynamics is completed rapidly after predissociation (Sec. III E), the B-state decay time, and the A'-state and escaped-atom rise times are very similar. Therefore, the offsets at UV and green wavelengths, both due to atoms which do not recombine, were assumed to form with the same rise time as the A'-state (see Eq. 1). In addition, in order to quantitatively assign the X-state vibrational dynamics based on the green and red transient curves, it was helpful to remove the B-state absorption which occurs at early time at 500 nm. Assuming that the decay time of the B-state absorption at 500 nm is set equal to the A'-state rise time, the B-state absorption was represented by $B \exp(-t/t_r)$. This term was subtracted from the 500 nm bleach curves, along with Eq. 1. The magnitude, B, is somewhat arbitrary, but has only a small effect on the subtracted data for times longer than 20 ps, where the vibrational analysis is focussed.

Appendix B. Transition Strength Calculations

The rotationless potential curves[24,45,69,79] and transition moments[32,75] are well known for the iodine X, B, A, and $^1\Pi_u$ states. Evidence suggests that the potentials are not strongly perturbed in the liquid.[80] Analytical approximations to these curves were made as follows:

$$V_X(R) = 14600\,[\,1 - e^{-1.85(R-2.67)}\,]^2$$

$$V_B(R) = 5000\,[\,1 - e^{-1.70(R-3.03)}\,]^2$$

$$|\mu_e|_{X\to B}(\bar{R}) = \begin{cases} 1.62\,\bar{R} - 3.51\ ; & 2.5 < \bar{R} < 3.1\ \text{Å} \\ -1.745\bar{R} + 6.91\ ; & 3.1 < \bar{R} < 3.3\ \text{Å} \\ -0.781\bar{R} + 3.74\ ; & 3.3 < \bar{R} < 4.6\ \text{Å} \end{cases}$$

$$V_A(R) = \begin{cases} -3241 + 2.958\times10^8 / R^{11} & ;\ R < 2.7873\text{Å} \\ 1100\,[\,1 - e^{-2.95(R-3.056)}\,]^2 & ;\ R > 2.7873\text{Å} \end{cases}$$

$$|\mu_e|_{X\to A} = 0.202\ \text{D}$$

$$V_{^1\Pi_u}(R) = \begin{cases} \text{as in Ref. 24} & ;\ R > 4.200\ \text{Å} \\ -180 & ;\ R > 4.200\ \text{Å} \end{cases}$$

$$|\mu_e|_{X\to {}^1\Pi_u} = 0.369\ \text{D}$$

where R is measured in Å, energy is in cm^{-1}, and $\bar{R}$ is the R-centroid. The X-state Morse parameters were chosen to optimize the fit to the outer limb of the RKR potential, since this is most important to the Franck-Condon calculations. The use of approximate potentials will not reproduce the state-to-state interference effects,[81] but these effects should be largely averaged out in the liquid. The bound Morse wavefunctions were calculated analytically.[82] The wavefunctions were calculated for v=0-50 in the X state and for all bound levels in the

upper states. For the unbound states, wavefunctions were calculated every 50-60 cm^{-1} by integrating Schrodinger's equation from 2.2 Å outward. Integration was carried out until the wavefunction reached its asymptotic behavior, so proper normalization could be performed.[83] Franck-Condon and R-centroid integrations were done from 2.2-3.74 Å at a 0.003 Å spacing.

The actual calculation was done in several stages. First, the program MWFUN calculated the Morse oscillator wavefunctions for each state using the subroutine MORSE, which contains the main algorithm. MORSE uses the function B repeatedly in its calculation. The program INTG1 calculated the wavefunctions for the unbound portions of the potentials. Franck-Condon factors and R-centroids were then calculated from the wavefunctions using the program FCFACT. The program VIBDIS then found the relative transition strength as a function of vibrational energy at a given absorption wavelength using the output of FCFACT. For the X→B transition, VIBDIS also calculated the R-centroid dependent transition moment. The transition strengths resulting from continuous and bound portions of the potentials, as well as from different transitions were then added using the program TRANAD. The FORTRAN code for each of these programs follows.

```
      PROGRAM MWFUN
C
C     THIS PROGRAM CREATES A FILE CONTAINING MORSE OSCILLATOR
C     WAVEFUNCTIONS IN STATES OF I2.  THE FIRST 10 WORDS OF THE FILE
C     CONTAIN A HEADER.  THE WAVEFUNCTIONS ARE STORED IN ACCENDING
C     VIBRATIONAL NUMBER.  SUBROUTINE MORSE (ON FILE MORSEB) IS
C     USED TO CALCULATE THE WAVEFUNCTIONS.  MB
C
      IMPLICIT INTEGER (V)
      INTEGER STATE
      REAL M
      LOGICAL ERR
      DIMENSION IDENT(3), WFUNCT(512)              !MUST MATCH NSTEP
      COMMON /MBLK/ WFUNCT, R1, STEP, NSTEP, K
C
C         PARAMETERS DEFINING THE CALCULATION
      R1 = 2.2     !INNER STARTING PT OF WFUNCT (ANGSTROMS)
      STEP = 0.003          !SPACING AT WHICH WFUNCT IS CALCULATED
      NSTEP = 512 !NUMBER OF PTS IN WFUNCT
C
C         GET STATE TO BE CALCULATED
100   PRINT 105
105   FORMAT ('$STATE TO BE CALCULATED (X, B, A): ')
      ACCEPT 110, STATE
110   FORMAT (1A)
      IF (STATE.EQ.'X') GOTO 115
      IF (STATE.EQ.'B') GOTO 120
      IF (STATE.EQ.'A') GOTO 125
      PRINT *, 'PARAMETERS NOT IN PROGRAM - TRY AGAIN'
      GOTO 100
C
C         X STATE PARAMETERS
115   RE = 2.67                     !EQUILBRIUM DISTANCE (ANGSTROMS)
      A = 1.85                      !MORSE PARAMETER (1/ANGSTROMS)
      D = 14600.                    !DISSOCIATION ENERGY (1/CM)
      K = 775                               !CALCULATION SCALING FACTOR
      GOTO 150
C
C         B STATE PARAMETERS
120   RE = 3.03                     !EQUILBRIUM DISTANCE (ANGSTROMS)
      A = 1.70                      !MORSE PARAMETER (1/ANGSTROMS)
      D = 5000.                     !DISSOCIATION ENERGY (1/CM)
      K = 420                               !CALCULATION SCALING FACTOR
      GOTO 150
C
C         A STATE PARAMETERS
125   RE = 3.056                    !EQUILBRIUM DISTANCE (ANGSTROMS)
      A = 2.95                      !MORSE PARAMETER (1/ANGSTROMS)
      D = 1100.                     !DISSOCIATION ENERGY (1/CM)
      K = 74                                !CALCULATION SCALING FACTOR
      GOTO 150
C
150   M = 89.735                    !REDUCED MASS (AMU)
      HBAR = 1.0536E-27
```

```
      G = 2. * SQRT(2. * M * D) * 1.8162E-28 / (A * HBAR)
C
C         GET RANGE OF V TO BE CALCULATED
20    PRINT 15
15    FORMAT ('$ENTER INITIAL AND FINAL VIBRATIONAL LEVELS: ')
      ACCEPT *, VI, VF
      IF (VF.GE.VI) GOTO 25
      PRINT *, 'WRONG ORDER. TRY AGAIN.'
      GOTO 20
C
C         OPEN OUTPUT FILE
25    PRINT 30
30    FORMAT ('$COMPLETE OUTPUT FILE NAME ')
      CALL ASSIGN (1, DUMMY, -1)
      PRINT 32
32    FORMAT ('$FILE IDENTIFIER - ')
      CALL GETSTR(5, IDENT, 4)
C
C         WRITE HEADER
      WRITE (1) (IDENT(J), J = 1,2)        !IDENTIFIER
      WRITE (1) VI, VF
      WRITE (1) R1, STEP, NSTEP
      WRITE (1) 0                    !EXTRA WORD
C
C         CALCULATE AND STORE WAVEFUNCTIONS
      PRINT *, 'TYPE Q TO INTERUPT PROGRAM'
      DO 35 V = VI, VF
      PRINT *, 'V = ', V
      CALL MORSE (RE, A, G, V, D) !WFUNCT PASSED THROUGH COMMON
      DO 33 J = 1, NSTEP
33    WRITE (1) WFUNCT(J)
      ITEST = IPEEK ("177562)              !LATEST KEYBOARD ENTRY
      IF (ITEST.EQ."121) GOTO 40
35    CONTINUE
C
C         CLOSE FILE
40    CLOSE (UNIT = 1)
      STOP
      END
```

```
      SUBROUTINE MORSE(RE, A, G, V, D)
C
C     THIS SUBROUTINE CALCULATES THE WAVEFUCTION, WFUNCT, FOR
C     THE VIBRATIONAL LEVEL, V, OF A MORSE OSCILLATOR.  THE
C     MORSE POTENTIAL IS DEFINED AS:
C
C       E(R) = D * [EXP[ -A(R - RE)] - 2 EXP[ -A(R - RE)]]
C         D = DISSOCIATION ENERGY
C         RE = EQUILBRIUM DISTANCE (ANGSTROMS)
C         A = W SQRT(M/2D) (1/ANGSTROMS)
C         W = VIBRATIONAL FREQUENCY AT BOTTOM OF V
C         M = REDUCED MASS OF OSCILLATOR
C         G = 2C = 2 * SQRT(2MD) / (A * hbar)
C
C     THE SUBROUTINE REQUIRES THE FUNCTION B.
C
      INTEGER V
      DIMENSION WFUNCT(512)        !SHOULD MATCH NSTEP
      COMMON /MBLK/ WFUNCT,R1,STEP,NSTEP,K
C
C     ***** FUNCTIONS *****
C
      X(Z) = G * EXP(-A * (R - RE))
C
C     ***** CONSTANTS *****
C
      DELTA =     1.E-10           !STOP CALCULATION WHEN WFUNCT < DELTA
      C2 = 0.6316188               !1/ SQRT(SQRT(2 PI))
C
C     ***********************
C
C         INITIALIZE !FUNCT
      DO 15 J = 1, NSTEP
15    WFUNCT(J) = 0.
C
C         FIND TURNING POINTS
      V12 = V + 0.5
      C1 = SQRT(4 * (G * V12 - V12**2) / G**2)
      RINNER = RE - (ALOG(1. + C1) / A)   !INNER TURNING POINT
      ROUTER = RE - (ALOG(1. - C1) / A)   !OUTER TURNING POINT
C
C     ***** CALCULATE WFUNCT *****
C
      CV = C2 * SQRT(A * (G - 1. - 2 * V))         !R INDEPENDENT PART
      INSTEP = INT((RINNER - R1) / STEP) + 1       !# OF PTS. R1-RINNER
C
C         FIRST CALCULATE FROM RINNER IN TOWARD R1
      DO 20 J = INSTEP, 1, -1
      R = R1 + (J - 1) * STEP
D     PRINT *, '*', X(R)
      WFUNCT(J) = CV * B(X(R), V, G, K)
      IF (ABS(WFUNCT(J)) - DELTA) 25,25,20         !STOP IF WFUNCT<DELTA
20    CONTINUE
C
```

```
C         NEXT CALCULATE FROM RINNER OUTWARD
25      DO 30 J = INSTEP + 1, NSTEP
        R = R1 + (J - 1) * STEP
D       PRINT *, X(R)
        WFUNCT(J) = CV * B(X(R), V, G, K)
        IF (R - ROUTER) 30, 30, 35  !CONTINUE IF RINNER< R <ROUTER
35      IF (ABS(WFUNCT(J)) - DELTA) 40,40,30        !STOP IN WFUNCT<DELTA
30      CONTINUE
C
40      RETURN
        END
```

```
C
C
C
      FUNCTION B(X , N, G, KT)
C
C     CALCULATES THE FUNCTION:
C
C     B = SQRT(N!) * EXP{-X + [G - 2N + 1] LN(X) + [G - N]
C                     - [G - N - 1/2] LN(G - N)} * L(G - 2N +1, N, X)
C
C     WHERE L IS THE LAGUERRE POLYNOMIAL.  A RECURSION FORMULA IS
C     USED.  FOR USE WITH SUBROUTINE MORSE IN CALCULATING MORSE
C     OSCILLATOR WAVEFUNCTIONS.
C
      REAL M
      SRTE = 1.648721                 !SQUARE ROOT OF E
      E = 2.718282                    !E
C
      H(Y) = EXP(((Y - 0.5) * ALOG(Y) / 2.) - K)  !FUNCTION
C
      SCALE = 0.
      K = KT
C
C         CALCULATE B(N = 0)
10    B1 = EXP((G - X + (G - 1.) * ALOG(X) - (G - 0.5) * ALOG(G)
     1 + SCALE) / 2.)
      IF (N) 15,20,23
15    PRINT *, 'ERROR IN CALLING B. N < 0'
      STOP
20    B = B1                                  !B(X, 0, G)
      RETURN
C
C         RESCALE IF B1 UNDERFLOWS
23    IF (ABS(B1).GT.5.0E-39) GOTO 25
22    SCALE = SCALE + 20.
      PRINT *, ' SCALE =', SCALE
      GOTO 10
C
C         CALCULATE B(N = 1)
25    H0 = H(G - 1.)
      H1 = H(G)
      D = 1. / (X * SRTE)
      V = G - 2. * N - 1.
      S2 = 1. + V - X
      B = S2 * D * H1 * B1 / H0    !B(X, 1, G)
      IF (N.EQ.1) RETURN
C
C         INITIALIZE REMAINING PARAMETERS
      F = 1. / (X * X * E)
      RTI = 1.
      M = G - 1.
      S1 = V
C
      M1 = 50
```

```
      IF (N.LE.50) N1 = N
D     PRINT *, '    B1=', B
C
C         RECURSION FOR B(1 < N < 51)
      DO 30 I = 2, N1
      M = M - 1.              !M = G - I
      S1 = S1 + 1.                    !S1 = I - 1 + V
      S2 = S2 + 2.                    !S2 = 2I + V - 1 - X
      H2 = H1                         !H2 = H(M + 2)
      H1 = H0                         !H1 = H(M + 1)
      H0 = H(M)
      RTI1 = RTI              !RTI1 = SQRT(I - 1)
      RTI = SQRT(FLOAT(I))
      B2 = B1                         !B2 = B(N = I - 2)
      B1 = B                          !B1 = B(N = I - 1)
      A3 = RTI * H0
D     PRINT *, 'S2= ', S2, ' H1=', H1, ' D= ', D
      A1 =  S2 * D * H1 * B1
      A2 = S1 * RTI1 * F * H2 * B2
D     PRINT *, 'A1= ', A1, ' A2= ', A2, ' A3= ', A3
      B = (A1 - A2) / A3  !B = B(N = I)
D     PRINT *, 'B(', I, ')=', B
30    CONTINUE
C
C         RESCALE K
      IF (N.LE.50) GOTO 100
      K = K - 115
      H1 = H(M + 1)
      H0 = H(M)
C
C         RECURSION FOR B(50 < N)
      DO 40 I = 51, N
      M = M - 1.              !M = G - I
      S1 = S1 + 1.                    !S1 = I - 1 + V
      S2 = S2 + 2.                    !S2 = 2I + V - 1 - X
      H2 = H1                         !H2 = H(M + 2)
      H1 = H0                         !H1 = H(M + 1)
      H0 = H(M)
      RTI1 = RTI              !RTI1 = SQRT(I - 1)
      RTI = SQRT(FLOAT(I))
      B2 = B1                         !B2 = B(N = I - 2)
      B1 = B                          !B1 = B(N = I - 1)
      A3 = RTI * H0
D     PRINT *, 'S2= ', S2, ' H1=', H1, ' D= ', D
      A1 =  S2 * D * H1 * B1
      A2 = S1 * RTI1 * F * H2 * B2
D     PRINT *, 'A1= ', A1, ' A2= ', A2, ' A3= ', A3
      B = (A1 - A2) / A3  !B = B(N = I)
D     PRINT *, 'B(', I, ')=', B
40    CONTINUE
C
100   IF (SCALE.EQ.0.) RETURN
      B = B * EXP(-SCALE / 2.)
D     PRINT *,  '    B=', B
```

```
      PROGRAM INTG1
C
C     THIS PROGRAM INTEGRATES SCHROEDINGERS EQUATION
C     OUTWARD FROM THE POINT R0, IN STEPS OF SIZE H,
C     FOR NPOINT STEPS.  THE POTENTIAL IS DEFINED
C     IN FUNCTION FV(), AT THE END OF INTG1.FOR.
C     CURRENTLY THE POTENTIAL FUNCTION IS IN ERGS
C     BUT THIS CAN BE CHANGED BY CHANGING THE VALUE
C     OF CON IN THE MAIN PART OF INTG1.
C     TWO POINTS ARE NEEDED TO START THE
C     INTEGRATION -- P0 AT R0, AND P1 AT R0+H
C     IT IS ASSUMED THAT P0=0., BUT YOU MUST INPUT P1.
C     THE VALUE OF P1 IS UNIMPORTANT AS LONG AS AN
C     UNDERFLOW OR AN OVERFLOW CONDITION DOES NOT
C     EXIST. FOR A SLOWLY VARYING POTENTIAL, P1 ON
C     THE ORDER OF UNITY IS APPROPRIATE, BUT FOR RAPIDLY
C     VARYING OR STEEP POTENTIALS P1 ON THE ORDER
C     OF 1.E-35 MAY BE NECESSARY.
C     THIS PROGRAM INTEGRATES THE EQUATION STARTING
C     AT THE ENERGY E0, E0 IS THEN INCREMENTED
C     BY THE AMOUNT EINC, AND THE EQUATION IS
C     INTEGRATED AGAIN.  THIS CONTINUES FOR
C     ILEVEL INTEGRATIONS.
C     CURRENTLY 512 POINTS ARE STORED IN THE
C     OUTPUT FILE. ISAVE DETERMINES THE SPACING
C     OF THESE POINTS.
C     SPACING=H*ISAVE
C
      INTEGER*4 ISTR
      DIMENSION A(6144)
      INUMS = 512          !# OF POINTS SAVED
      CON = 5.3224                 !2*M / HBAR**2 (CM / ANG**2)
C
C     ************* INPUT PARAMETERS ***************
C
      PRINT 20
20    FORMAT ('$# OF INTEGRATION POINTS (INTEGER): ')
      ACCEPT *, NPOINT
      PRINT 25
25    FORMAT ('$INTEGRATION STEP SIZE (ANG): ')
      ACCEPT *, H
      PRINT 30
30    FORMAT ('$STARTING POINT (ANGS): ')
      ACCEPT *, R0
      PRINT 35
35    FORMAT ('$STARTING PARAMETER P0: ')
      ACCEPT *, EPS
      PRINT 40
40    FORMAT ('$INITIAL ENERGY (1/CM): ')
      ACCEPT *, E0
      PRINT 45
45    FORMAT ('$ENERGY INCREMENT (1/CM): ')
      ACCEPT *, EINC
      PRINT 50
```

```
50    FORMAT ('$# OF ENERGY LEVELS (INTEGER): ')
      ACCEPT *, ILEVEL
      PRINT 55
55    FORMAT ('$OUTPUT FILE NAME ')
      CALL ASSIGN(1,DUMMY,-1)
      PRINT 60
60    FORMAT ('$FILE IDENTIFIER (4 CHAR AT MOST) = ')
      READ(5,911) ISTR
911   FORMAT(A5)
      PRINT 70
70    FORMAT ('$FRACTION OF POINTS SAVED (INTEGER): ')
      ACCEPT *, ISAVE
C
C     ********* WRITE OUTPUT FILE HEADER *************
C
      WRITE(1) ISTR                 !FILE IDENTIFIER
      WRITE(1) 1, ILEVEL
      WRITE(1) R0, H*ISAVE, INUMS
      WRITE(1) ILEVEL
      WRITE(1) E0
      WRITE(1) EINC
C
C     ************* CALCULATION *****************
C
      PRINT *,
      DO 173 II1=0,ILEVEL-1                 !ENERGY LEVEL
      E = E0 + II1 * EINC           !ENERGY ABOVE DISS.
      PRINT *, II1 + 1, E
      A(2)=EPS
      A(1)=0.
C
C         INTEGRATE SCRODINGER'S EQ.
      DO 10 I=3,NPOINT
      R = R0 + (I - 1) * H
      A(I)=(2. - H * H * CON * (E - FV(R))) * A(I-1) - A(I-2)
      IF (A(I).LT.1.E+19) GOTO 10
      DO 15 J = 1, I                        !PREVENT OVERFLOW
15    A(J) = A(J) / A(I)
10    CONTINUE
C
C         NORMALIZATION CONSTANT
      K=NPOINT
16    K=K-1
      IF (A(NPOINT)*A(K).GE. 0.) GOTO 16
      N1=K                          !LAST ZERO CROSSING
C
17    K=K-1
      IF (A(NPOINT)*A(K).LT. 0.) GOTO 17
      N=N1-K                        !PENULTIMATE ZERO CROSSING
C
      SUM=0.
      DO 11 I=0,N-1                 !INTEGRATE LAST HALF PERIOD
11    SUM=SUM+A(N1-I)
C
```

```
      FACTOR=ABS(.5079*N/SUM)
C
C         NORMALIZE
      ILOOP=1+(INUMS-1)*ISAVE
      DO 12 I=1,ILOOP,ISAVE
      A(I)=FACTOR * A(I)
      WRITE(1) A(I)
12    CONTINUE
173   CONTINUE
      CALL CLOSE(1)
C
      STOP
      END
```

```
      PROGRAM FCFACT
C
C     THIS PROGRAM CALCULATES THE FRANCK-CONDON FACTORS AND
C     R-CENTROIDS FOR TRANSITIONS BETWEEN TWO STATES WHOSE
C     VIBRATIONAL WAVEFUNCTIONS HAVE BEEN STORED ON DISK.  THE
C     MESHES ON WHICH THE WAVEFUNCTIONS HAVE BEEN CALCULATED
C     MUST BE THE SAME.  F-C FACTORS AND R-CENTROIDS ARE STORED
C     ON SEPERATE FILES AND ARE NOT SQUARED.   5/27/85   MB
C
C     FUNCTIONS:
C         SQUAD(EX)
C
C     51 LOWER VIBRATIONAL LEVELS, 100 UPPER LEVELS
C     512 POINTS / WAVEFUNCTION MAX.
C     IF FCF = 0, RCENT = -1.
C
      IMPLICIT INTEGER(V)
      VIRTUAL WFUNL(512, 51), WFUNU(512)
      VIRTUAL FCF(51, 101), RCENT(51, 101)
C         74K OF VIRTUAL MEMORY REQUIRED
      REAL INTGRD(512)
      DIMENSION IDENTL(3), IDENTU(3), IDENTF(4), IDENTR(4)
      LOGICAL*1 FCNAME(16), RNAME(16), ERR
      COMMON /SBLK/ INTGRD                  !FOR SUBROUTINE SQUAD
C
C     ********************** INPUT ***************************
C
C     ********* INPUT LOWER STATE WAVEFUNCTIONS *********
      PRINT 15
15    FORMAT ('$COMPLETE LOWER STATE FILENAME ')
      CALL ASSIGN (1, DUMMY, -1)
C
C         READ HEADER
      READ (1) (IDENTL(J), J = 1, 2)       !FILE IDENTIFIER
      IDENTL(3) = 0                  !STRING TERMINATER
      PRINT 20
20    FORMAT ('$FILE IDENTIFIER - ')
      CALL PRINT (IDENTL)
C
      READ (1) VIL, VFL   !INITIAL AND FINAL VIB. LEVELS
      READ (1) R1, STEP, NSTEP
      READ (1) IDUMMY                !EXTRA WORD
C
C         READ LOWER STATE WAVEFUNCTIONS
      DO 25 VL = VIL + 1, VFL + 1
      DO 25 J = 1, NSTEP
      READ (1) WFUNL(J, VL)
25    CONTINUE    !NEW VIBRATIONAL LEVEL
C
      CLOSE (UNIT = 1)
C
C     ********** OPEN UPPER STATE FILE *********
30    PRINT *,
      PRINT 35
```

```
35    FORMAT ('$COMPLETE UPPER STATE FILENAME ')
      CALL ASSIGN (1, DUMMY, -1)
C
C         READ HEADER
      READ (1) (IDENTU(J), J = 1, 2)                !FILE IDENTIFIER
      IDENTU(3) = 0                  !STRING TERMINATER
      PRINT 40
40    FORMAT ('$FILE IDENTIFIER - ')
      CALL PRINT (IDENTU)
C
      READ (1) VIU, VFU   !INITIAL AND FINAL VIB. LEVELS
      READ (1) R1U, STEPU, NSTEPU
      IF (ABS(R1 - R1U).GT.1.E-04) GOTO 43
      IF (ABS(STEP - STEPU).GT.1.E-06) GOTO 43
      IF (NSTEP.NE.NSTEPU) GOTO 43
      GOTO 45                !MESH PARAMETERS MUST BE IDENTICAL
43    PRINT *, 'MISMATCH IN MESH PARAMETERS - TRY A NEW FILE'
      CLOSE (UNIT = 1)
      GOTO 30
C
45    READ (1) NELEVL                !# OF CONTINUUM ENERGY LEVELS
      IF (NELEVL.LE.0) GOTO 50
      PRINT *, 'CONTINUUM FILE'
      IF (NELEVL.EQ.VFU) GOTO 46
      PRINT *, 'ERROR IN FILE HEADER'
      STOP
46    READ (1) EINIT                 !INITIAL ENERGY LEVEL (1/CM)
      READ (1) ESPACE                !ENERGY LEVEL SPACING (1/CM)
C
C     ********** OUTPUT FILENAMES **********
50    PRINT *,
      PRINT 55
55    FORMAT ('$FC FACTOR FILENAME: ')
      CALL GETSTR (5, FCNAME, 15, ERR)
      PRINT 60
60    FORMAT ('$FILE IDENTIFIER: ')
      CALL GETSTR (5, IDENTF, 6, ERR)
      PRINT 65
65    FORMAT ('$R-CENTROID FACTOR FILENAME: ')
      CALL GETSTR (5, RNAME, 15, ERR)
      PRINT 70
70    FORMAT ('$FILE IDENTIFIER: ')
      CALL GETSTR (5, IDENTR, 6, ERR)
C
C
C     ******************** CALCULATION ************************
C
      DO 110 VU = VIU + 1, VFU + 1          !UPPER VIBRATIONAL LEVEL
      PRINT 115, VU - 1
115   FORMAT (T20, ' VUPPER = ', I3)
C     FCT = 0.                !SUM OF FCF**2 FOR VL
C         READ UPPER WAVEFUNCTION
      DO 51 J = 1, NSTEP
```

```
      READ (1) WFUNU(J)
51    CONTINUE
C
      DO 120 VL = VIL + 1, VFL + 1          !LOWER VIBRATIONAL LEVEL
C
C         FORM FRANCK-CONDON INTEGRAND
      DO 125       J = 1, NSTEP
      INTGRD(J) = WFUNU(J) * WFUNL(J, VL)
125   CONTINUE
C
C         INTEGRATE FRANCK-CONDON FACTOR
      FCF(VL, VU) = SQUAD(STEP, NSTEP)
      FCT = FCT + FCF(VL, VU)**2
C
      IF (FCF(VL, VU).NE.0.) GOTO 220
      RCENT(VL, VU) = -1. !PREVENT DIVISION BY ZERO
      GOTO 120
C
C         FORM R-CENTROID INTEGRAND
220   DO 225 J = 1, NSTEP
      R = R1 + (J - 1) * STEP
      INTGRD(J) = WFUNU(J) * R * WFUNL(J, VL)
225   CONTINUE
C
C         INTEGRATE R-CENTROID
229   RCENT(VL, VU) = SQUAD(STEP, NSTEP)
      RCENT(VL, VU) = RCENT(VL, VU) / FCF(VL, VU) !NORMALIZE
C
120   CONTINUE              !NEW VL
C
      PRINT 130, FCT
130   FORMAT ('+FCT =', F8.5)
110   CONTINUE              !NEW VU
      CLOSE (UNIT = 1)
C
C     ********************** STORAGE ************************
C
C         OPEN FRANCK-CONDON FILE
300   CALL ASSIGN (1, FCNAME, 0)
      WRITE (1) (IDENTF(J), J = 1, 3)
      WRITE (1) VIL, VFL, VIU, VFU
      WRITE (1) NELEVL
C
C         OPEN R-CENTROID FILE
      CALL ASSIGN (2, RNAME, 0)
      WRITE (2) (IDENTR(J), J = 1, 3)
      WRITE (2) VIL, VFL, VIU, VFU
      WRITE (2) NELEVL
C
C         FOR CONTINUUM UPPER LEVELS
      IF (NELEVL.LE.0) GOTO 310
      WRITE (1) EINIT
      WRITE (1) ESPACE
      WRITE (2) EINIT
```

```
      WRITE (2) ESPACE
C
C         WRITE FC FACTORS AND R-CENTROIDS
310   DO 150 VL = VIL + 1, VFL + 1
      DO 150 VU = VIU + 1, VFU + 1
      WRITE (1) FCF(VL, VU)
      WRITE (2) RCENT(VL, VU)
150   CONTINUE
C
      CLOSE (UNIT = 1)
      CLOSE (UNIT = 2)
C
C     ************************************************************
C
C     GOTO 30                          !NEW UPPER STATE
      STOP
      END
```

```
      PROGRAM VIBDIS
C
C     VIBDIS CALCULATES THE DISTRIBUTION OF VIBRATIONAL LEVELS
C     OBSERVED AT A GIVEN WAVELENGTH.  THE FRANCK-CONDON FACTORS
C     FOR THE TRANSITON MUST ALREADY BE STORED ON DISK.  THE
C     RELATIVE CONTRIBUTION OF EACH (MORSE) VIBRATIONAL LEVEL
C     IS BOTH PRINTED AND STORED ON DISK.  MB
C     MODIFIED FOR USE WITH CONTINUUM STATES. 6/1/85 MB
C     TO USE A NEW UPPER STATE, CHANGE THE UPPER STATE PARAMETERS,
C     INSERT A FUNCTION TO CALCULATE THE UPPER STATE ENERGY,
C     AND CHANGE ENU IN CALCULATION-DISCRETE STATES SO IT IS THE
C     UPPER STATE ENERGY.  NOTE DEFINITION OF EINIT FOR 1U STATE.
C
C     FUNCTIONS - MUST MATCH STATES INVOLVED
C         ENX     ENB     ENA     N       SQUAD(EX)
C
      IMPLICIT INTEGER(V)
      REAL M, INTGRD(512)
      INTEGER FNAME(4)
      VIRTUAL FCF(51, 101), RCENT(51, 101)
      DIMENSION TRANST(51), IDENTF(4), IDENTR(4), NAME(8)
      COMMON /SBLK/ INTGRD
C
C         UPPER STATE PARAMETERS (1U-STATE)
      TEU = 12546.                  !UPPER STATE TE (1/CM)
      DISSU = -180.         !UPPER STATE DISSOCIATION ENERGY (1/CM)
      TRMMOM = 0.136 * 2. !TRANSITION MOMENT (DEBYE**2) * DEGENERACY
C
C     ********************** INPUT ***************************
C
C         OPEN FRANCK-CONDON FILE
      PRINT 15
15    FORMAT ('$COMPLETE NAME OF FILE CONTAINING F-C
     1 FACTORS ')
      CALL ASSIGN (1, DUMMY, -1)
C
      READ (1) (IDENTF(J), J = 1, 3)
      IDENTF(4) = 0                 !FILE TERMINATER
      PRINT 22
22    FORMAT ('$FC IDENTIFIER - ')
      CALL PRINT (IDENTF)
C
      READ (1) VIL, VFL, VIU, VFU
      READ (1) NELEVL
C
C         OPEN R-CENTROID FILE
      PRINT 17
17    FORMAT ('$COMPLETE NAME OF FILE CONTAINING R-CENTROIDS')
      CALL ASSIGN (3, DUMMY, -1)
      READ (3) (IDENTR(J), J = 1, 3)
      IDENTR(4) = 0                 !FILE TERMINATER
      PRINT 24
24    FORMAT ('$R-CENTROID IDENTIFIER - ')
      CALL PRINT (IDENTR)
```

```
C
      READ (3) VILR, VFLR, VIUR, VFUR
      READ (3) NELEVR
C
C         TEST FILE AGEEMENT
      IF (VIL.NE.VILR.OR.VFL.NE.VFLR.OR.VIU.NE.VIUR.OR.
     1VFU.NE.VFUR.OR.NELEVL.NE.NELEVR) GOTO 35
      GOTO 36
35    PRINT *, 'MIS-MATCHED FILES'
      STOP
C
C         CONTINUUM FILES
36    IF (NELEVL.LE.0) GOTO 25
      READ (1) EINIT
      READ (1) ESPACE
      READ (3) EINITR
      READ (3) ESPACR
      IF ((EINIT - EINITR).GT.1.E-04) GOTO 35
      IF ((ESPACE - ESPACR).GT.1.E-04) GOTO 35
      EINIT = EINIT + 180.                    !1U STATE ONLY!
C
C         READ FRANCK-CONDON FACTORS AND R-CENTROIDS
25    DO 30 VL = VIL + 1, VFL + 1
      DO 30 VU = VIU + 1, VFU + 1
      READ (1) FCF(VL, VU)
      READ (3) RCENT(VL, VU)
30    CONTINUE
      CLOSE (UNIT = 1)
C
C         TRANSITION WAVELENGTH
      PRINT *,
10    PRINT 5
5     FORMAT ('@TRANSITION WAVELENGTH (NM): ')
      ACCEPT *, WTRANS
      ETRANS = 1.0E7 / WTRANS                 !TRANSITION ENERGY (1/CM)
C
C         OPEN OUTPUT FILE
      PRINT 20
20    FORMAT ('@COMPLETE OUTPUT FILENAME: ')
      CALL GETSTR (5, NAME, 14)
      CALL ASSIGN (2, NAME, 0)
      PRINT 45
45    FORMAT ('@FILE IDENTIFIER - ')
      CALL GETSTR(5, FNAME, 7)
C
C     ********************** CALCULATION ********************
C
C         INITIALIZE TRANST
      DO 110 J = 1, 51
110   TRANST(J) = 0.
C
C         DISCRETE STATES
      IF (NELEVL.GT.0) GOTO 150   !CONTINUUM STATES
      DO 120 VL = VIL, VFL
```

```
      DO 120 VU = VIU, VFU
      ENU = ENA(VU)                                   !UPPER ENERGY
      DELTAE = ENU - ENX(VL) - ETRANS                 !ENERGY MISMATCH
C     TRNMOM = AM2(RCENT(VL + 1, VU + 1)) !TRANSITION MOMENT
      WT = W(DELTAE)                                  !WEIGHTING FUNCTION
C
      TRANST(VL + 1) = TRANST(VL + 1) +
     1 WT * FCF(VL + 1, VU + 1)**2 * TRNMOM
C
120   CONTINUE
      GOTO 200              !OUTPUT
C
C         CONTINUUM STATES
150   DO 155 VL = VIL, VFL
      DO 160 JE = 1, NELEVL
      E = EINIT + (JE - 1) * ESPACE          !ENERGY (1/CM) ABOVE DISS.
      ENU = TEU + DISSU + E                           !ENERGY ABOVE VX=0
      DELTAE = ENU - ENX(VL) - ETRANS                 !ENERGY MISMATCH
C     TRNMOM = AM2(RCENT(VL + 1, JE + 1)) !TRANSITION MOMENT
      D = 1.1536 / SQRT(E)                            !DENSITY OF STATES
      WT = W(DELTAE)                                  !WEIGHTING FUNCTION
C
      INTGRD(JE + 1) = FCF(VL + 1, JE + 1)**2 * WT *
     1 TRNMOM * D
C
160   CONTINUE                               !NEW JE
C
      INTGRD(1) = INTGRD(2)                  !INTEGRATE TO E = 0
      TRANST(VL + 1) = SQUAD(ESPACE, NELEVL + 1)
155   CONTINUE                               !NEW VL
C
C     ************************ OUTPUT ************************
C
C         WRITE HEADER
200   WRITE (2) (FNAME(J), J = 1, 3)         !FILE IDENTIFIER
      WRITE (2) VIL, VFL
      WRITE (2) WTRANS
      WRITE (2) 0                    !EXTRA WORD
C
C         WRITE TRANSITION STRENGTHS TO DISK
      DO 210 VL = VIL + 1, VFL + 1
210   WRITE (2) TRANST(VL)
      CLOSE (UNIT = 2)
C
C         PRINT RESULTS
      PRINT *, '!LPR C'              !PRINTER ON
      PRINT 212
212   FORMAT ('$FILENAME - ')
      CALL PRINT (NAME)
      PRINT 213, WTRANS
213   FORMAT (' TRANSITION AT ', F5.0, ' NM', /)
      PRINT 215
215   FORMAT ('  VL   ENERGY   STRENGTH', /)
C
```

```
      TSUM = 0.
      DO 220 VL = VIL, VFL
      PRINT 217, VL, EMX(VL), TRANST(VL + 1)
217   FORMAT ('  ', I2, X, F8.1, X, G12.5)
      TSUM = TSUM + TRANST(VL + 1)
220   CONTINUE
C
      PRINT 225, TSUM
225   FORMAT (/, ' TOTAL =', 6X, G12.5)
      PRINT *, '!LPR N'                          !PRINTER OFF
      PAUSE 'RETURN FOR NEW WAVELENGTH'
      GOTO 10
C
      STOP
      END
```

```
      PROGRAM TRANAD
C
C     THIS PROGRAM ADDS TRANSITION STRENGTH FILES. 6/1/85 MB
C
      IMPLICIT INTEGER (V)
      INTEGER FNAME(8)
      DIMENSION IDENT(4), TRANS(51)
C
      DO 5 J = 1, 51
5     TRANS(J) = 0.
C
C     ****************** READ AND ADD OLD FILES **************
C
10    PRINT 15
15    FORMAT ('$COMPLETE FILENAME ')
      CALL ASSIGN (1, DUMMY, -1)
C
C         READ HEADER
      READ (1) (IDENT(J), J = 1,3)
      IDENT(4) = 0.                 !STRING TERMINATER
      PRINT 20
20    FORMAT ('$FILE IDENTIFIER - ')
      CALL PRINT (IDENT)
C
      READ (1) VI, VF
      READ (1) WTRANS
      READ (1) IDUMMY
C
C         READ AND ADD TRANSITION STRENGTHS
      DO 25 V = VI + 1, VF + 1
      READ (1) T
      TRANS(V) = TRANS(V) + T
25    CONTINUE
C
      CLOSE (UNIT = 1)
C
C         REPEAT?
      ANS = 'N'             !DEFAULT = STOP
      PRINT 30
30    FORMAT ('$ADD ANOTHER FILE?')
      ACCEPT 35, ANS
35    FORMAT (1A)
      IF (ANS.EQ.'Y') GOTO 10
C
C     ************************ WRITE NEW FILE ********************
C
      PRINT *,
      PRINT 110
110   FORMAT ('$SUM FILE NAME: ')
      CALL GETSTR(5, FNAME, 15)
      PRINT 115
115   FORMAT ('$SUM FILE IDENTIFIER - ')
      CALL GETSTR(5, IDENT, 6)
      CALL ASSIGN(1, FNAME, 0)
```

```
C
C          WRITE HEADER
      WRITE (1) (IDENT(J), J = 1, 3)
      WRITE (1) VI, VF
      WRITE (1) WTRANS              !TRANSISION WAVELENGTH
      WRITE (1) 0.                          !EXTRA WORD
C
C          WRITE TRANSITION STRENGTHS
      DO 120 V = VI + 1, VF + 1
      WRITE (1) TRANS(V)
120   CONTINUE
C
      CLOSE (UNIT = 1)
C
C     ******************** PRINT RESULTS ********************
C
      PRINT 213, WTRANS
213   FORMAT (' TRANSITION AT ', F5.0, ' NM', /)
      PRINT 215
215   FORMAT ('  VL    ENERGY    STRENGTH', /)
C
      TSUM = 0.
      DO 220 V = VI, VF
      PRINT 217, V, EMX(V), TRANS(V + 1)
217   FORMAT ('  ', I2, X, F8.1, X, G12.5)
      TSUM = TSUM + TRANS(V + 1)
220   CONTINUE
C
      PRINT 225, TSUM
225   FORMAT (/, ' TOTAL =', 6X, G12.5)
      STOP
      END
```

Appendix C. Vibrational Population Distribution Calculation

The data inversion to find the population distribution requires several provisions to obtain reasonable results. First, to get the total absorption at a given wavelength, the absorption of the ground state at that wavelength must be added to the absorption change measured by the data. Thus one number must be chosen which represents the total population relaxing in the X state, but which is the same for all wavelengths and all times. The total population should be such that the total absorption at 500 nm is near the maximum bleach observed. Furthermore, none of the populations calculated should be negative, nor should the lowest level populate before the higher levels. These conditions restrict the value of the population to a narrow range. Variation of the population within this range causes small variations in the population in the lowest energy region and negligible changes elsewhere.

For the data obtained using a 12-ps A-state risetime, all the conditions on the population value cannot be simultaneously satisfied. This arises because the subtracted bleach curve has a nearly flat early portion, whereas a partial early recovery is expected (see text). If a risetime of 17 ps is used, a qualitatively correct bleach curve is obtained and a realistic population distribution is found. A risetime of 17 ps was used for all the data used to generate figure 19. It is not surprising that this is a different risetime than that cited earlier. Since the exponential rise assumed for the A state is probably not the correct functional form, slightly different exponential risetimes will give the best results in different situations.

Finally, the function S' must be chosen to give the proper limit at long times. For most of the energy regions, S' is set equal to the average value of S over that region. For the lowest region, however, the value is set to the value at the bottom of the well. This insures that at long times, when the population is all at the very bottom of the well, the correct absorption spectrum will be predicted.

The FORTRAN code for the program DATINV, which actually performed the calculation, follows.

```
      PROGRAM DATINV
C
C     THIS PROGRAM IS INTENDED TO APPROXIMATE THE I2 VIBRATIONAL
C     DISTRIBUTIONS AT SEVERAL TIMES.  THE CORRELATION FUNCTION
C     OF THE FRANCK-CONDON STRENGTH WITH THE VIBRATIONAL DISTRIBUTION
C     IS INVERTED BY APPROXIMATING IT AS A MATRIX PROBLEM.  5/20/85
C
C     FUNCTIONS:
C         MINV(EX)        EXX     IRND
C
C
      LOGICAL*1 NAME(16), ERR
      IMPLICIT INTEGER (V)
      INTEGER TPT(20), VPT(7), DPTS, STEPS, TO
      DIMENSION DATA(6,20), TRANST(6,6), P(6, 20), WTRANS(6)
      DIMENSION IDENT(3), W1(6), W2(6), DATA1(6,20), TRANS(6,6)
C
C     ************ READ EXTERNAL COMMAND FILE *************
C
      PRINT 15
15    FORMAT ('$INPUT COMMAND FILE NAME ')
      CALL ASSIGN (2, DUMMY, -1)
      PRINT *, '!LPR C'              !PRINTER ON
      READ (2, *) MICRON             !MICRONS/STEP
      PRINT *, MICRON, 'MICRONS / STEP'
      READ (2, *) IWIDTH             !DATA AVERAGING HALF WIDTH (PTS)
      PRINT *, 'AVERAGE +-', IWIDTH, ' POINTS OF DATA'
      READ (2, *) NDIM               !# LAMBDA PTS = # ENERGY PTS
      READ (2, *) (VPT(J), J = 2, NDIM)  !VIB. DIVIDING PTS.
      PRINT *, 'VIBRATIONAL DIVIDING POINTS'
      PRINT *, (VPT(J), J = 2, NDIM)
      READ (2, *) NTPTS              !# TIME PTS
      READ (2, *) (TPT(J), J = 1, NTPTS)  !TIME PTS
C
C     ******** READ AND AVERAGE TRANSITION STRENGTHS *******
C
      PRINT *,
      PRINT *, 'TRANSITION STRENGTH FILES'
      PRINT *,
      DO 210 LAMBDA = 1, NDIM
C
C         OPEN FILE AND READ HEADER
      CALL GETSTR (2, NAME, 15, ERR)
      CALL ASSIGN (1, NAME, 0)
      CALL PRINT(NAME)
      READ (1) (IDENT(J), J = 1, 3)        !FILE IDENTIFIER
      READ (1) VIX, VFX              !INITIAL AND FINAL VIB.
      VPT(1) = VIX
      VPT(NDIM + 1) = VFX
      READ (1) WTRANS(LAMBDA)                !TRANSITION WAVELENGTH (NM)
      READ (1) IDUMMY                        !EXTRA WORD
C
C         IDENTIFY BLEACH DATA
      IF (WTRANS(LAMBDA).GT.550.) GOTO 215
```

```
      LGREEN = LAMBDA
C
C         TRAPAZOID RULE INTEGRATION OF TRANSITION STRENGTHS
215   READ (1) ENDPT                          !FIRST TRANSITION STRENGTH
      ENDPT1 = ENDPT
C
      DO 220 JE = 1, NDIM          !VIB ENERGY REGION
      SUM = 0.5 * ENDPT
      NINTER = VPT(JE + 1) - VPT(JE)       !# OF INTERVALS IN INTEGRATION
C
      DO 230 VX = VPT(JE) + 1, VPT(JE + 1) - 1
      READ (1) TRAN
      SUM = SUM + TRAN
230   CONTINUE
C
      READ (1) ENDPT
      SUM = SUM + 0.5 * ENDPT
      TRANST(LAMBDA, JE) = SUM / NINTER
C         CHANGE JE = 1 DEFINITION
      IF (JE.EQ.1) TRANST(LAMBDA, JE) = ENDPT1
C
220   CONTINUE              !NEW ENERGY REGION
C
      CLOSE (UNIT = 1)
210   CONTINUE              !NEW WAVELENGTH
C
C         DELTA FUNCTION APPROXIMATION
C     DO 232 LAMBDA = 1, NDIM
C     DO 232 JE = 1, NDIM
C     IF (JE.NE.LAMBDA) TRANST(LAMBDA, JE) = 0.
C     IF (JE.EQ.LAMBDA) TRANST(LAMBDA, JE) = 0.2E-03
C232  CONTINUE
C
C         RESCALE TRANSITION STRENGTHS
      DO 250 LAMBDA = 1, NDIM
      DO 250 JE = 1, NDIM
      TRANST(LAMBDA, JE) = TRANST(LAMBDA, JE) * 5.0E+03
250   CONTINUE
C
C     ***************** READ SUBTRACTED DATA ******************
C
      PRINT *,
      PRINT *, 'DATA FILES'
      LDUMMY = 0.
      DO 120 LAMBDA = 1, NDIM              !WAVELENGTH (FILE)
      READ (2, *) SMAX              !MAXIMUM SIGNAL CHANGE
C
C         OPEN DATA FILE
      CALL GETSTR(2, NAME, 15, ERR)        !READ FILENAME FROM COMMAND FILE
      ITEST = ISCOMP('DUMMY', NAME)
      IF (ITEST.NE.0) GOTO 103
      LDUMMY = LAMBDA
      GOTO 120
103   CALL ASSIGN(1, NAME, 0)
```

```
      PRINT 105, NAME, NTRANS(LAMBDA), SMAX
105   FORMAT (' ', 16A1, F7.0, ' NM ', F7.3, ' SIGNAL CHANGE')
      DEFINE FILE 1 (1000, 1, U, IASV)
      READ (1'1) KB                          !FILE TYPE IDENTIFIER
      IF (KB.EQ."45502) GOTO 110
      PRINT *, 'WRONG FILE TYPE'
      STOP
C
C         READ PARAMETER FROM DATA FILE
110   READ (1'13) DPTS              !# OF DATA PTS
      READ (1'18) STEPS             !STEPS / PT
C     EARLY FILES HAD T0 AT 77 - NOW CR IS AT 77, T0 AT 80
      READ (1'77) T0
      IF (T0.EQ.13) READ (1'80) T0          !T=0 PT
      PSPT = MICRON * STEPS / 299.79        !PICOSECONDS / PT
C
C     *******      READ AND AVERAGE DATA *******
      DO 130 JT = 1, NTPTS                  !TIME PT
      LOCTPT = IRND(TPT(JT) / PSPT) + T0    !TPT LOCATION IN POINTS
      IF (LOCTPT + IWIDTH.LE.DPTS) GOTO 132
      IF (LOCTPT.GT.DPTS) GOTO 135
      PRINT *, 'ERROR IN TIME LOCATION - ', TPT(JT), 'PS'
      PAUSE 'RETURN TO SET DATA = 0'
135   DATA1(LAMBDA, JT) = 0.
      GOTO 130
C
C         AVERAGING LOOP
132   SUM = 0.
      DO 140 K = LOCTPT - IWIDTH, LOCTPT + IWIDTH
      READ (1' K + 256) INTER
      DIFF = (FLOAT(INTER) / 100.) - 10.  !DE-SCALE DIFF DATA
      IF (DIFF.LT.-.002) DIFF = DIFFT              !SET TO PREVIOUS VALUE
      DIFFT = DIFF
      SUM = SUM + DIFF
140   CONTINUE
C
      SUM = SUM * SMAX / 100.               !SCALE TO ABS. CHANGE
      DATA1(LAMBDA, JT) = SUM / (2 * IWIDTH + 1)
130   CONTINUE
C
C         RE-INVERT BLEACH DATA
      IF (LAMBDA.NE.LGREEN) GOTO 129
      DO 127 JT = 1, NTPTS
127   DATA1(LAMBDA, JT) = -DATA1(LAMBDA, JT)
C
129   CLOSE (UNIT = 1)              !CLOSE DATA FILE
120   CONTINUE                      !NEW WAVELENGTH
C
C         JUGGLE TRANSITION MATRIX SO TOTAL POP. IS FIXED
      DO 165 LAMBDA = 1, NDIM
      DO 165 JE = 1, NDIM
165   TRANS(LAMBDA, JE) = TRANST(LAMBDA, JE)  !PRESERVE ORIGINAL VALUES
      IF (LDUMMY.EQ.0) GOTO 170
      DO 128 JE = 1, NDIM
```

```
128   TRANS(LDUMMY, JE) = 1.
C
C         PRINT TRANST MATRIX
170   PRINT *,
      PRINT *,
      PRINT *,'TRANSITION STRENGTHS * 5.E+03'
      DO 155 LAMBDA = 1, NDIM
      PRINT 160, NTRANS(LAMBDA), (TRANS(LAMBDA, JE),
     1 JE = 1, NDIM)
160   FORMAT(F6.0, ':', 6(2X, G11.4))
155   CONTINUE
      PRINT *,
      PRINT *,
C
C     ******************** INVERT TRANST ******************
C     ASSUMING DATA = TRANST * P (MATRIX MUL.) WHERE P IS THE VECTOR
C     DESCRIBING THE VIBRATIONAL DISTRIBUTION, P CAN BE FOUND BY
C     INVERTING THE TRANST MATRIX
C
      CALL MINV(TRANS, NDIM, DET, W1, W2)
C
C         PRINT INVERSE TRANST MATRIX
      PRINT *,
      PRINT *,
      PRINT *, 'DETERMINANT =', DET
      PRINT *,
      PRINT *,
      PRINT *,'INVERSE TRANSITION STRENGTHS'
      DO 340 LAMBDA = 1, NDIM
      PRINT 345, (TRANS(LAMBDA, JE), JE = 1, NDIM)
345   FORMAT(6X, ':', 6(2X, G11.4))
340   CONTINUE
      PRINT *,
      PRINT *,
C
C     ********** REDEFINE DATA BASELINE ******************
C
600   PRINT *,
      PRINT 605
605   FORMAT ('$A0 = ')
      ACCEPT *, A0
C
C         CORRECT BASELINE
      DO 625 LAMBDA = 1, NDIM
      DO 625 JT = 1, NTPTS
      DATA(LAMBDA, JT) = DATA1(LAMBDA, JT) + A0 *
     1 TRANST(LAMBDA, 1) / TRANST(LGREEN, 1)
625   CONTINUE
C
C         ASSIGN "DUMMY" DATA
      IF (LDUMMY.EQ.0) GOTO 630
      POPTOT = A0 / TRANST(LGREEN, 1)
      PRINT *, 'POPTOT = ', POPTOT          !TOTAL POPULATION
      DO 610 JT = 1, NTPTS
```

```
      DATA(LDUMMY, JT) = POPTOT
610   CONTINUE
C
C
C         PRINT DATA MATRIX
630   PRINT *,
      PRINT *, 'DATA(%)'
      DO 615 JT = 1, NTPTS
      PRINT 620, TPT(JT), (DATA(LAMBDA, JT) * 100.,
     1 LAMBDA = 1, NDIM)
620   FORMAT (' ', I4, ':', 6(2X, F10.4))
615   CONTINUE
C
C     ******************** CALCULATE P ********************
C
      DO 410 IT = 1, NTPTS                    !TIME
      DO 410 I = 1, NDIM
      P(I, IT) = 0.
      DO 410 J = 1, NDIM
      P(I, IT) = P(I, IT) + TRANS(I, J) * DATA(J, IT)
410   CONTINUE
C
C     ********************** PRINT P ************************
C
      DO 510 IT = 1, NTPTS                    !TIME POINT
C
C         PRINT HEADING
      PRINT 515, TPT(IT)
515   FORMAT (/, 10X, 'TIME = ', I3, ' PS', /)
      PRINT 520
520   FORMAT ('  VIB', 5X, 'AVE', 27X, 'P DEN')
      PRINT 525
525   FORMAT (' LEVELS  ENERGY', 8X, 'P', 8X, 'P(%)', 2X,
     1 '1/1000 CM')
C
C         SUM P
      PTOT = 0.
      DO 530 JE = 1, NDIM
530   PTOT = PTOT + P(JE, IT)
C
C         PRINT P
      DO 535 JE = 1, NDIM          !ENERGY REGIONS
      PPER = P(JE, IT) * 100. / PTOT       !P AS A % OF TOTAL
      ENIDTH = (ENX(VPT(JE + 1)) - ENX(VPT(JE))) / 2.      !ENERGY WIDTH
      PDEN = (PPER / ENIDTH) * 1000.       !POPULATION DENSITY
      EAVE = (ENX(VPT(JE + 1)) + ENX(VPT(JE))) / 2.   !AVE. ENERGY
      PRINT 540, VPT(JE), VPT(JE + 1), EAVE, P(JE, IT), PPER,
     1 PDEN
540   FORMAT (' ', I2, '-', I2, 3X, F5.0, 3X, E11.4, 2X,
     1 F6.2, 3X, F7.2)
535   CONTINUE              !NEW ENERGY REGION
C
      PRINT 545, PTOT
545   FORMAT (11X, 'TOTAL ', E11.4)
```

```
C
C          CALCULATE AND PRINT DUMMY SIGNAL
      IF (LDUMMY.EQ.0) GOTO 510
      DUMSIG = 0.
      DO 550 JE = 1, NDIM
550   DUMSIG = DUMSIG + P(JE, IT) * TRANST(LDUMMY, JE)
      PRINT *, 'DUMMY SIGNAL =', DUMSIG
C
510   CONTINUE              !NEW TIME POINT
C
      GOTO 600
      STOP
      END
```

References

1. Geminate recombination refers to the recombination of a dissociating atom with its original partner to form a bound, molecular species.
2. E. Rabinowitch and W. C. Wood, Trans. Faraday Soc. 32, 547 (1936).
3. T. J. Chuang, G. W. Hoffman and K. B. Eisenthal, Chem. Phys. Lett. 25, 201 (1974).
4. D. J. Nesbitt and J. T. Hynes, J. Chem. Phys. 77, 2130 (1982).
5. D. F. Kelley, N. A. Abul-Haj, D.-J. Jang, J. Chem. Phys. 80, 4105 (1984).
6. D. F. Kelley and N. A. Abul-Haj, in Ultrafast Phenomena IV, edited by D. H. Auston and K. B. Eisenthal, Springer Ser. Chem. Phys. 38 (Springer, New York, 1984), p. 292.
7. N. A. Abul-Haj and D. F. Kelley, Proc. Soc. Photo-Optical Instrum. Engin. (in press).
8. P. Bado, C. Dupuy, D. Magde, K. R. Wilson, and M. M. Malley, J. Chem. Phys. 80, 5531 (1984).
9. P. Bado and K. R. Wilson, J. Phys. Chem. 88, 655 (1984).
10. P. Bado, P. H. Berens, J. P. Bergsma, S. B. Wilson, K. R. Wilson, and E.J. Heller, in Picosecond Phenomena III, edited by K. B. Eisenthal, R. M. Hochstrasser, W. Kaiser, A. Laubereau, Springer Ser. Chem. Phys. 23 (Springer, New York, 1982), p. 260.
11. P. Bado, C. G. Dupuy, J. P. Bergsma, and K. R. Wilson, in Ultrafast Phenomena IV, edited by D. H. Auston and K. B. Eisenthal, Springer Ser. Chem. Phys. 38 (Springer, New York, 1984), p. 296.
12. M. Berg, A. L. Harris, and C. B. Harris, Phys. Rev. Lett. 54, 951

(1985).

13. M. Berg, A. L. Harris, J. K. Brown, and C. B. Harris, in Ultrafast Phenomena IV, edited by D. H. Auston and K. B. Eisenthal, Springer Ser. Chem. Phys. 38 (Springer, New York, 1984), p. 300.

14. J. Zimmerman and R. M. Noyes, J. Chem. Phys. 18, 658 (1950).

15. F. W. Lampe and R. M. Noyes, J. Am. Chem. Soc. 76, 2140 (1954).

16. D. Booth and R. M. Noyes, J. Am. Chem. Soc. 82, 1868 (1960).

17. L. F. Meadows and R. M. Noyes, J. Am. Chem. Soc. 82, 1872 (1960).

18. R. M. Noyes, Z. Electrochem. 64, 153 (1960).

19. R M. Noyes, Prog. React. Kinetics 1, 129 (1961).

20. K. Luther and J. Troe, Chem. Phys. Lett. 24, 85 (1974).

21. K. Luther, J. Schroeder, J. Troe, and U. Unterberg, J. Phys. Chem. 84, 3072 (1980).

22. B. Otto, J. Schroeder and J. Troe, J. Chem. Phys. 81, 202 (1984).

23. H. Hippler, V. Schubert, and J. Troe, J. Chem. Phys. 81, 3931 (1984).

24. J. Tellinghuisen, J. Chem. Phys. 82, 4012 (1985).

25. Ref. 3 reported time parameters from a free flight model, Refs. 8 and 9 characterized times by the FWHM of the decay curves, and Ref. 13 used exponential fits to the decaying edge of the absorption.

26. C. A. Langhoff, B. Moore and M. DeMeuse, J. Am. Chem. Soc. 104, 3576 (1982).

27. C. A. Langhoff, B. Moore, and M. DeMeuse, J. Chem. Phys. 78, 1191 (1983).

28. D. F. Kelley and P. M. Rentzepis, Chem. Phys. Lett. 85, 85 (1982).

29. C. L. Brooks, III, M. W. Balk, and S. A. Adelman, J. Chem. Phys. 79, 784 (1983).

30. P. Bado, P. H. Berens, and K. R. Wilson, in Picosecond Lasers and Applications, edited by L. S. Goldberg, Proc. Soc. Photo-Optical Instrum. Engin. 322, p. 230 (1982).

31. P. Bado, P. H. Berens, J. P. Bergsma, M. H. Coladonato, C. G. Dupuy, P. M. Edelsten, J. D. Kahn, K. R. Wilson, and D. R. Fredkin, in Photochemistry and Photobiology: Proceedings of the International Conference, A. H. Zewail, ed. (Harwood, New York, 1983).

32. J. Tellinghuisen, J. Chem. Phys. 76, 4736 (1982).

33. J. Tellinghuisen, J. Quant. Spectrosc. Radiat. Transfer 19, 149 (1978).

34. M. Berg, A. L. Harris, J. K. Brown, and C. B. Harris, Opt. Lett. 9, 50 (1984).

35. For a review see M. Tamres and R. L. Strong, in Molecular Association, edited by R. Foster, (Academic Press, New York, 1979) Vol. 2, Chap. 5.

36. L. E. Orgel and R. S. Mulliken, J. Am. Chem. Soc. 79, 4839 (1957).

37. D. F. Evans, J. Chem. Phys. 23, 1424 (1955).

38. H. A. Benesi and J. H. Hildebrand, J. Am. Chem. Soc. 71, 2703 (1949).

39. S. R. Logan, R. Bonneau, J. Joussot-Dubien, and P. Fournier de Violet, J. Chem. Soc., Faraday I 71, 2148 (1975).

40. Atom/solvent contact charge-transfer absorptions are observed in the UV (Sec. IIIA). No evidence correlating absorption strengths from molecular states with the solvent's ionization potential was observed, indicating that molecule/solvent contact charge-transfer transitions are not important in these measurements.

41. The CH_2Cl_2 used contained an alkene preservative which caused some UV absorption. Since the results in CH_2Cl_2 solutions are very similiar to results in $CHCl_3$ and CCl_4, there appears to be no affect on the dynamics.

42. P. A. D. de Maine, J. Chem. Phys. 24, 1091 (1956).

43. R. Marshall and N. Davidson, J. Chem. Phys. 21, 2086 (1953).

44. R. S. Mulliken, J. Chem. Phys. 55, 288 (1971).

45. K. S. Viswanathan, A. Sur, and J. Tellinghuisen, J. Mol. Spectrosc. 86, 393 (1981).

46. J. Tellinghuisen, J. Mol. Spectrosc. 94, 231 (1982).

47. P. B. Beeken, E. A. Hanson, and G. W. Flynn, J. Chem. Phys. 78, 5892 (1983).

48. The absorption strength at 295 nm is uncertain because of a different experimental configuration at that wavelength. The absorption coefficient was obtained by scaling the absorption strength at each wavelength to the magnitude of the A'-state bleach component at 500 nm. It was assumed that $\varepsilon_{500}(A') = 0$ and $\varepsilon_{500}(X) = 800\ L\text{-}mol^{-1}\text{-}cm^{-1}$.

49. J. Tellinghuisen, A. R. Whyte, and L. F. Phillips, J. Phys. Chem. 88, 6084 (1984).

50. L. M. Julien and W. B. Person, J. Phys. Chem. 72, 3059 (1968).

51. J. P. Perrot, M. Broyer, J. Chevaleyre, and B. Femelat, J. Mol. Spectrosc. 98, 161 (1983).

52. K. S. Viswanathan and J. Tellinghuisen, J. Mol. Spectrosc. 101, 285 (1983).

53. G. T. Evans and M. Pinman, J. Phys. Chem. 80, 1344 (1976).

54. B. Martire and R. G. Gilbert, Chem. Phys. 56, 241 (1981).

55. D. R. Bauer, J. I. Brauman, and R. Pecora, J. Am. Chem. Soc. 96, 6840 (1974).

56. F. D. Rossini, K. S. Pitzer, R. L. Arnett, R. M. Brown, and G. C. Pimentel, Selected Values of Physical and Thermodynamic Properties of Hydrocarbons and Related Compounds, American Petroleum Institute Project 44 (Carnegie Press, Pittsburgh, 1953) Tables 20c, 23c; J. A. Dean, ed., Lange's Handbook of Chemistry, 12th ed., (McGraw-Hill, New York, 1979), Table 10-35.

57. J. T. Hynes, R. Kapral, and G. M. Torrie, J. Chem. Phys. 72, 177 (1980).

58. M. Schell and R. Kapral, Chem. Phys. Lett. 81, 83 (1981).

59. K. J. Shin and R. Kapral, J. Chem. Phys. 69, 3685 (1978).

60. M. W. Balk, C. L. Brooks, III, and S. A. Adelman, J. Chem. Phys. 79, 804 (1983).

61. C. L. Brooks, III and S. A. Adelman, J. Chem. Phys. 80, 5598 (1984).

62. J. M. Dawes and M. G. Sceats, Chem. Phys. 96, 315 (1985).

63. D. L. Bunker and B. S. Jacobsen, J. Am. Chem. Soc. 94, 1843 (1972).

64. J. N. Murrell, A. J. Stace and R. Dammell, J. Chem. Soc. Faraday Trans. 2 74, 1532 (1978).

65. A. H. Lipkus, F. P. Buff and M. G. Sceats, J. Chem. Phys. 79, 4830 (1983).

66. J. M. Deutch and I. Oppenheim, J. Chem. Phys. 54, 3547 (1971); J. Albers, J. M. Deutch, and I. Oppenheim, J. Chem. Phys. 54, 3541 (1971); P. Mazur and I. Oppenheim, Physica 50, 241 (1970).

67. D. P. Ali and W. H. Miller, J. Chem. Phys. 78, 6640 (1983); D. P. Ali and W. H. Miller, Chem. Phys. Lett. 105, 501 (1984).

68. T. Shimanouchi, Tables of Molecular Vibrational Frequencies, Consolidated Volume I, Nat. Stand. Ref. Data Ser., Nat. Bur. Stand. (U.S.), 39 (U. S. Government Printing Office, Washington, D. C., 1972).

69. R. J. LeRoy, J. Chem. Phys. 52, 2683 (1970).

70. The resonant transfer width is taken to be $\hbar\alpha\,(kT/\mu)^{1/2}/2$, where α is the range of the exponential interaction potential and μ is the reduced mass of the collision. Eq. 5.4 of Ref. 4, which was used to calculate the V-V energy transfer rates, should read:

$$\Delta E^{VV}(v\to v-1) = -\left(\frac{2}{\pi}\right)^{1/2}\hbar\,\omega_{I_2}\,v\,\left(\frac{2\mu|U_{if}|}{\hbar\alpha}\right)^2\left(\frac{\mu}{kT}\right)^{3/2} e^{\Delta E/2kT}$$
$$\times\int_0^\infty dv_0\, v_0^4 \exp\left(\frac{-\mu v_0^2}{2kT}\right)\operatorname{sech}^2\left(\frac{2\Delta E}{\hbar v_0\alpha}\right)$$

71. C. B. Moore, J. Chem. Phys. 43, 2979 (1965).

72. R. J. Myers and W. D. Gwinn, J. Chem. Phys. 20, 1420 (1952).

73. S. N. Ghosh, R. Trambarulo, and W. Gordy, J. Chem. Phys. 20, 605 (1952).

74. D. J. Nesbitt and J. T. Hynes, J. Chem. Phys. 76, 6002 (1982).

75. J. B. Koffend, R. Bacis, and R. W. Field, J. Chem. Phys. 70, 2366 (1979).

76. J. I. Steinfeld, J. Chem. Phys. 44, 2740 (1966).

77. G. A. Capelle and H. P. Broida, J. Chem. Phys. 58, 4212 (1973).

78. J. I. Steinfeld, J. Phys. Chem. Ref. Data 13, 445 (1984).

79. R. F. Barrow and K. Y. Yee, J. Chem. Soc., Faraday II 69, 684 (1973).

80. M. Geilhaupt and Th. Dorfmüller, Chem. Phys. 76, 443 (1983).

81. R. N. Zare, J. Chem. Phys. 40, 1934 (1964).

82. M. L. Sage, Chem. Phys. 35, 375 (1978).

83. M. S. Child, Molecular Collision Theory, (Academic Press, New York, 1974), Appendix A.

TABLE 1. A'-State Lifetimes

Solvent	Decay Time (ps)	
	This work[c]	Ref. 5
CCl_4	2700±400[a]	2700
$CHCl_3$	1120±100[a]	980
CH_2Cl_2	510± 30[a]	500
Hexane	66± 8[b]	~100
Nonane	64± 4[b]	----
Hexadecane	59± 6[b]	~90
Cyclohexane	71± 9[b]	----

a) Times based on absorption decays at 710 and 635 nm.

b) Times based on absorption decay at 350 nm.

c) Error limits are values which double the χ^2 value in the data fit.

TABLE 2. Long Time Absorption Offset Magnitude

Fraction of Peak Height

	Wavelength (nm)		
Solvent	500 nm[a]	350 nm[b]	295 nm[b]
CCl_4[c]	(0.0)	(0.0)	(0.27)
$CHCl_3$[c]	(0.12)	(0.0)	(0.12)
CH_2Cl_2	0.40	0.0	0.30
Hexane	0.38	0.14	0.29
Nonane	0.16	0.08	----
Hexadecane	0.05	0.03	----
Cyclohexane	0.12	0.07	0.10

a) Bleach offset (negative absorbance change)

b) Positive absorbance change

c) Offsets approximate due to slow A'-state decay.

Table 3: Absorption Transients with A'-state Contribution Subtracted
i. Delay to 1/e of maximum (ps); ii. Delay to maximum (ps)

		Wavelength (nm)									
		X-state dynamics						B-state dynamics			
Solvent		1000[c]	860[c]	760	710	635	500[a]	400	370	350	295
CCl_4	i.	26	54	82	110	149	174	7	14	17	35
	ii.	16[b]	28	49	62	86	—	2.4	5.6	6.4	10
$CHCl_3$	i.	16	39	—	90	148	196	—	—	15	27
	ii.	4	12	—	48	80	—	—	—	6	15
CH_2Cl_2	i.	10	22	—	34	52	88	—	—	14	20
	ii.	4	8	—	14	16	—	—	—	5.2	10
Hexane	i.	15	24	—	42	(108)[d]	(116)[d]	5	—	14	21
	ii.	6	12	—	26	(37)[d]	—	1.2	—	2-5	6
Nonane	i.	13	23	—	38	66	(100)[d]	—	—	13	—
	ii.	5	11	—	22	38	—	—	—	4.8	—
Hexadecane	i.	13	23	—	40	58	(84)[d]	—	—	13	—
	ii.	5	10	—	23	34	—	—	—	5.6	—
Cyclohexane	i.	22	38	—	89	(160)[d]	(208)[d]	—	—	14	43
	ii.	7	18	—	46	(67)[d]	—	—	—	4.8	—

a) Transients have a negative absorption change (bleach).
b) Time taken from a shoulder on an early transient.
c) Maximum times may be affected by an unresolved early transient.
d) A'-state component is not resolved. Numbers in parentheses are taken from unsubtracted data.

Figure Captions

FIG. 1. Electronic potential surfaces of I_2 important to the discussion. Five states which correlate with ground state atoms as well as numerous higher states are not shown (Ref. 44). The B state vibrational level initially populated by 590 nm light is labeled. Vertical transitions illustrate the shift in absorption wavelength with vibrational level in both the X and B states.

FIG. 2. Picosecond absorption experiment (1000-350 nm). Heavy line - excitation pulse path, double line - probe pulse path. BS - beamsplitter, DL - delay line, SPF - short pass filters, $\lambda/2$ - half-wave plate, CG - continuum generation cell, BPF - bandpass filters, SF - spatial filter, PD - photodiode, F - filters, REF - reference sample, SAMPLE - primary sample.

FIG. 3. Transient long wavelength absorptions of I_2 in CCl_4. Note vertical scale changes in this and subsequent figures (4 ps/pt).

FIG. 4. Transient absorption at 635 nm of I_2 in chlorinated methanes. Lines represent the A'-state absorption component (4 ps/pt).

FIG. 5. Transient UV absorptions of I_2 in CCl_4, on two time scales. The early component is assigned to B-state absorption and the long component to A'-state absorption. The small intermediate

time component at 400 nm is expanded in Fig. 12.
a) 295 nm - 1.1 ps/pt, 350 nm - 0.4 ps/pt, 370 and 400 nm - 0.8 ps/pt. b) 4 ps/pt, except 295 nm is 5.3 ps/pt.

FIG. 6. Transient UV absorptions of I_2 in hexane, on two time scales. The early component is assigned to B-state absorption and the 65-ps component to A'-state absorption. The long time offsets at 295 and 350 nm are assigned to escaped atoms. a) 295 nm - 2.1 ps/pt, 350 and 400 nm - 0.4 ps/pt. b) 295 nm - 2.1 ps/pt, 350 nm - 4 ps/pt.

FIG. 7. Transient long wavelength absorptions of I_2 in hexane. Lines represent the A'-state absorption component, with decay times fixed by UV A'-state absorption (635 and 710 nm - 4 ps/pt, 860 and 1000 nm - 1.6 ps/pt).

FIG. 8. Transient long wavelength absorptions of I_2 in cyclohexane (1.6 ps/pt, except 710 nm is 0.8 ps/pt).

FIG. 9. Transient bleach at 500 nm of I_2 in chlorinated methanes (4 ps/pt).

FIG. 10. Transient bleach at 500 nm of I_2 in alkanes (4 ps/pt).

FIG. 11. Absorption spectrum of the iodine A' state measured in CCl_4: a) UV spectrum, b) Vis/IR spectrum. ● -this work, ○ -values obtained from Fig. 3 of Ref. 5, Δ -approximate gas phase D'←A' absorption spectrum (Ref. 49), □ -estimated D'←A'

liquid-phase spectrum.

FIG. 12. Transient absorption at 400 nm of I_2 in CCl_4, on an expanded vertical scale (0.8 ps/pt). See also Fig. 5.

FIG. 13. Early portion of the transient absorption at 350 and 635 nm of I_2 in CCl_4 (see also Figs. 3 and 5). Fits to the A'-state contribution to the absorption are shown with a) 8 ps, b) 12 ps, and c) 25 ps exponential rise times. The decay time is 2700 ps in all cases (350 nm - 0.4 ps/pt, 635 nm - 1.6 ps/pt).

FIG. 14. Early portion of the transient absorption at 350 and 710 nm of I_2 in hexane. Fits to the A'-state contribution to the absorption are shown with a) 10 ps, b) 20 ps exponential rise times. The decay time is 66 ps in both cases. Dotted line shows extension of the 66 ps decay without the effects of the rising edge (350 nm - 0.4 ps/pt, 710 nm - 0.8 ps/pt).

FIG. 15. Long wavelength transient absorptions in CCl_4 after subtraction of the A'-state absorption (500 and 635 nm - 4 ps/pt, other wavelengths - 0.8 ps/pt). Circles at 500 nm represent the calculated recovery of ground state absorption from Ref. 4, Fig. 11.

FIG. 16. Vertical difference between the iodine X- and B-state potentials in wavelength vs. X-state vibrational energy. Wavelengths experimentally observed and corresponding vibrational energy levels are marked.

FIG. 17. Time from t=0 to 1/e of the maximum of the absorption due to vibrationally excited X-state molecules. Vibrational energy is associated with absorption wavelength using the difference potential (Fig. 16). ● -CCl_4, ▲-$CHCl_3$, ■ -CH_2Cl_2, ○ -cyclohexane, △-hexadecane (other n-alkanes are similiar).

FIG. 18. i. Quantum mechanical calculation of the relative absorption strength from the iodine X-state vs. the amount of vibrational excitation: a) 500 nm, b) 635 nm, c) 710 nm, d) 760 nm, e) 860 nm, f) 1000 nm. Points where absorption is predicted by the classical model (Fig. 16) are marked on top. ii. Absorption strength at 710 nm, S, and its approximation, S'. The same intervals on the vibrational energy axis are used in approximating all the curves in (i).

FIG. 19. The distribution of the vibrationally excited population in the iodine X-state at several delay times in CCl_4 solution. The average population density over each energy interval (Fig. 18) has been plotted at the center of that interval.

FIG. 20. Effect of different corrections to the classical model for absorption strengths on the derived population distribution in the iodine X state at 50 ps in CCl_4 solution. △-classical model, □-corrected for the change in peak widths and positions, but not including the high energy tail, ● -full quantum mechanical treatment.

FIG. 21. Measured iodine A'-state lifetime as a function of the ionization potential of the solvent. The nearly identical values of the n-alkanes have been averaged to give a single point.

FIG. 22. Lifetime of the trapped electronic state compared to the viscosity of the solvent. Also plotted are the results of Langevin simulations of the A-state relaxation and of an analytical model based on those simulations (Ref. 62). If the trap state is actually the A'-state, as proposed in the text, the models predict much longer lifetimes. ● - experimental points, ○ - simulation results.

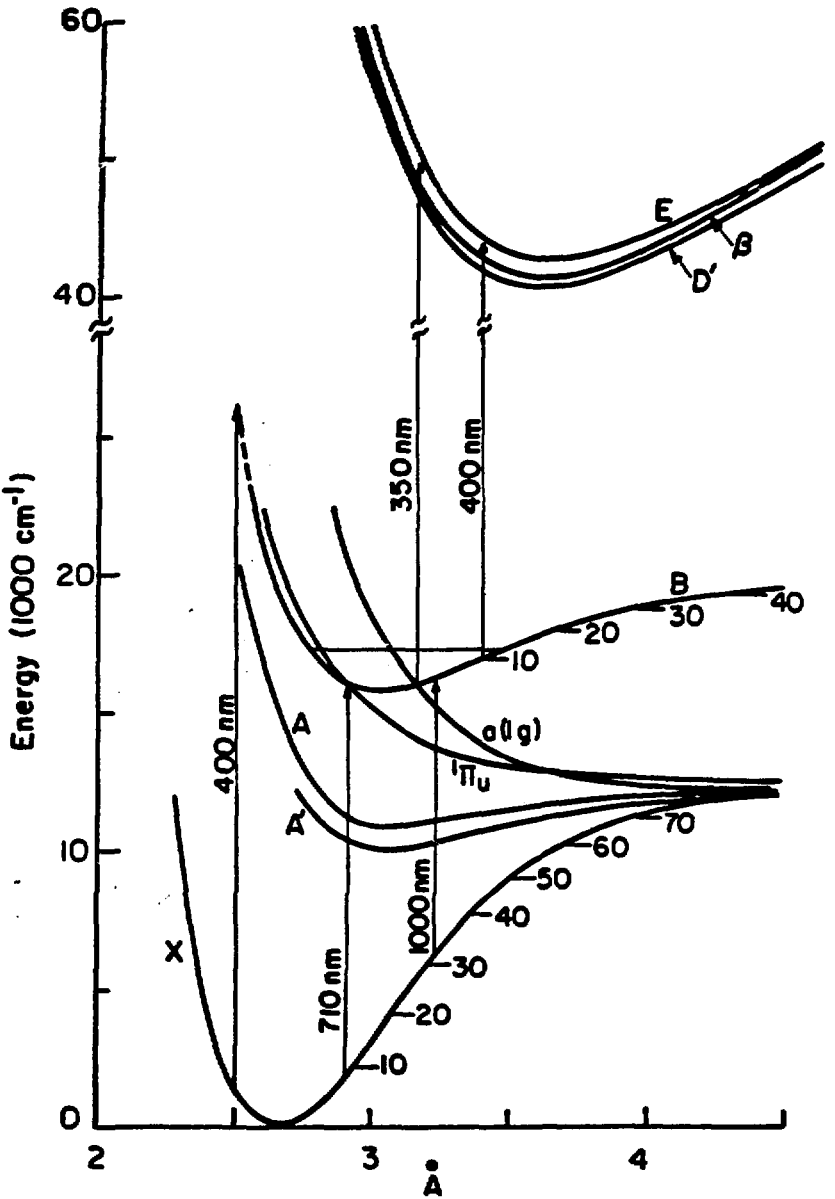
60
40
20
10
0
Energy (1000 cm⁻¹)
2
3
4
Å
E
β
D'
350 nm
400 nm
B
10
20
30
40
a(1g)
¹Πu
A
A'
400 nm
X
710 nm
1000 nm
10
20
30
40
50
60
70

Fig. 1

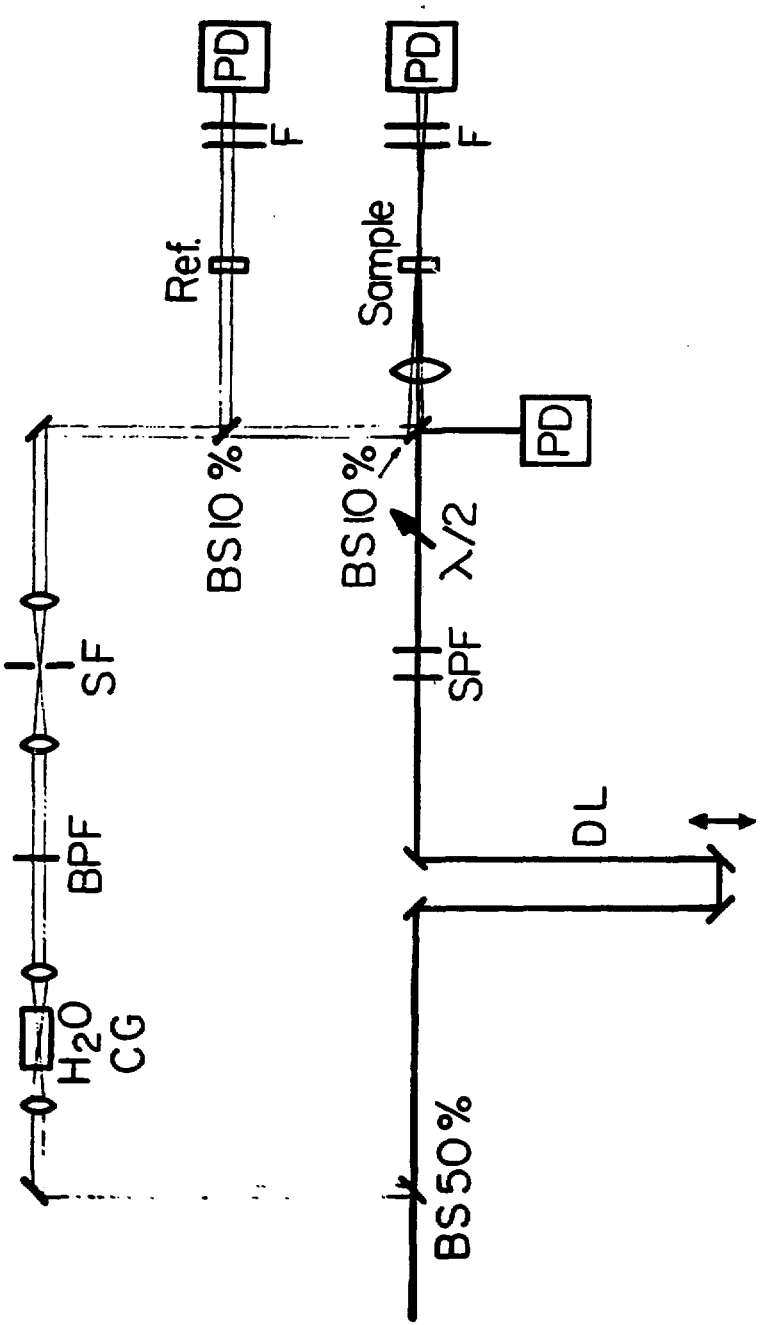

Fig. 2

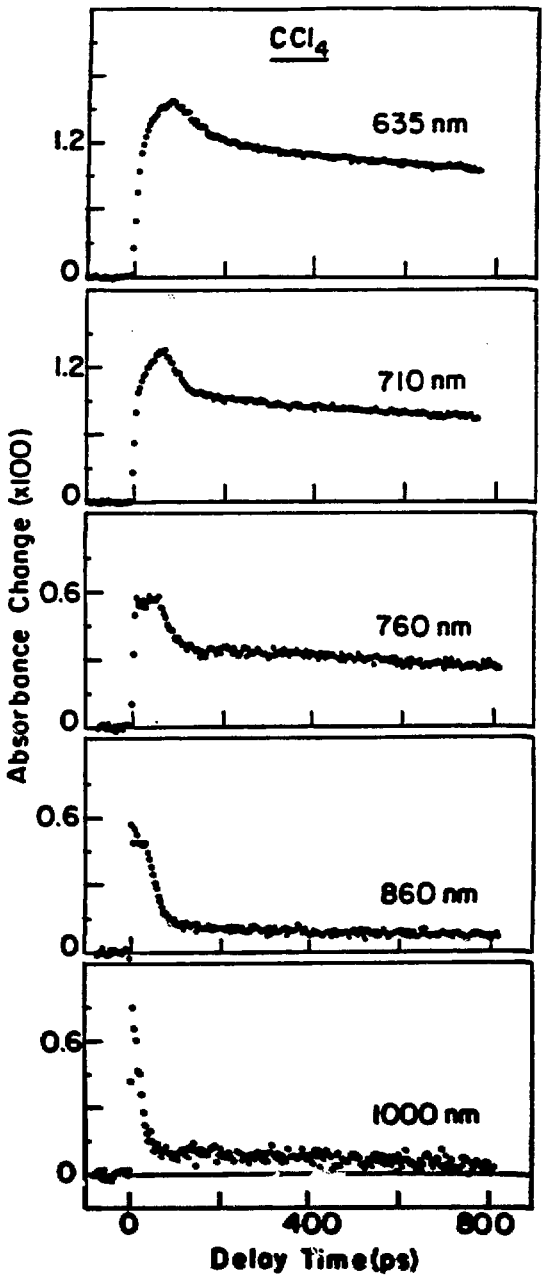
CCl4
635 nm
710 nm
760 nm
860 nm
1000 nm
1.2
0.6
0
Absorbance Change (x100)
0
400
800
Delay Time(ps)

Fig. 3

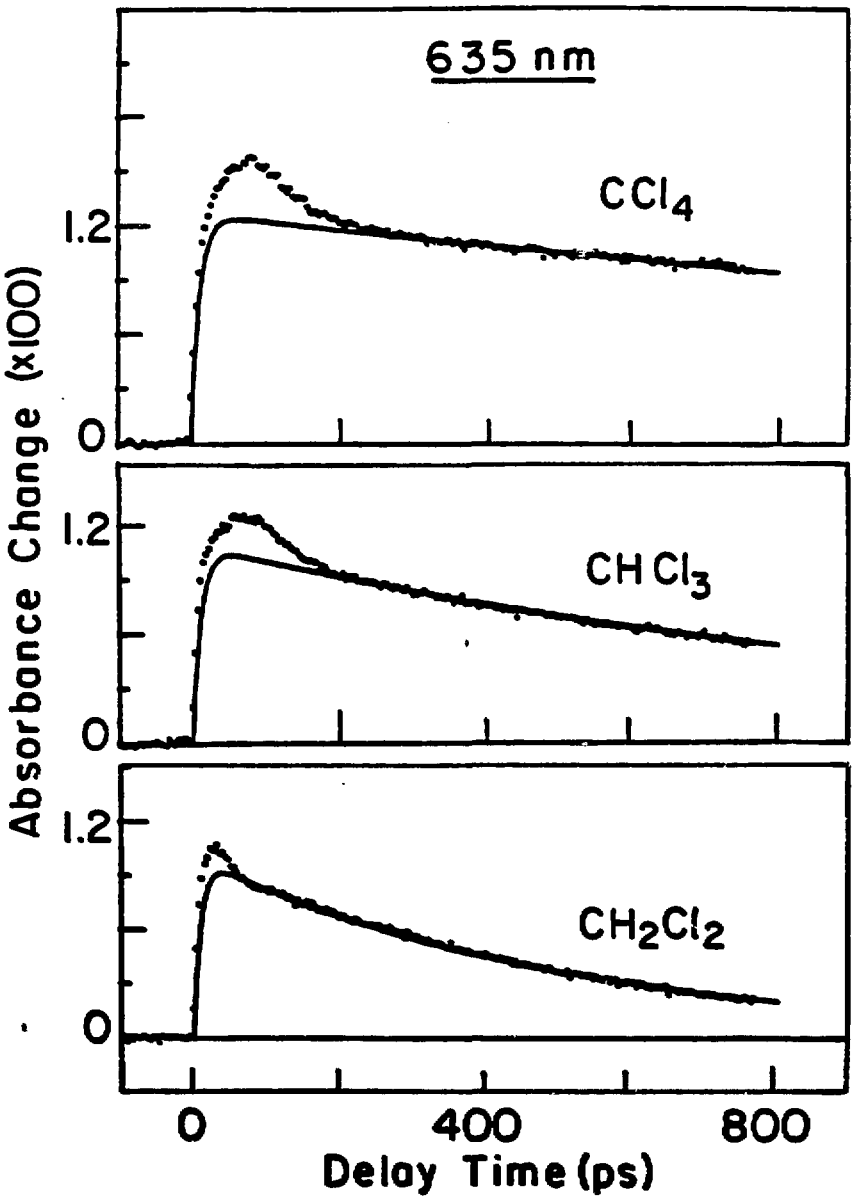
635 nm
CCl4
CHCl3
CH2Cl2
1.2
0
Absorbance Change (x100)
0
400
800
Delay Time (ps)

Fig. 4

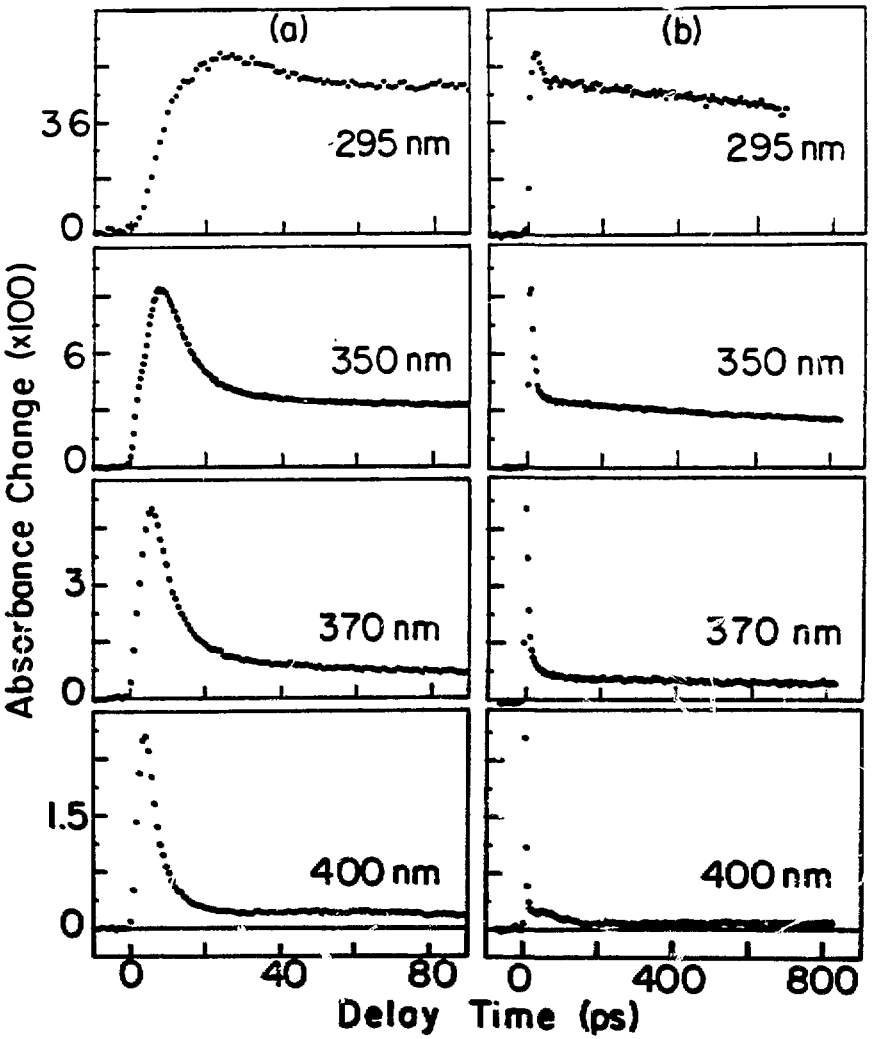
(a)
(b)
295 nm
295 nm
350 nm
350 nm
370 nm
370 nm
400 nm
400 nm
36
0
6
0
3
0
1.5
0
Absorbance Change (x100)
0
40
80
0
400
800
Delay Time (ps)

Fig. 5

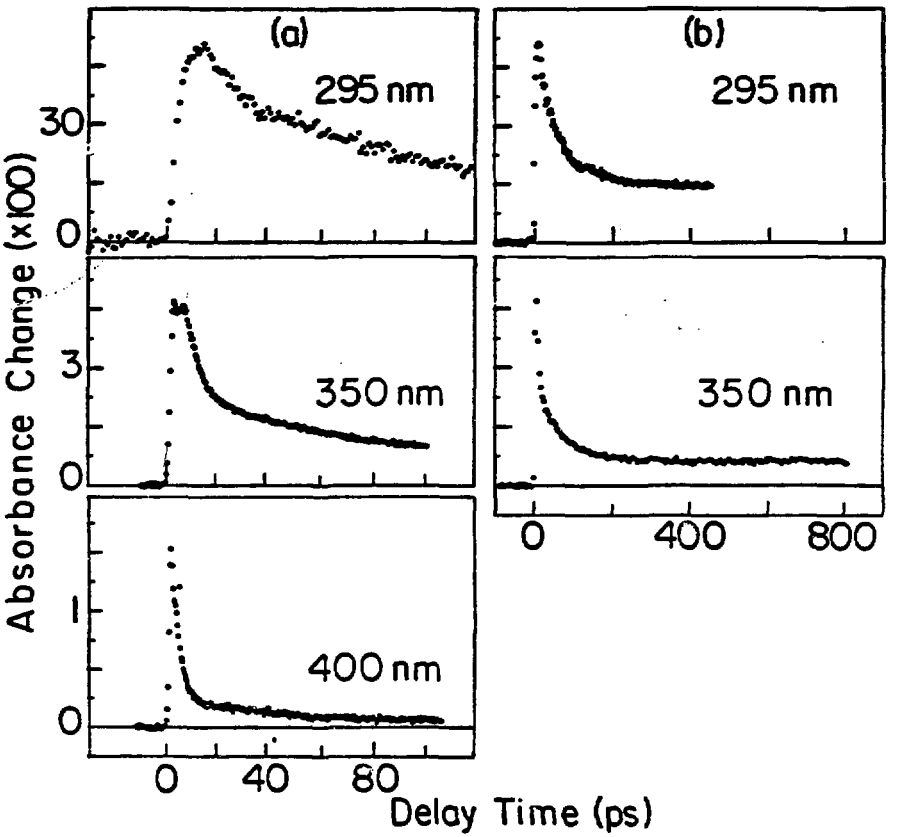
(a)
295 nm
30
0
350 nm
3
0
400 nm
1
0
0
40
80
(b)
295 nm
350 nm
0
400
800
Absorbance Change (x100)
Delay Time (ps)

Fig. 6

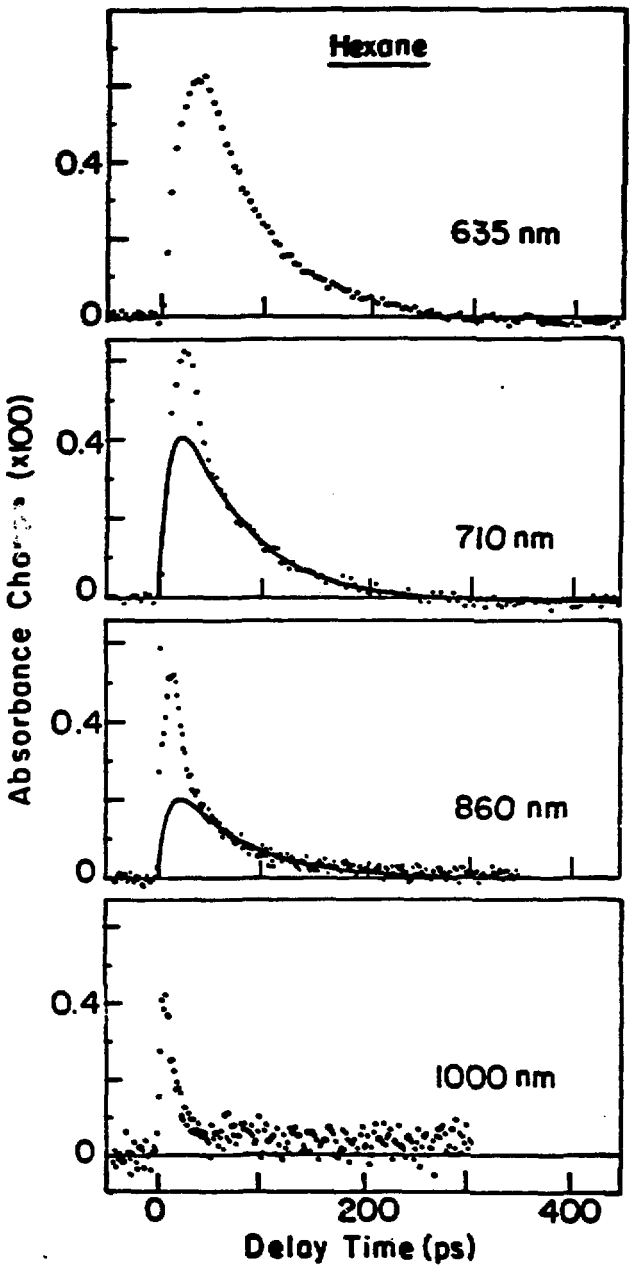
Hexane
0.4
0
635 nm
710 nm
860 nm
1000 nm
Absorbance Change (x100)
0
200
400
Delay Time (ps)

Fig. 7

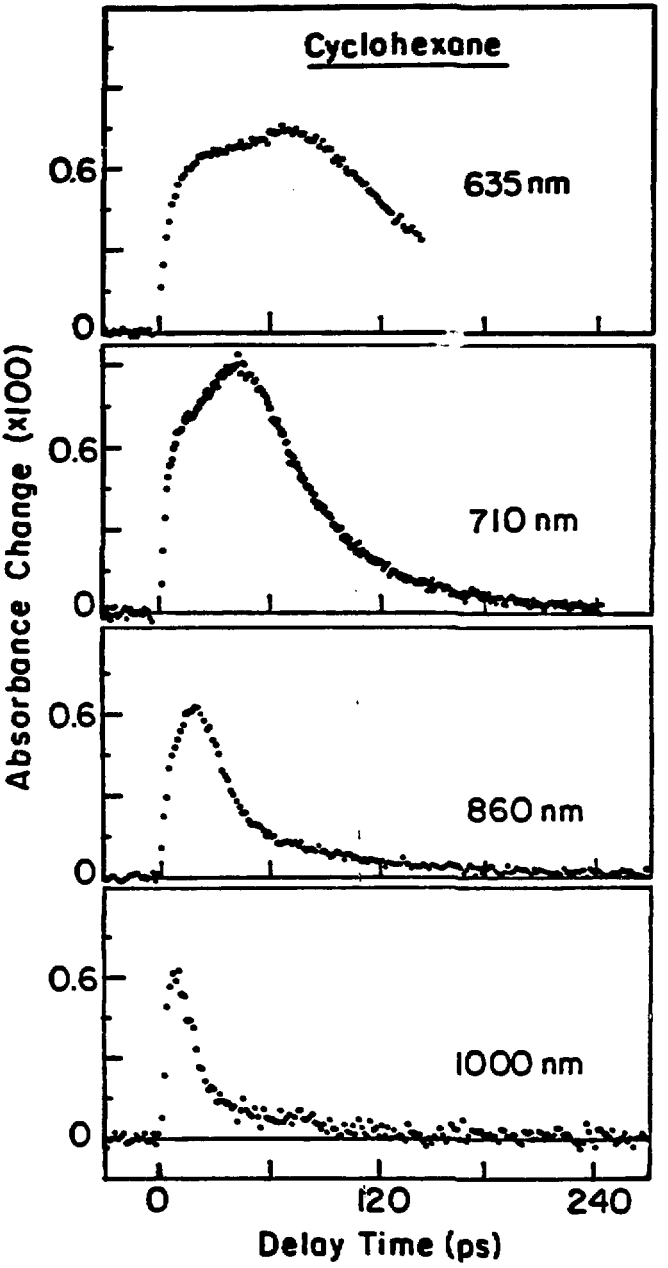
Cyclohexane
635 nm
710 nm
860 nm
1000 nm
0.6
0
Absorbance Change (x100)
0
120
240
Delay Time (ps)

Fig. 8

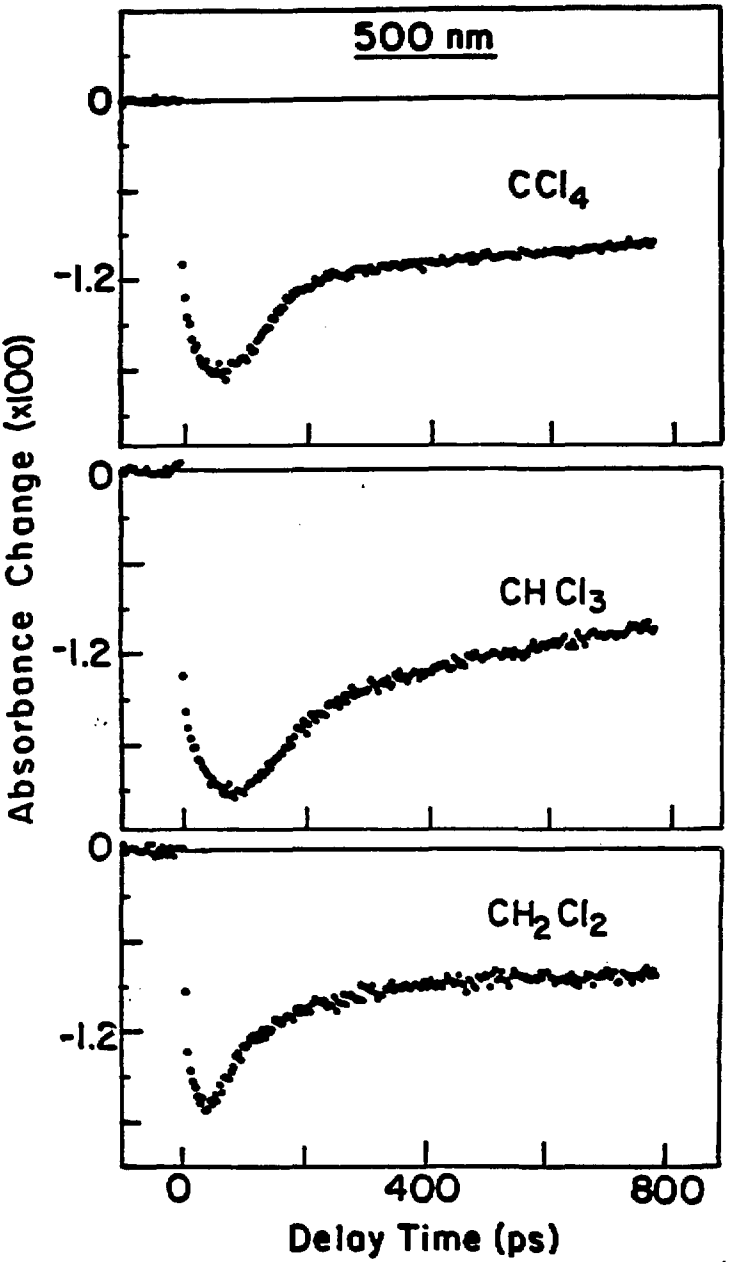
500 nm
0
-1.2
CCl_4
0
-1.2
$CHCl_3$
0
-1.2
CH_2Cl_2
Absorbance Change (x100)
0
400
800
Delay Time (ps)

Fig. 9

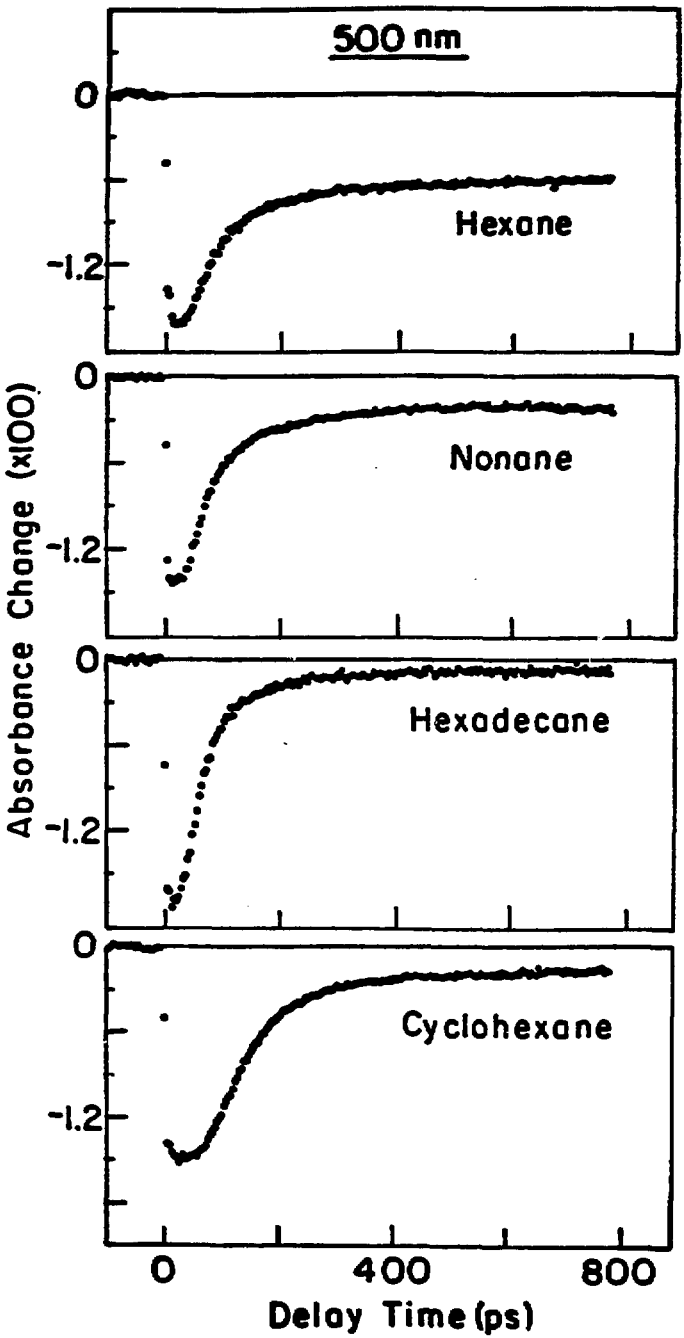
500 nm
0
-1.2
Hexane
Nonane
Hexadecane
Cyclohexane
Absorbance Change (x100)
0
400
800
Delay Time (ps)

Fig. 10

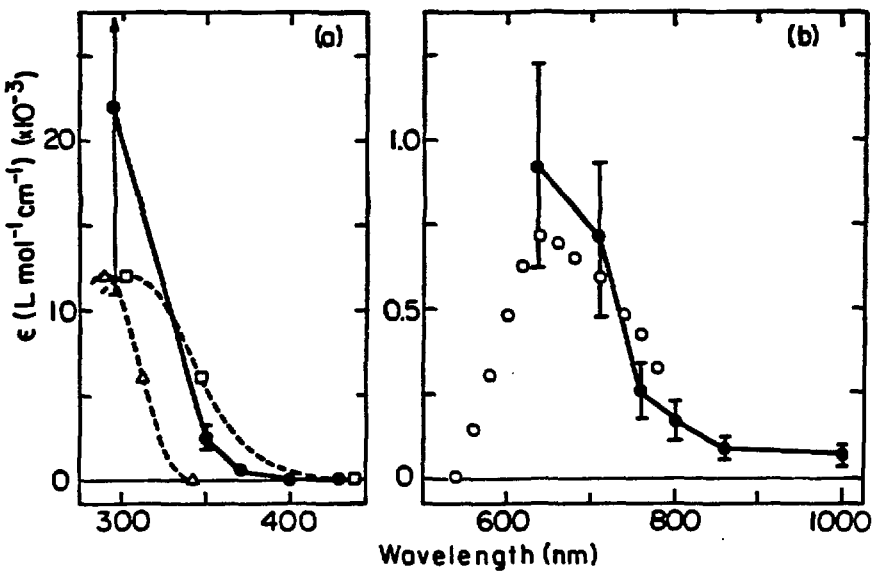
(a)
(b)
ε (L mol⁻¹cm⁻¹) (x10⁻³)
20
10
0
1.0
0.5
0
300
400
600
800
1000
Wavelength (nm)

Fig. 11

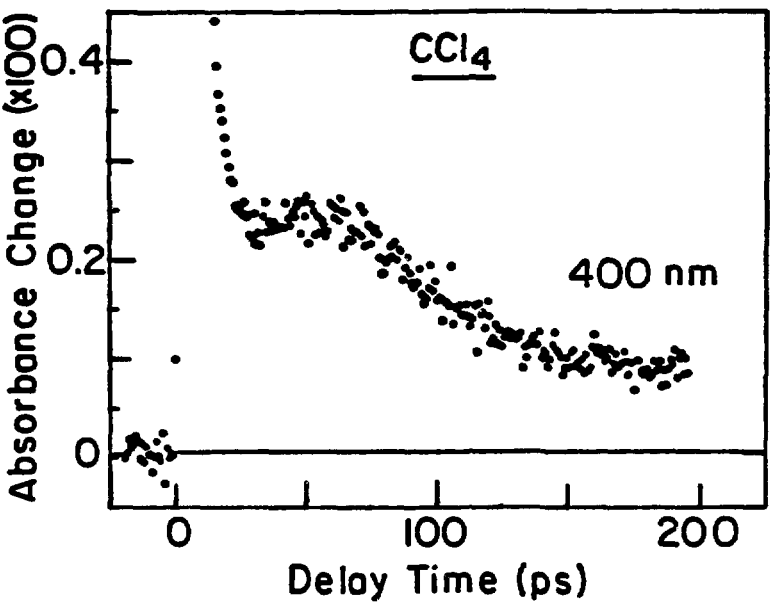
CCl4
400 nm
Absorbance Change (x100)
0.4
0.2
0
0
100
200
Delay Time (ps)

Fig. 12

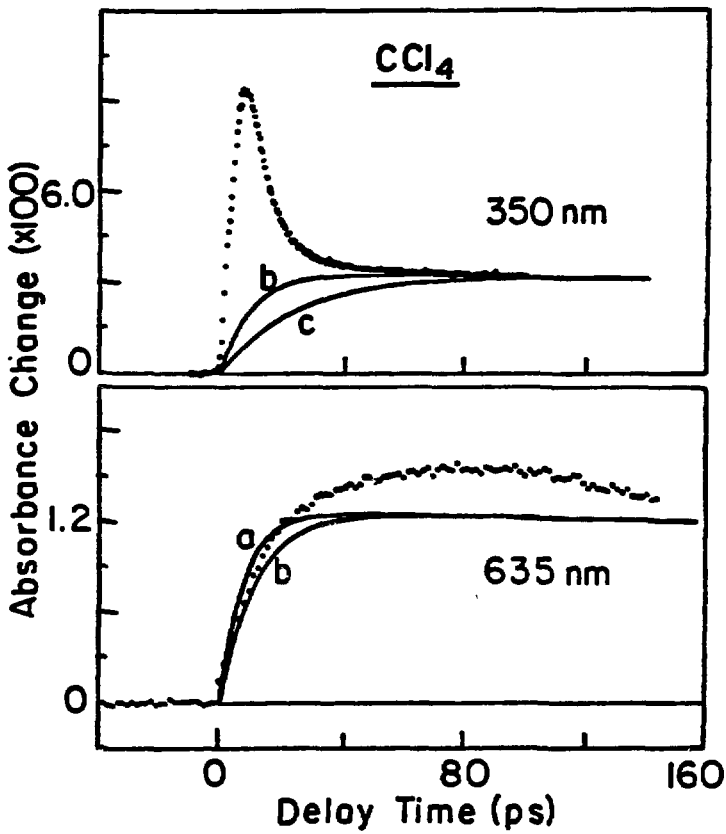
CCl4
350 nm
635 nm
a
b
c
6.0
0
1.2
0
Absorbance Change (x100)
0
80
160
Delay Time (ps)

Fig. 13

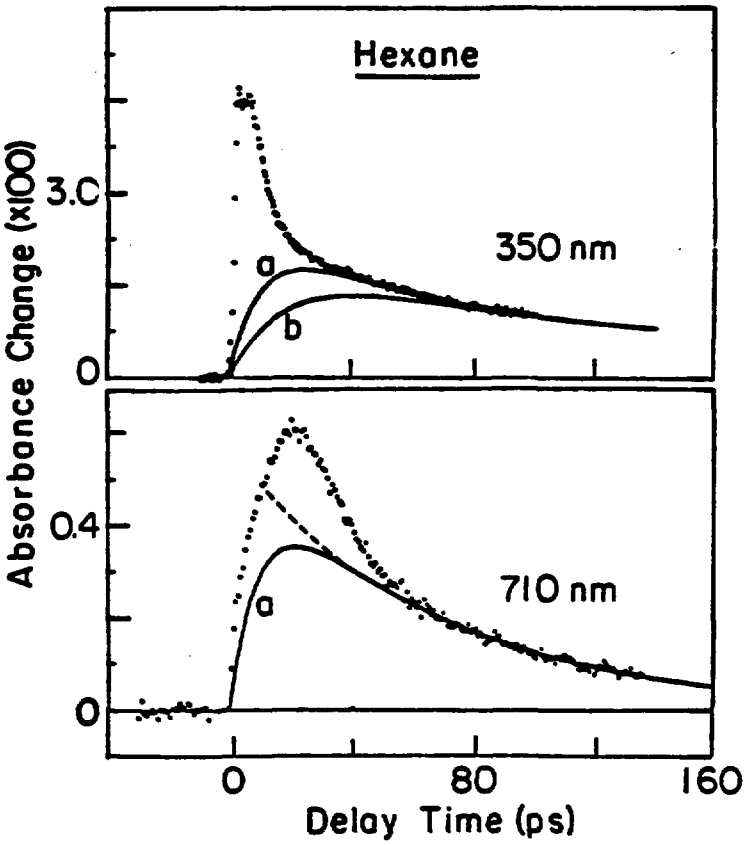
Hexane
350 nm
710 nm
a
b
a
3.0
0
0.4
0
Absorbance Change (x100)
0
80
160
Delay Time (ps)

Fig. 14

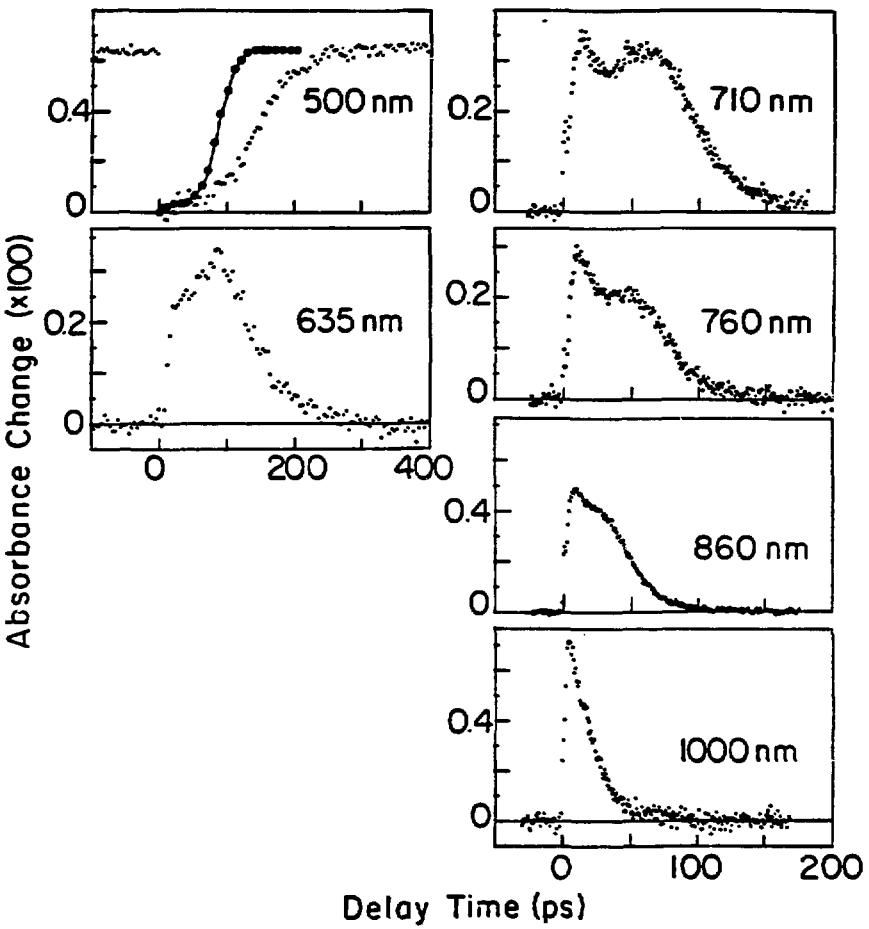
500 nm
710 nm
635 nm
760 nm
860 nm
1000 nm
0.4
0.2
0
0
200
400
100
Absorbance Change (x100)
Delay Time (ps)

Fig. 15

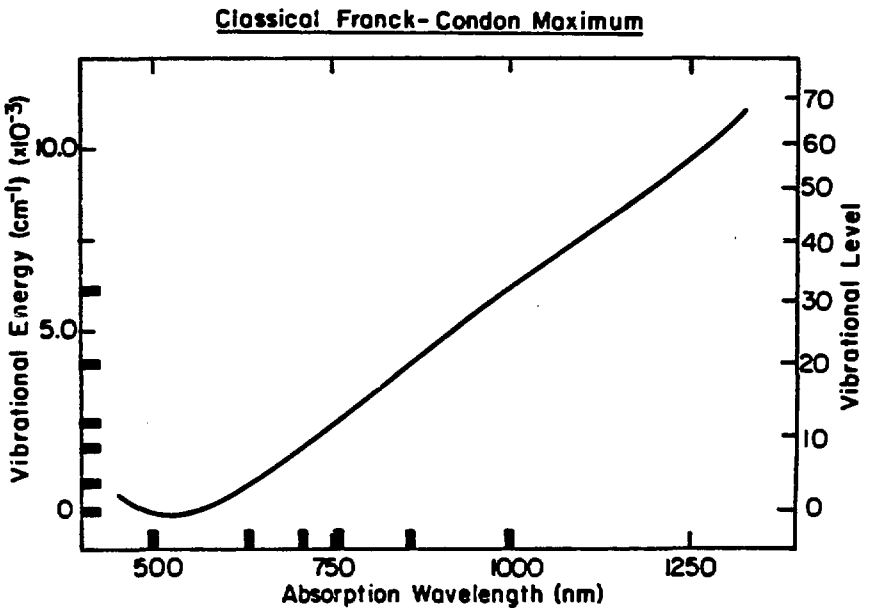
Classical Franck-Condon Maximum
Vibrational Energy (cm⁻¹) (x10⁻³)
10.0
5.0
0
500
750
1000
1250
Absorption Wavelength (nm)
70
60
50
40
30
20
10
0
Vibrational Level

Fig. 16

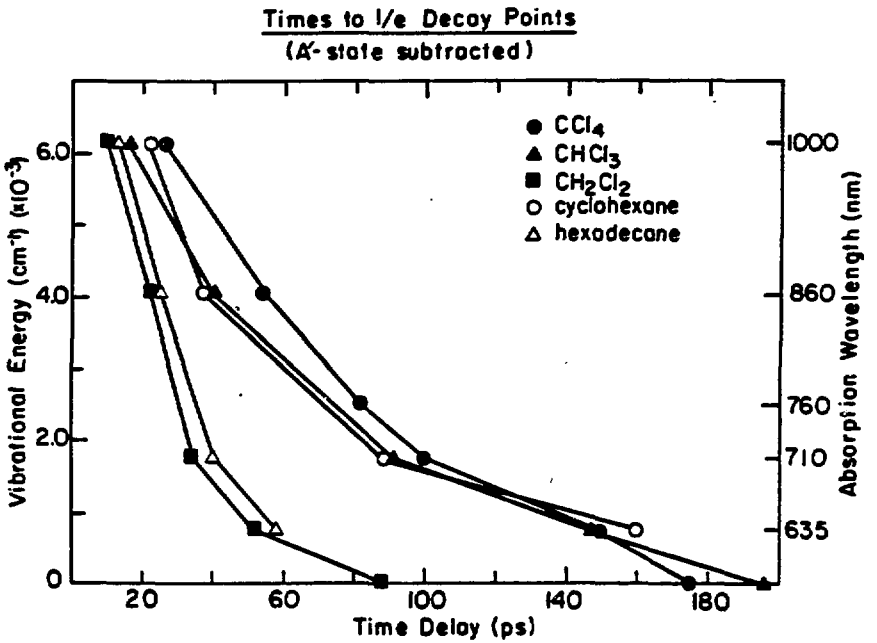
Times to 1/e Decay Points
(A'-state subtracted)
CCl4
CHCl3
CH2Cl2
cyclohexane
hexadecane
Vibrational Energy (cm-1) (x10-3)
6.0
4.0
2.0
0
20
60
100
140
180
Time Delay (ps)
1000
860
760
710
635
Absorption Wavelength (nm)

Fig. 17

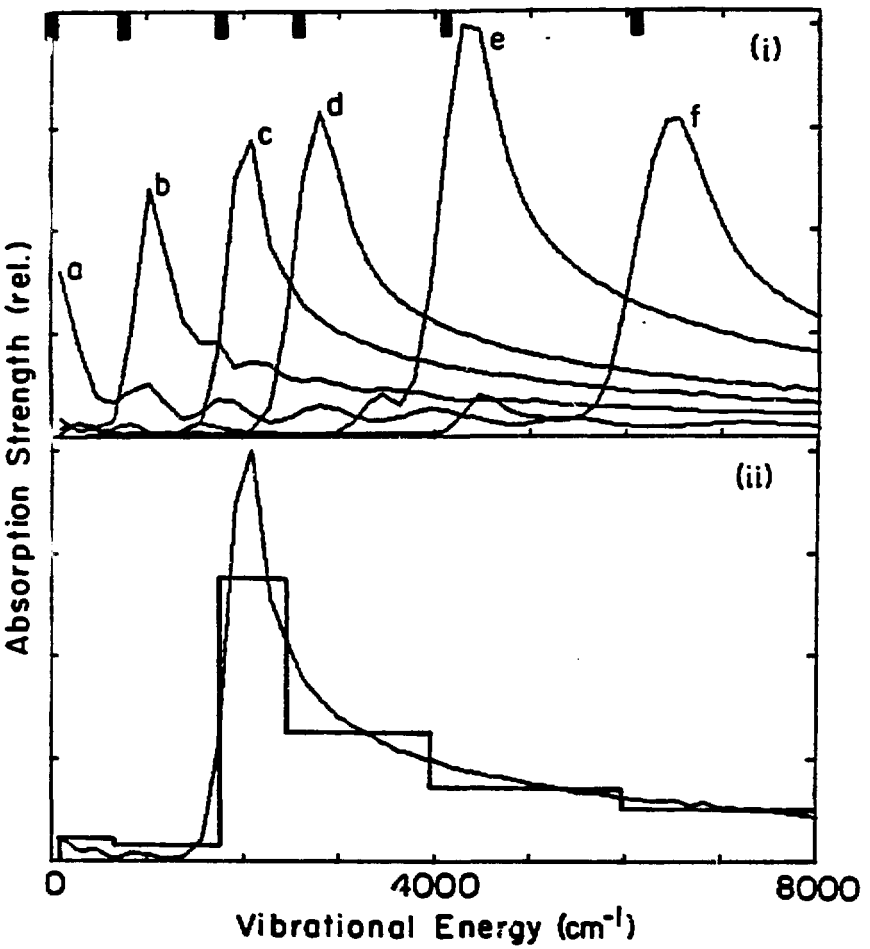
(i)
(ii)
a
b
c
d
e
f
Absorption Strength (rel.)
0
4000
8000
Vibrational Energy (cm⁻¹)

Fig. 18

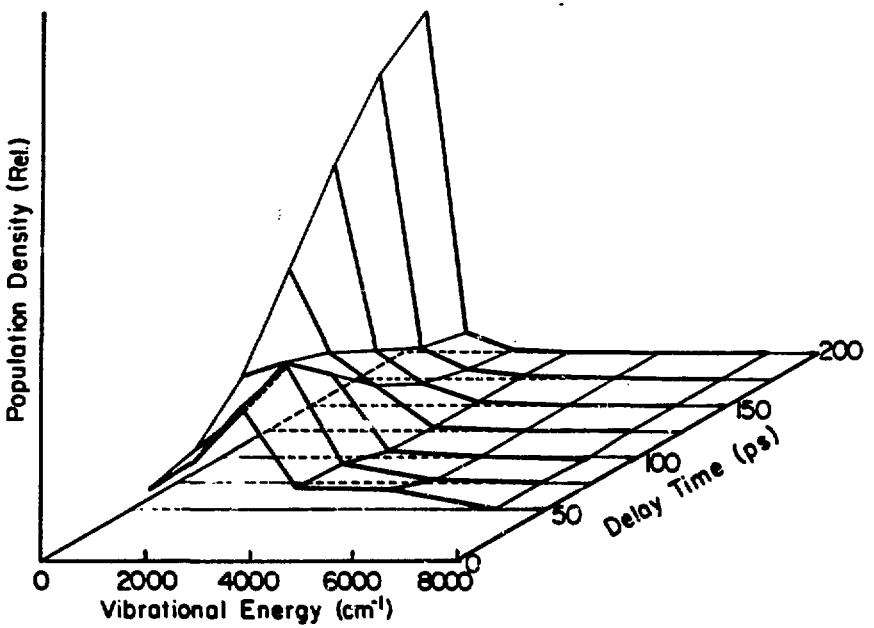
Population Density (Rel.)
0
2000
4000
6000
8000
Vibrational Energy (cm⁻¹)
0
50
100
150
200
Delay Time (ps)

Fig. 19

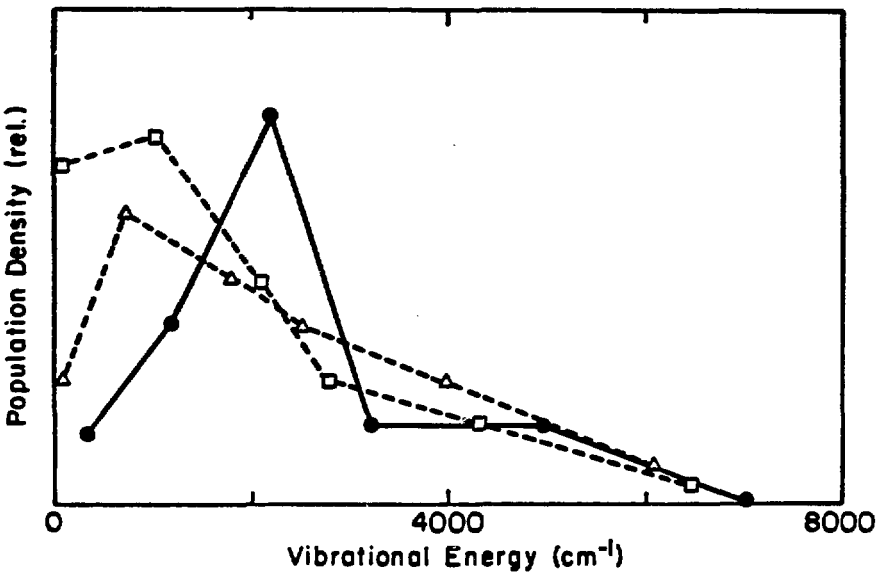

Fig. 20

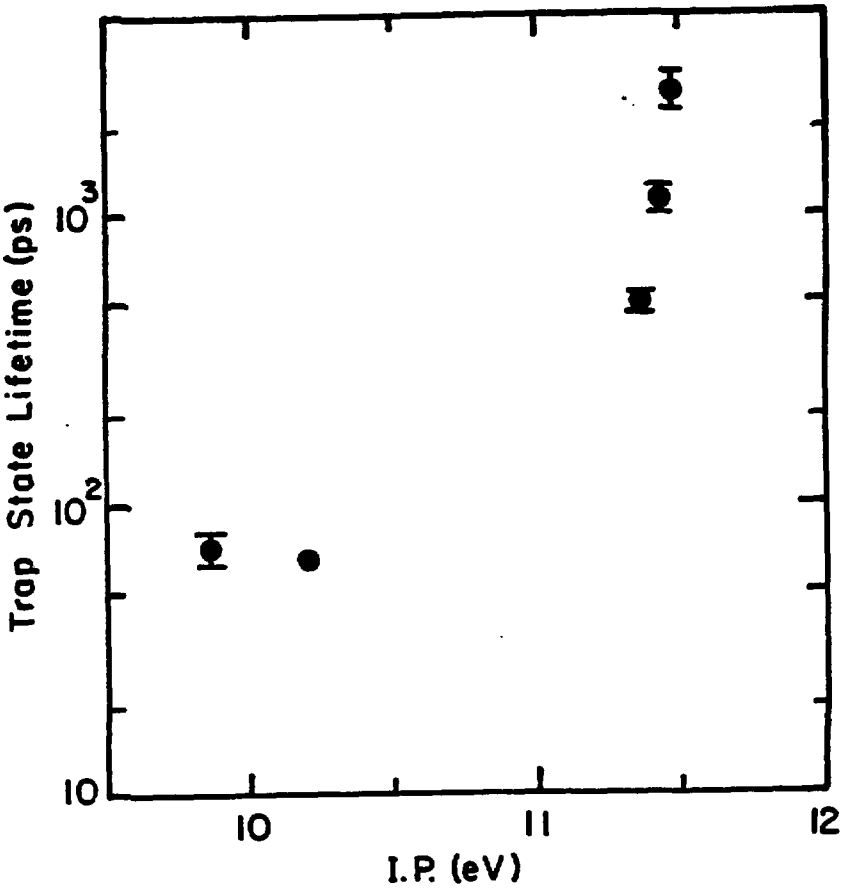

Fig. 21

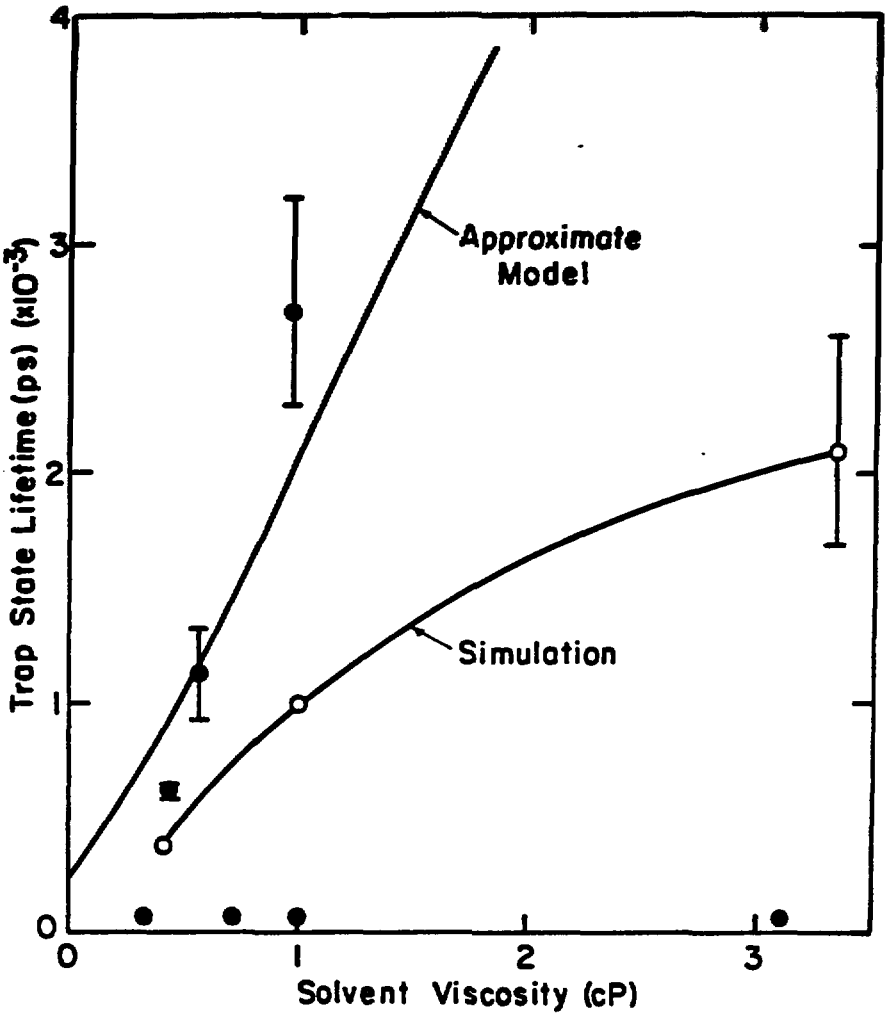
Trap State Lifetime (ps) (x10^{-3})
Solvent Viscosity (cP)
Approximate Model
Simulation
0
1
2
3
4

Fig. 22

CHAPTER III

GENERATION OF PICOSECOND AND NANOSECOND PULSES IN THE VIBRATIONAL INFRARED BY STIMULATED ELECTRONIC RAMAN SCATTERING IN CESIUM VAPOR

A. Introduction

There are few techniques for generating intense, tunable, picosecond pulses in the vibrational infrared, especially below ~3000 cm^{-1}. This is unfortunate since the infrared spectrum contains a great deal of information which would be useful in identifying and monitoring transient intermediates. The visible absorption experiments presented in the last chapter illustrated the problem of broad, overlapping transitions and the difficulty of assigning transitions in the visible region. Furthermore processes such as vibrational relaxation can best be studied by direct excitation of vibrational modes.

Because of the lack of widely tunable lasers operating directly in the vibrational infrared, the generation of picosecond pulses in this region has been based on various frequency shifting mechanisms. Simple difference frequency generation has been reported, but with low peak and average powers.[1,2] Higher peak powers can be generated by using optical parametric generation, but this method suffers from the need to simultaneously tune several crystals and from problems of crystal damage.[3-6] Furthermore, pulses of a few picoseconds duration have only

been generated from low repetition rate, relatively unstable Nd:glass lasers.

Recently, stimulated electronic Raman scattering (SERS) in atomic vapors has been extensively investigated as a method of frequency shifting visible, nanosecond pulses.[7-9] SERS has the advantages of high efficiency, lack of phase-matching requirements and a non-damagable medium. Cotter and Wyatt have also demonstrated that SERS can be extended to picosecond infrared generation, using a pump laser operating in the blue.[10,11] However, the difficulty in operating a blue picosecond laser limits the practical applications of their system. This chapter descibes the development of picosecond SERS from the cesium 6s-5d transition in the red (Fig. 1a). Infrared picosecond pulses in the range 3040-1950 cm^{-1} have been generated with up to 4.6% quantum efficiency. Extensions of this tuning range seem achievable. This technique allows the use of reliable pump lasers such as described in Chapter I, and it is hoped that this feature will make application to experimental problems feasible.

In the nanosecond regime, there is more flexibility in generating pulses in the vibrational infrared, but difficulties still exist. Difference frequency techniques become difficult at lower frequencies, where non-linear crystals absorb. Previous work using SERS has demonstrated the generation of narrowband[12] (~0.5 cm^{-1} bandwidth) and broadband[13,14] (>200 cm^{-1} bandwidth) infrared light pulses, using tunable blue and ultraviolet pump light (for example the 6s-7s transition, Fig. 1a). This technique has the disadvantage of relatively narrow tuning ranges and the need for less reliable blue pump sources. In conjunction with the developement of picosecond SERS on the cesium

6s-5d transition, work was also done to demonstrate that the same technique can provide a broadly tunable source of either narrowband or broadband nanosecond pulses pumped by yellow-red pulses (550 nm to 650 nm). The nanosecond experiments also demonstrate the effect that the photophysics of the cesium dimers and excited monomers can have on the SERS process and will be discussed first.

For both picosecond and nanosecond pulses, absorption of the visible pump light by cesium dimers is a major limitation (Fig. 1c). Nanosecond SERS above 3890 cm^{-1} has been previously demonstrated on the cesium 6s-5d transition,[15] but absorption by cesium dimers prevented tuning into the vibrational infrared region.[15,16] It has been shown, however, that by thermally dissociating the dimers in a superheated vapor,[15] SERS threshold could be reached at 3100 cm^{-1}. In the present work, an improved superheated vapor arrangement allowed wide tunability and routine nanosecond infrared generation down to 900 cm^{-1}. The superheating is even more crucial in getting above threshold for the picosecond process, because of the lower pulse energies available.

The atomic vapor was contained in a helium-buffered split-wick heat pipe,[15] constructed of Inconel 601, which could be heated to 1200° C over a one meter superheated vapor length. Most of the remaining dimers were contained in saturated vapor end sections, even after the end section lengths were minimized by placement of the wicks and adjustment of the heater powers. The best operation was a compromise between shortening the saturated end sections and avoiding unstable interfaces, which produce a mist that blocks visible transmission. The best transmission actually obtained at 560-590 nm and 50 torr vapor pressure was 20%. This compares to a theoretical transmission, calculated using

dimer thermodynamic[17] and visible absorption[18] data, of 68% for a one meter vapor length heated to 1200° C, with no saturated end sections. Further details on the heat pipe design and operation can be found in the thesis of Alex Harris.[19]

To generate infrared, the laser beam of ~6 mm diameter was focused near the middle or far end of the heat pipe using a 3:1 telescope. Infrared energies were measured with a calibrated pyroelectric energy meter, after a germanium filter. All SERS scattering observed was to the 5d $^2D_{5/2}$ sublevel; no scattering to the 5d $^2D_{3/2}$ level was seen.

B. Narrowband Nanosecond Pulses

The narrowband dye laser was a commercial Nd:YAG pumped scanning dye laser. Using rhodamine and DCM dyes, 25-50 mJ light pulses of 5-10 nanosecond duration were obtained from 550 nm to 650 nm. The spectral bandwidth of the light pulses was specified as <0.4 cm^{-1}. The input energy threshold for narrowband SERS infrared generation at 50 torr operating pressure is 2 mJ at 560 nm (3225 cm^{-1} infrared). The threshold rises to 6.5 mJ at 617 nm (1610 cm^{-1} infrared) and rises above the available pump energy of 25 mJ at 645 nm (900 cm^{-1} infrared). The observed increase in the threshold at lower Stokes infrared frequency is somewhat steeper than predicted.[15] Since visible losses at 560 nm and 617 nm are nearly identical, they cannot account for the discrepancy. As has been noted,[12] not all of the factors affecting the SERS gain are yet well understood.

The narrowband infrared energy was recorded as a function of

visible input wavelength. A substantial fraction (~30%) of the infrared energy passing the germanium filter was found to be amplified spontaneous emission (ASE) from excited cesium atom transitions, near 3230 cm^{-1} and 2860 cm^{-1}. These emissions were eliminated or corrected for by using bandpass infrared filters to obtain true tunable SERS energy.

The infrared tuning curves for four dyes are shown in Figure 2a-d. Together, they show tuning from 3450 cm^{-1} to 900 cm^{-1}, with sufficient overlap between dyes to fill the tuning range. The quantum conversion efficiency reaches 2.5% in the range 3300 cm^{-1} to 2600 cm^{-1}, is around 1% at 1700 cm^{-1}, then drops to 0.2% at 900 cm^{-1}. Increased visible absorption by dimers[18] and increased Stokes diffraction losses[15] may cause the lower efficiency below 1700 cm^{-1}.

The bandwidth of the narrowband infrared is 0.5 cm^{-1} at 2250 cm^{-1}, showing a small or nonexistant broadening from the specified visible bandwidth of 0.4 cm^{-1}. The infrared pulse width is typically 3-4 ns, considerably shorter than the visible pump.

The structure in the tuning curves (Fig. 2) can be assigned to absorption of visible or infrared light by 6p and 5d cesium atoms.[20] Cesium dimers predissociate after absorption of visible light in the 550 nm to 650 nm range to give primarily 6p atoms along with some 5d atoms.[21,22] In addition, 5d atoms are created in the SERS process. When the visible pump or the generated infrared light is tuned to a transition from a populated 6p or 5d level to higher levels (Fig. 3), the infrared generation is strongly damped. In addition, when the visible light is absorbed to give highly excited Rydberg atoms, additional infrared ASE is seen from a number of cesium atom transitions

(Fig. 3). Some of this light passes the infrared filters, giving a peak in the plot of infrared energy versus wavelength. While at most wavelengths the tuning curves show true SERS energy, these sharp peaks are predominantly fixed frequency ASE emissions.

C. Broadband Nanosecond Pulses

In order to generate broadband infrared pulses, the pump radiation was obtained from a broadband dye laser consisting of the dye amplifier originally constructed to amplify picosecond dye laser pulses (Chapt. I). The amplifier was modified by placing a mirror at the input end and by turning off the saturable absorber dye jets which normally isolate one stage from the next.

The threshold for infrared generation with broadband pulses centered at 560 nm is identical to the narrowband threshold at 560 nm. The threshold to longer wavelengths increases similarly in both cases. The lack of dependence on bandwidth is in agreement with experimental work on other transitions,[13,14] but contrasts sharply with previous work on the 6s-5d transition.[15] Theoretical calculations predict that the Raman gain should not be affected by increased bandwidth due to frequency modulation,[23] but any associated amplitude modulation is difficult to model. In any case, the present result demonstrates that the SERS threshold on this transition does not change even when the bandwidth is increased from 0.5 cm^{-1} to >200 cm^{-1}.

The ~4-ns broadband visible pulses generate infrared pulses shorter than the 1.5 nanosecond response time of the Au:Ge detector. Table 1

summarizes the visible and infrared pulse energies obtained with broadband pulses, and the infrared ranges covered with each broadband dye. The visible-to-infrared photon conversion efficiency, shown in the last column of Table 1, decreases at lower frequencies, as in the narrowband infrared generation. The 14 mJ of broadband light from DCM was insufficient to reach threshold, which should be in the range of 15-20 mJ based on narrowband measurements. A more efficient broadband dye laser would improve the dye energies, broaden the tuning ranges, and might allow broadband generation well below 1800 cm^{-1}.

The broadband infrared spectra (Fig. 4) show dips at the same points as found in the narrowband spectra, due to excited cesium atom absorptions. When the visible pulse overlaps 6p visible absorptions, the output contains a number of ASE lines, as in the case of the narrowband pulses. It is estimated that ASE lines account for approximately 30% of the measured broadband infrared energies listed in Table 1.

The energies obtained in both the narrowband and broadband infrared generation compare reasonably well with previous results obtained on a series of higher cesium and rubidium transitions using blue and ultraviolet dyes.[12-14] The advantage of the present method lies in the use of a single vapor and a single transition, along with reliable rhodamine dyes, to produce wide tuning ranges. Including the results of previous work,[15] coherent infrared radiation can now be generated from 6000 cm^{-1} to 900 cm^{-1} (1.7 μm to 11.1 μm) on the 6s-5d cesium transition, giving the broadest SERS tuning range obtained to date on a single atomic transition.[24] Further reductions in the dimer density would be expected to improve the efficiency and reduce the structure in

the tuning curves and might extend the tuning range to even lower frequencies.

D. Picosecond Pulses

Visible picosecond pulses were used from the amplified picosecond dye laser described in Chapter I. Because of the high energy needed, a great deal of attention was paid to optimizing the picosecond energy, which resulted in pulses of 1-2 mJ. The SERS threshold is lowest when the beam profile is smooth and uniform. This occurs when water is used as the dye solvent. If methanol is used, the turbulence of the dye flow occuring in the final amplifier stage is translated into random intensity variations across the amplified beam profile. Since this results in poorer focusing of the beam, the threshold of the SERS process is raised. The higher energies generally obtained with methanol solutions compensate somewhat for the detrimental effects of turbulence.

The lowest thresholds occurred with a buffer gas pressure of 50-60 Torr. Fixed frequency emissions near 3230 cm^{-1} (7p-7s) and 2860 cm^{-1} (5d-6p) accounted for a significant fraction of the infrared energy and were either blocked by infrared filters or corrected for in the energy measurements. The median infrared SERS energy obtained, as well as the visible energy used to obtain it, are shown as a function of wavelength in Figure 5. A peak quantum efficiency of 4.6% occured at 2520 cm^{-1}. The dip in infrared generation near 2850 cm^{-1} is due to the lack of a good dye for amplification of the picosecond pulse. This can probably be remedied by using different solvents to shift the dye tuning curves.[26]

The bandwith of the infrared pulses varied from 6 to 10 cm^{-1}. This implies an infrared pulse length of 1-2 ps, if a Gaussian bandwidth limited pulse is assumed.[27] Since stimulated Raman scattering in the transient limit is expected to generate a Stokes pulse shorter than the pump pulse,[28] it is reasonable to believe that the infrared pulse is of this length. Furthermore, previous work on the cesium 6s-7p transition has implied a similiar infrared pulse width.[10]

The experiments with nanosecond pulses showed that infrared can be generated over a very wide tuning range (3500 to 900 cm^{-1}). However a reduction in picosecond SERS efficiency occurs below 2500 cm^{-1} and is probably due to an increase in the non-linear losses that occurs with shorter pulses. This conclusion is based on the fact that the tuning range can be extended by using longer pulses which have lower peak intensities but the same total energy. Figure 6 shows a large increase in SERS energy at 2350 cm^{-1} as the input pulse to the dye amplifier is broadened.[29] At shorter wavelengths the SERS energy is relatively insensitive to pulse width. In the transient regime the SERS process should not be affected by pulse width changes at constant energy;[30] thus, the results of Figure 6 imply that competing non-linear effects are being significantly reduced as the pulse width is increased. Furthermore, by broadening the input pulse autocorrelation from 2.2 ps to 21 ps, the transmission of the visible pulse through the heat pipe increases approximately 10%.

As an example of the increased tuning range of longer pulses, Figure 5 (squares) shows the SERS energy generated over the tuning curve of Kiton Red in water with 21 ps input pulses (~10 ps amplified pulse). Significant amounts of SERS were also generated at the far end

of the dye laser tuning range (1950 cm^{-1}), although the actual energy was not measured. These results suggest that tuning even further into the vibrational infrared should be possible with the longer pulses.

The likely sources of non-linear loss are two photon ionization of cesium atoms or cesium dimers. Unfortunately experimental cross sections for these processes do not extend to the wavelengths used here.[31] The calculated cross section for the two photon ionization of cesium atoms,[32] however, is of the correct magnitude to contribute to the losses for 1-2 mJ pulses whose widths are on the order of a picosecond and is increasing with longer wavelength in this region.

It should be noted that a small amount of SERS was observed at the far end of the dye laser tuning range (1950 cm^{-1}) even with short pulses (see Fig. 5). The increase in the generated infrared may result from approaching a minimum in the dimer absorption at 615 nm.[33] This suggests that a further reduction of the dimer concentration might extend the tuning range for the shorter pulses.

In summary, SERS from the 6s-5d transition in cesium has been demonstrated as a practical source of intense picosecond infrared from 3040-1950 cm^{-1} using rhodamine dye lasers. No tuning limitations to shorter wavelengths are forseen. Tuning to longer wavelengths with broad (>10 ps) pulses also seems possible. However, tuning below 2300 cm^{-1} with <1 ps pulses may require additional reductions in the cesium dimer concentration. Further understanding of the exact origin of the non-linear losses will ultimately determine how well the 6000-900 cm^{-1} tuning range for nanosecond pulses can be matched by picosecond pulses on this transition.

References

1. C. A. Moore and L. S. Goldberg, Opt. Commun. 16, 21 (1976).
2. I. S. Ruddock and R. Illingworth, L. Reekie, Appl. Phys. B 29, 177 (1982).
3. A. Seilmeier and W. Kaiser, Appl. Phys 23, 113 (1980).
4. A. Fendt, W. Kranitzky, A. Laubereau and W. Kaiser, Opt. Commun. 28, 142 (1979).
5. B. Bareika, G. Dilchyus, E. D. Isyanova, A. Piskarskas and V. Sirutkaitis, Sov. Tech. Phys. Lett. 6, 301 (1980).
6. T. Elsaesser, A. Seilmeier, and W. Kaiser, Opt. Commun. 44, 293 (1983).
7. For example: a) J. Manners, Opt Commun. 44, 366 (1983). b) P. Bernage, P. Niay, and R. Houdart, Opt. Commun. 36, 241 (1981). R. Burnham and N. Djeu, Opt. Lett. 3, 215 (1978). D. Cotter and D. C. Hanna, Opt. and Quantum Electron. 9, 509 (1977).
8. R. T. Hodgson, Appl. Phys. Lett. 34, 58 (1979).
9. R. Wyatt and D. Cotter, Appl. Phys. 21, 199 (1980).
10. R. Wyatt and D. Cotter, Opt. Commun. 37, 421 (1981).
11. R. Wyatt and D. Cotter, Opt. Commun. 32, 481 (1980).
12. D. Cotter, D. C. Hanna, and R. Wyatt, Optics Commun. 16, 256 (1976).
13. D. S. Bethune, J. R. Lankard, M. M. T. Loy, and P. P. Sorokin, IBM J. Res. Develop. 23, 556 (1979).
14. D. S. Bethune, A. J. Schell-Sorokin, J. R. Lankard, M. M. T. Loy and P. P. Sorokin, in Advances in Laser Spectroscopy, Vol. II, edited by B. A. Garetz and J. R. Lombardi (Wiley-Interscience, New

York, 1983).

15. R. Wyatt and D. Cotter, Appl. Phys. 21, 199 (1980).

16. R. T. Hodgson, Appl. Phys. Lett. 34, 58 (1979).

17. D. R. Stull and G. C. Sinke, Thermodynamic Properties of the Elements, Adv. Chem. Ser., No. 18 (Amer. Chem. Soc., Washington, D.C., 1956).

18. M. Lapp and L. P. Harris, J. Quant. Spectrosc. Radiat. Transfer 6, 169 (1966).

19. A. L. Harris, Ph.D. thesis (University of California, Berkeley, California, 1985).

20. Notable exceptions are: unassigned broad dips at 611 nm (1770 cm^{-1} infrared), due to visible absorption, and 619 nm (1570 cm^{-1} infrared), due to infrared absorption; and a sharp absorption at 560.8 nm (3230 cm^{-1} infrared), due to cesium atom 7s-7p infrared absorption.

21. C. B. Collins, F. W. Lee, J. A. Anderson, P. A. Vicharelli, D. Popescu, and I. Popescu, J. Chem. Phys. 74, 1067 (1981).

22. M. Raab, G. Honing, W. Demtroder and C. R. Vidal, J. Chem. Phys. 76, 4370 (1980).

23. M. G. Raymer and J. Mostowski, Phys. Rev. A 24, 1980 (1981).

24. Although tuning between 3890 cm^{-1} and 3450 cm^{-1} has not yet been demonstrated, the threshold should be similar to Rhodamine 590.

25. K. H. Drexhage, Laser Focus, March 1973.

26. E. P. Ippen and C. V. Shank in Ultrashort Light Pulses, edited by S. L. Shapiro (Springer-Verlag, New York, 1977), p. 88.

27. R. L. Carmen, F. Shimizu, C. S. Wang and N. Bloembergen, Phys. Rev. A 2, 60 (1970); S. M. George and C. B. Harris, Phys. Rev. A

28, 863 (1983).

28. Experience has shown (Chapter I) that the amplified pulse width scales with the input pulse width, but remains shorter. The amplified pulse energy and bandwidth, however, remain approximately constant.

29. A. Laubereau and W. Kaiser, Rev. Mod. Phys. 50, 607 (1978).

30. J. Morellec, D. Normand, G. Mainfray, and C. Manus, Phys. Rev. Lett. 44, 1394 (1980).

31. H. Bebb, Phys Rev. 149, 25 (1966).

32. M. Lapp and L. P. Harris, J. Quant. Spectrosc. and Radiat. Transfer 6, 169 (1966).

Figure Captions

Fig. 1. Spectroscopy of cesium atoms and dimers. a. lower energy levels of the cesium atom. The SERS transition used here, as well as one based on a blue pump are shown. b. two-photon ionization cross section of the cesium atom. c. visible absorption spectrum of the cesium dimer.

Fig. 2. Narrowband infrared energy obtained as a function of visible pump wavelength for four visible dyes. Arrows mark dips or ASE emission peaks resulting from 6p or 5d cesium atom absorptions. Lines in (a) mark dips assigned to 7s and 9s cesium atom absorptions. Asterisk in (b) marks atmospheric CO_2 infrared absorption.

Fig. 3. Cesium dimer potential curves and the predissociative transition leading to excited cesium atoms. Visible and infrared absorptions of these excited atoms and resulting infrared fluorescence transitions are marked.

Fig. 4. Typical spectrum of the broad band infrared pulses. Arrows mark dips and peaks due to excited cesium atoms (see also Fig. 2). Lines mark atmospheric CO_2 absorptions.

Fig. 5. Top: Visible pump pulse energy versus wavelength; a. R 590, b. R 610, c. KR 620, d. R 640; ● - methanol solutions, ▲- water solutions (no surfactants). Points used for best SERS generation are outlined with the solid portions of the curves. Bottom: ● - SERS energy

generated with short pulses, ■ - SERS energy generated with broad pulses.

Fig. 6. SERS energy generated at 2350 cm^{-1} versus autocorrelation width of the input to the dye amplifier. Autocorrelation widths are measured at one quarter of the maximum height.

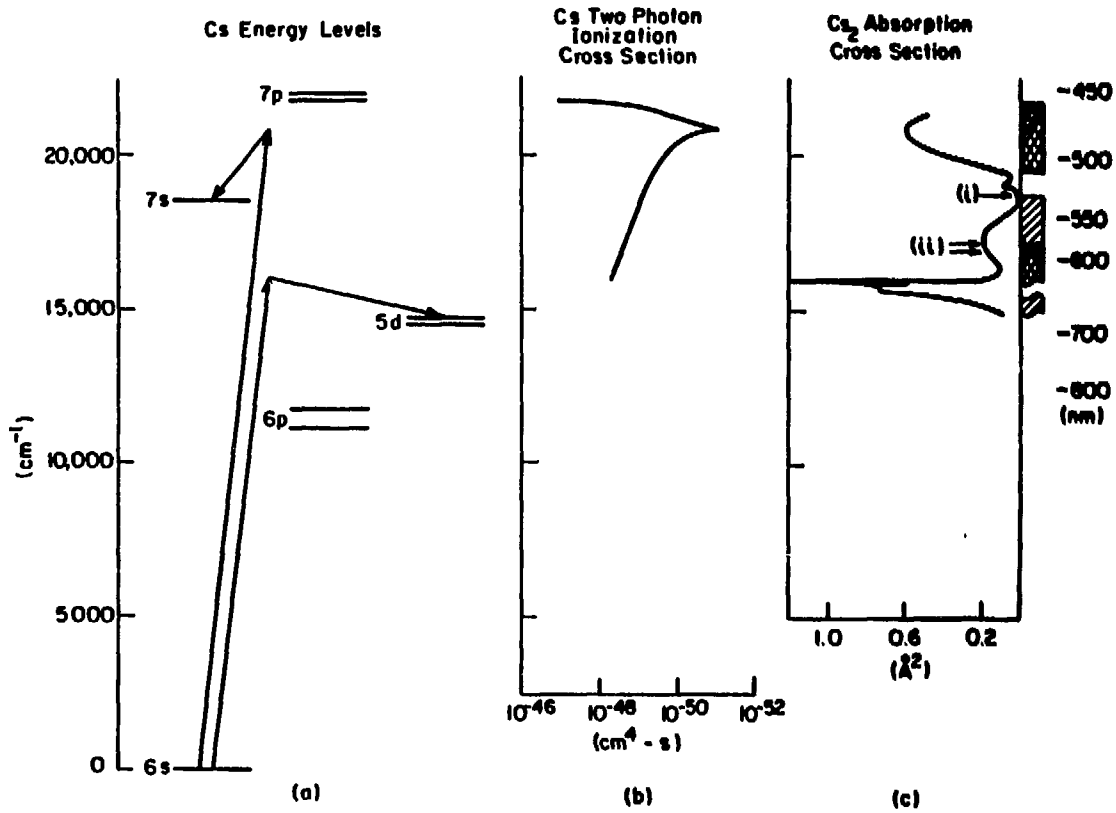
Cs Energy Levels
Cs Two Photon Ionization Cross Section
Cs_2 Absorption Cross Section
7p
7s
5d
6p
6s
20,000
15,000
10,000
5000
0
(cm^{-1})
10^{-46}
10^{-48}
10^{-50}
10^{-52}
(cm^4 - s)
-450
-500
-550
-600
-700
-800
(nm)
(i)
(ii)
(iii)
1.0
0.6
0.2
(Å^{-2})
(a)
(b)
(c)

Fig. 1

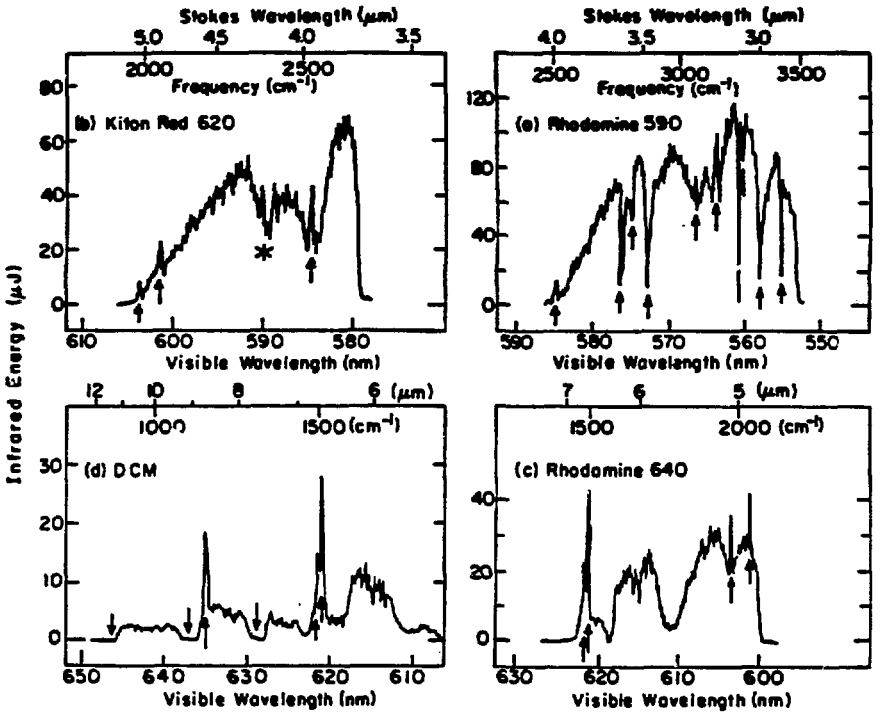
Stokes Wavelength (μm)
5.0
4.5
4.0
3.5
2000
2500
Frequency (cm⁻¹)
(b) Kiton Red 620
Visible Wavelength (nm)
Stokes Wavelength (μm)
4.0
3.5
3.0
2500
3000
3500
Frequency (cm⁻¹)
(a) Rhodamine 590
Visible Wavelength (nm)
Infrared Energy (μJ)
12
10
8
6 (μm)
1000
1500 (cm⁻¹)
(d) DCM
Visible Wavelength (nm)
7
6
5 (μm)
1500
2000 (cm⁻¹)
(c) Rhodamine 640
Visible Wavelength (nm)

Fig. 2

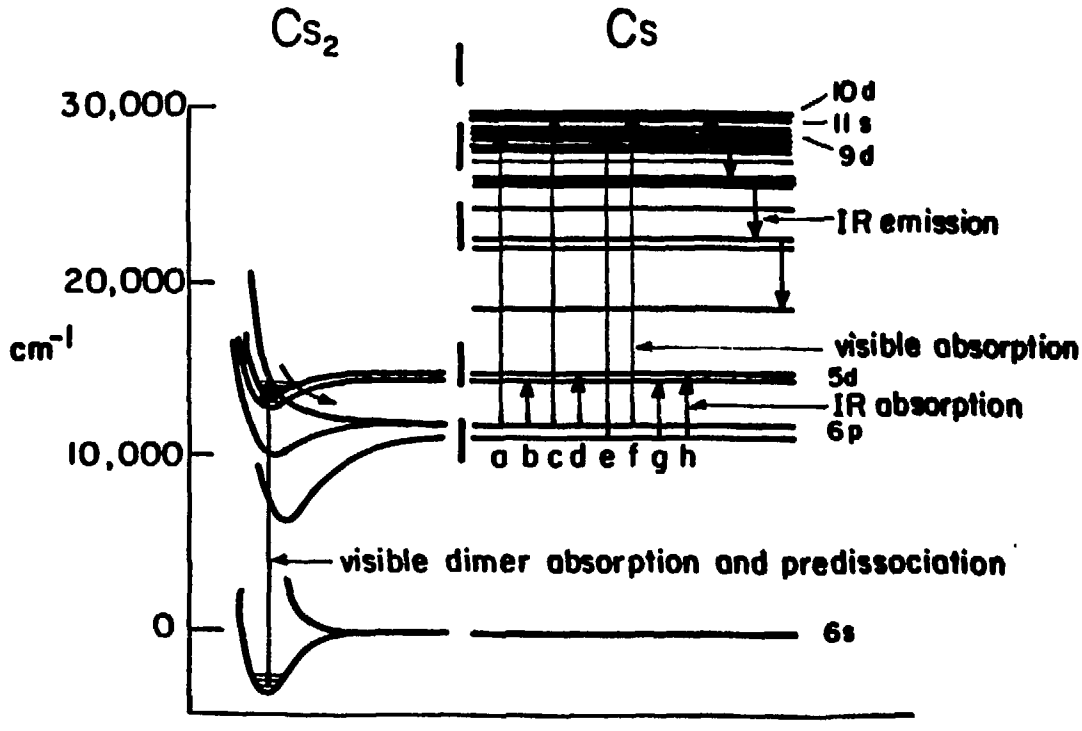
Cs2
Cs
30,000
20,000
10,000
0
cm-1
10d
11s
9d
IR emission
visible absorption
5d
IR absorption
6p
a b c d e f g h
visible dimer absorption and predissociation
6s

FIG. 3

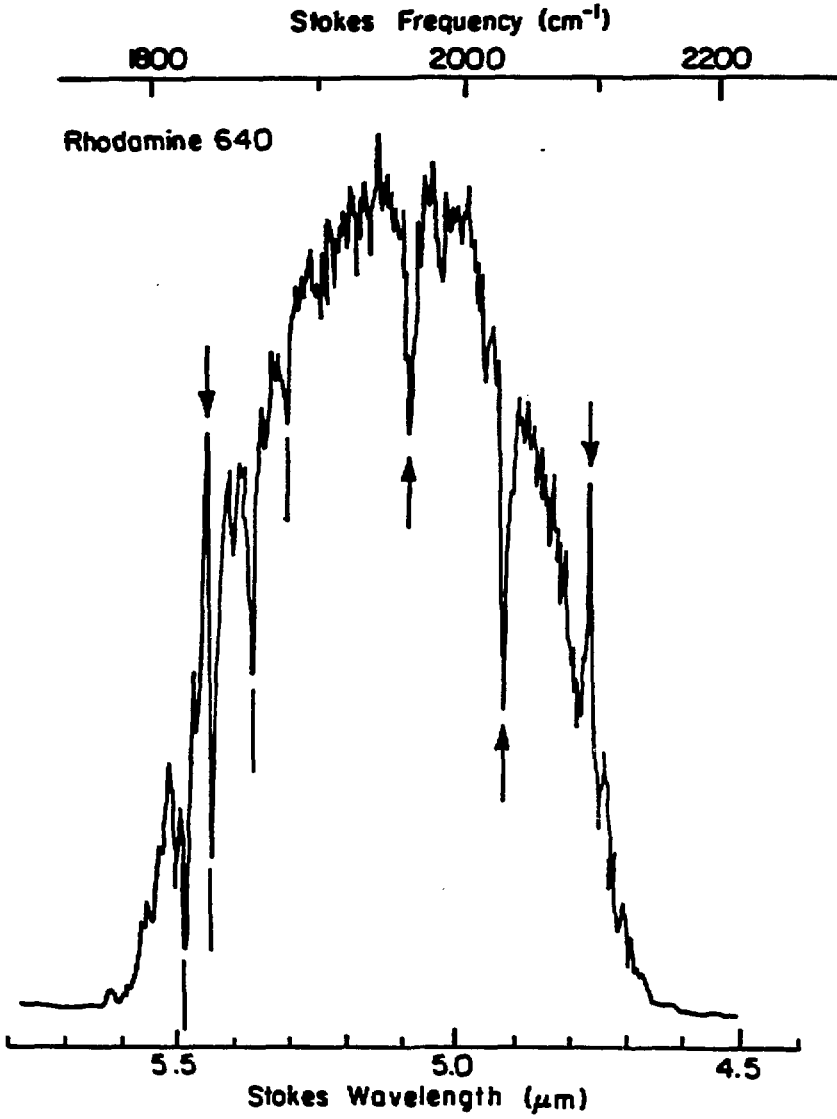
Stokes Frequency (cm⁻¹)
1800
2000
2200
Rhodamine 640
5.5
5.0
4.5
Stokes Wavelength (μm)

Fig. 4

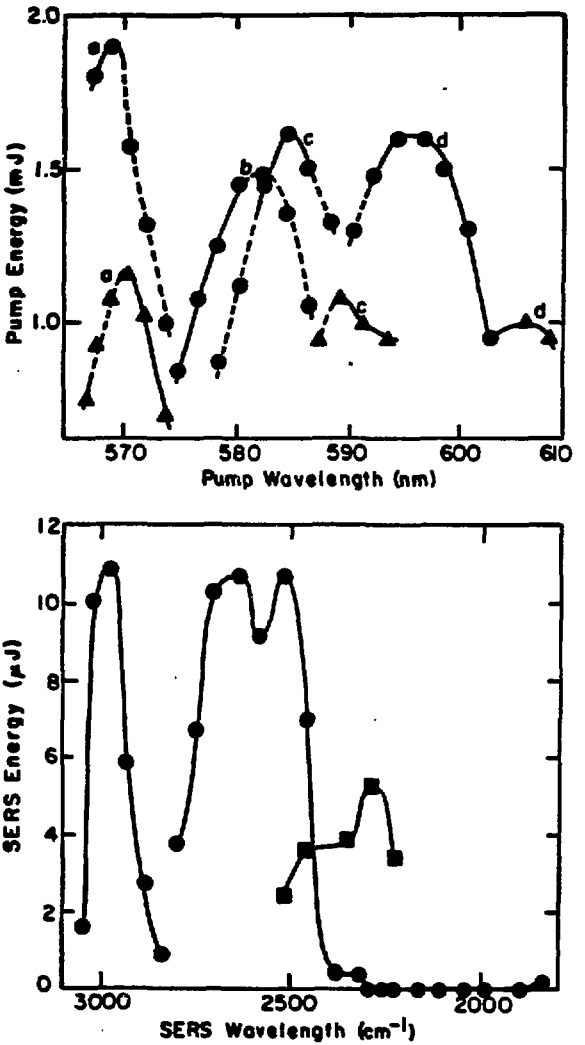
2.0
1.5
1.0
Pump Energy (mJ)
a
b
c
d
570
580
590
600
610
Pump Wavelength (nm)
12
10
8
6
4
2
0
SERS Energy (μJ)
3000
2500
2000
SERS Wavelength (cm⁻¹)

Fig. 5

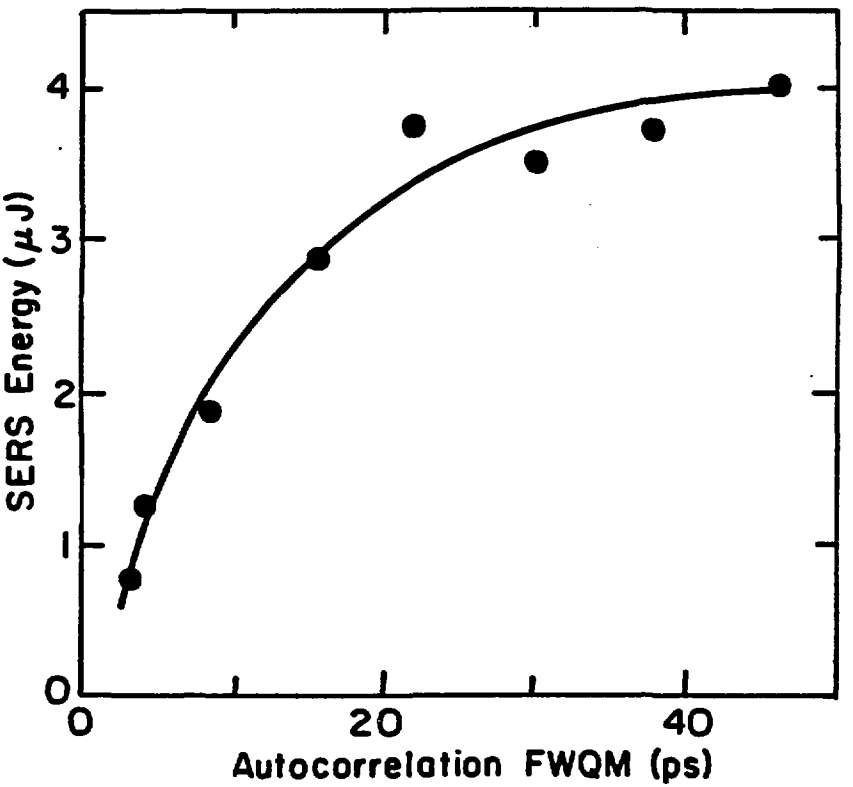

Fig. 6

CHAPTER IV

GENERATION OF PICOSECOND PULSES IN THE FAR-INFRARED BY THE DIFFERENCE FREQUENCY MIXING OF VISIBLE PULSES

The investigation of many dynamical processes in the far-infrared (FIR) require a source of intense, tunable, narrow bandwidth picosecond pulses. Recently there has been interest in the generation of picosecond pulses from free electron lasers,[3] but success has not yet been demonstrated in the FIR. Most other lasers operating directly in the FIR have little tunability, so work has centered on frequency shifting lasers operating in other spectral regions. Optical rectification has been used to generate broadband picosecond[1] and femtosecond[2] pulses, but with a broad bandwidth. A variety of frequency-shifting techniques have been successful in generating longer FIR pulses.[4,5] In particular, tunable nanosecond FIR pulses have been generated by the difference frequency mixing of two visible dye lasers.[6,7] The high peak power produced by the amplified synchronously-pumped dye laser (Chapter I) offers the potential of both extending this technique to the picosecond regime and also increasing its efficiency. Although the results of these experiments do not meet theoretical expectations, a valuable source of picosecond FIR was developed.

Two visible pulses, the first 1-2 ps long and the second 5 ns long, were mixed in a $LiNbO_3$ crystal to generate FIR pulses. Since mixing only occurred while both pulses were present, picosecond FIR was generated. The 0.2 mJ picosecond pulses at 589 nm were generated by the amplified, synchronously-pumped dye laser described in Chapter I. A

YAG-pumped dye laser (Quanta-Ray) produced the 20-mJ nanosecond pulses, which were tuned from 590-596 nm. The pulse-to-pulse energy fluctuations were ±10% for the picosecond pulses and ±6% for the nanosecond pulses. The YAG beam normally used to pump the third amplifier cell was split to pump both the nanosecond dye laser and the picosecond amplifier, thus insuring synchronization of the two pulses. This accounts for the low energy of the picosecond pulse (see Chapt. I). The two beams were superimposed in the $LiNbO_3$ crystal and focused slightly to give spot sizes of 0.6 mm and 1.2 mm for the picosecond and nanosecond beams respectively. Smaller spot sizes caused crystal damage. Note that the instantaneous nanosecond intensity (350 MW/cm^2) is much lower than the picosecond intensity (70 GW/cm^2).

Non-collinear phase-matching was achieved by the method of Yang, et al.[6] The two visible beams, as well as the FIR, were polarized along the optic axis of the $LiNbO_3$ to utilize the largest non-linear coefficient.[8] Since the FIR spectral band is below the optical phonon modes of the crystal, the FIR refractive index[9] (n = 5.5) is much larger than the visible index (n = 2.3). Therefore the phase-matching can be accomplished geometrically, without using birefringence. Tuning was achieved by changing both the angle between the visible beams (from 5 to 50 mrad) and the frequency of the nanosecond laser. An advantage of the phase-matching scheme used here over collinear phase matching is that the direction of the optic axis does not have to be changed as the FIR is tuned. Thus only one crystal was needed for the entire tuning range. Because the FIR was produced at a 68 degree angle from the visible beams, a corner of the 4-mm cubic crystal was removed to avoid total internal reflection and allow the FIR to exit.[6]

The FIR was produced with a significant divergence due to the f1 mrad convergence of the visible beams, the diffraction of the FIR, and the bandwidth of the picosecond pulse. This divergence was increased by refraction at the crystal surface to >1 srad. In order to collect this large solid angle, the small end of a Winston concentrator[10] was placed in contact with the exit face of the crystal. The concentrator collected and collimated the emerging FIR pulse, which then passed through frequency filters to a composite bolometer operated at 1.5 K. The bolometer was calibrated using blackbody sources at 77 and 300 K. A Michelson Fourier spectrometer was used to measure the spectrum of the FIR pulses.

Figure 1 shows the median collected FIR energy at frequencies from 20-200cm^{-1}. The energies were typically 3 nJ per pulse, which gave detector signals which were several orders of magnitude larger than detector noise. In these experiments, noise in the amplifying electronics and electrical pick-up from the lasers was significant, but better quality electronics can be obtained. The quantum efficiency for conversion of photons from the visible picosecond pulse to detected FIR photons varied from 0.1% to 0.3%. Surprisingly, there was no strong trend in the energy or the quantum efficiency as the frequency changed by a factor of ten. The variation in the amount of diffractive loss in the FIR should be large over this range. Furthermore, an optical phonon mode in $LiNbO_3$ at 252 cm^{-1} would be expected to strongly influence the quantum efficiency through changes in the FIR absorption and phonon resonance enhancement.[11,12]

The spectrum in Figure 2 shows that the FIR was generated in a narrow bandwidth at the frequency difference of the visible pulses. The

FIR bandwidth of <10 cm^{-1} was similar to that of the visible picosecond pulses. This bandwidth is consistent with a 1 ps FIR pulse. Since the crystal face is cut perpendicular to the FIR wavefront, the time required for the interaction region to propagate through the crystal does not broaden the FIR pulse. However, consideration of the transverse dimensions of the interaction region suggests that the actual FIR pulse length was closer to 10 ps.

The simple theory of parametric mixing predicts that photons from the high frequency picosecond pulse are split into photons at both the lower, nanosecond frequency and into FIR photons.[13] As long as the nanosecond intensity is low relative to the picosecond intensity, the FIR energy will depend exponentially on the picosecond intensity and linearly on the nanosecond intensity. If the mixing continues until the picosecond pulse is significantly converted, the process will saturate. The FIR energy will then depend linearly on the picosecond intensity and will be insensitive to the nanosecond intensity.

Experimentally, a small amount of FIR was generated, even when only the the picosecond pulse entered the crystal. At the same time, a small amount of visible light was observed to be shifted down in frequency from 0 to >300 cm^{-1}, but peaked near a shift of 150 cm^{-1}. This is interpreted to be parametric fluorescence resulting from the amplification of quantum noise.[14] Optical rectification may have also contributed to the FIR signal.[1,2] These observations indicate the strength of the non-linear interactions at the intensities used.

When both the nanosecond and the picosecond pulse were passed through the full 4-mm length of the crystal, the picosecond pulse was depleted by 35-50%. With the nanosecond pulse at full intensity, the

FIR energy was observed to depend linearly on the visible picosecond intensity for more than an order of magnitude above a threshold at 20 μJ. This threshold may represent the beginning of the saturated regime. Finally, the FIR was insensitive to the nanosecond pulse energy; when the nanosecond intensity was reduced by a factor of 7, the FIR intensity only dropped by a factor of 2, and the visible picosecond pulse was still strongly depleted. All these observations are consistent with a very strong non-linear interaction, leading to strongly saturated FIR generation.

However, strongly saturated mixing should lead to high quantum efficiencies. Even considering losses such as reflections at the crystal faces and FIR absorption[11] by the crystal, the observed quantum efficiencies were surprisingly low. Furthermore, strong pulse-to-pulse fluctuations in the FIR energy were observed, whereas saturated mixing should be quite stable. Figure 3 shows a histogram of these fluctuations. All pulses with energy greater than twice the median energy are shown in the cross-hatched bar at the right. Some pulses were observed with as much as five times the median pulse energy. Comparable fluctuations were not seen in the strong depletion of the optical picosecond pulse which occurred when FIR was being generated. Given the observed weak dependence of the FIR energy on the visible pulse energies, the FIR fluctuations cannot result from the small visible pulse fluctuations assuming smooth visible pulses of uniform length. Also, measurements of the transmission of the visible beams through a pinhole showed that wandering of the beams from pulse-to-pulse was not responsible for the fluctuations.

Both the low quantum efficiency and the large pulse-to-pulse

fluctuations are inconsistent with the simple theory of saturated mixing. Two of the possible explanations for this disagreement are:

1) The FIR was generated efficiently by a saturated process, but was then depleted by further non-linear processes. The fluctuations in these processes caused the fluctuations in the FIR and were responsible for the discrepancy between depleted picosecond energy and measured FIR energy. However, no reduction in the fluctuations was observed when the beam intensities were reduced.

2) The nanosecond pulse was not bandwidth limited, implying that it had significant amplitude modulation. Since the picosecond pulse was not long enough to average these fluctuations, it may have seen pulse-to-pulse intensity variations in the temporal overlap with the nanosecond pulse that were larger than are implied by the total pulse-to-pulse energy variations. Since the FIR energy was relatively insensitive to the nanosecond energy, these modulations would have to be very large.

Neither of these explanations is entirely satisfactory, but the presence of occasional high efficiency pulses can be seen as encouraging. Their presence implies that a fundamental limit to conversion efficiency has not yet been reached. If the source of these fluctuations can be understood, it may be possible to consistently generate FIR pulses with the efficiencies which are now seen only erratically. Even without this improvement however, the lack of picosecond FIR sources with comparable intensity and bandwidth make this technique a potentially valuable spectroscopic tool.

References

1. K. H. Yang, P. L. Richards, and Y. R. Shen, Appl. Phys. Lett. 19, 320 (1971); J. R. Morris and Y. R. Shen, Opt. Commun. 3, 81 (1971).
2. D. H. Auston, K. P. Cheung, J. A. Valdmanis, and D. A. Kleinman, Phys. Rev. Lett. 53, 1555 (1984).
3. E. D. Shaw and C. K. N. Patel, in Free Electron Generators of Coherent Radiation, edited by S. F. Jacobs, H. S. Pilloff, M. Sargent III, M. O. Scully, and R. Spitzer (Addison-Wesley, London, 1980), p. 665.
4. For examples see Nonlinear Infrared Generation, edited by Y. R. Shen (Springer-Verlag, New York, 1977).
5. J. M. Yarborough, S. S. Sussman, H. E. Purhoff, R. H. Pantell, and B. C. Johndon, Appl. Phys. Lett. 15, 102 (1969); M. A. Piestrup, R. N. Fleming, and R. H. Pantell, Appl. Phys. Lett. 26, 418 (1975).
6. K. H. Yang, J. R. Morris, P. L. Richards, and Y. R. Shen, Appl. Phys. Lett. 23, 669 (1973).
7. J. R. Morris and Y. R. Shen, Phys. Rev. A15, 1143 (1977).
8. M. Berg, A. L. Harris, J. K. Brown, and C. B. Harris, Opt. Lett. 9, 50 (1984).
9. I. P. Kaminow and W. D. Johnston, Phys. Rev. 160, 519 (1967).
10. A. S. Barker, Jr. and R. Loudon, Phys. Rev. 158, 433 (1967).
11. W. T. Welford and R. Winston, The Optics of Non-Imaging Concentrators (Academic Press, Inc., New York, 1978), pp. 47-68.
12. See for example, D. R. Bosomworth, Appl. Phys. Lett. 9, 330 (1966). Measurements by T. W. Kenny show the absorption coefficients to be a factor of 10 larger than Bosomworth's.

13. C. H. Henry and C. G. B. Garrett, Phys. Rev. 171, 1058 (1968).

14. N. Bloembergen, Non-linear Optics (W. A. Benjamin, Inc., Reading, Mass., 1965), Sec 4-4.

15. A. Yariv, Quantum Electronics (John Wiley and Sons, Inc., New York, 1975), Sec 17.7.

Figure Captions

Fig. 1. Total detected energy of the picosecond FIR pulse as a function of frequency. The quantum efficiency, G, for conversion from the visible to the FIR varies from 0.1% to 0.3%.

Fig. 2. Average spectrum of the FIR generated with the laser difference frequency centered at 70 cm^{-1}.

Fig. 3. Distribution of the pulse-to-pulse fluctuations of the FIR energy. The cross-hatched region represents all of the pulses with more than twice the median energy.

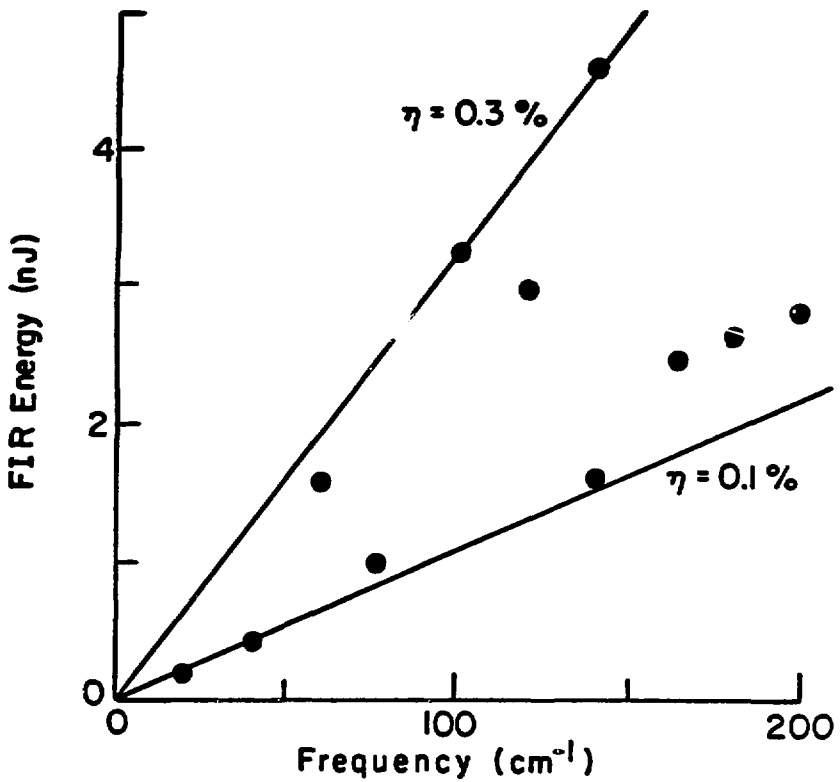

Fig. 1

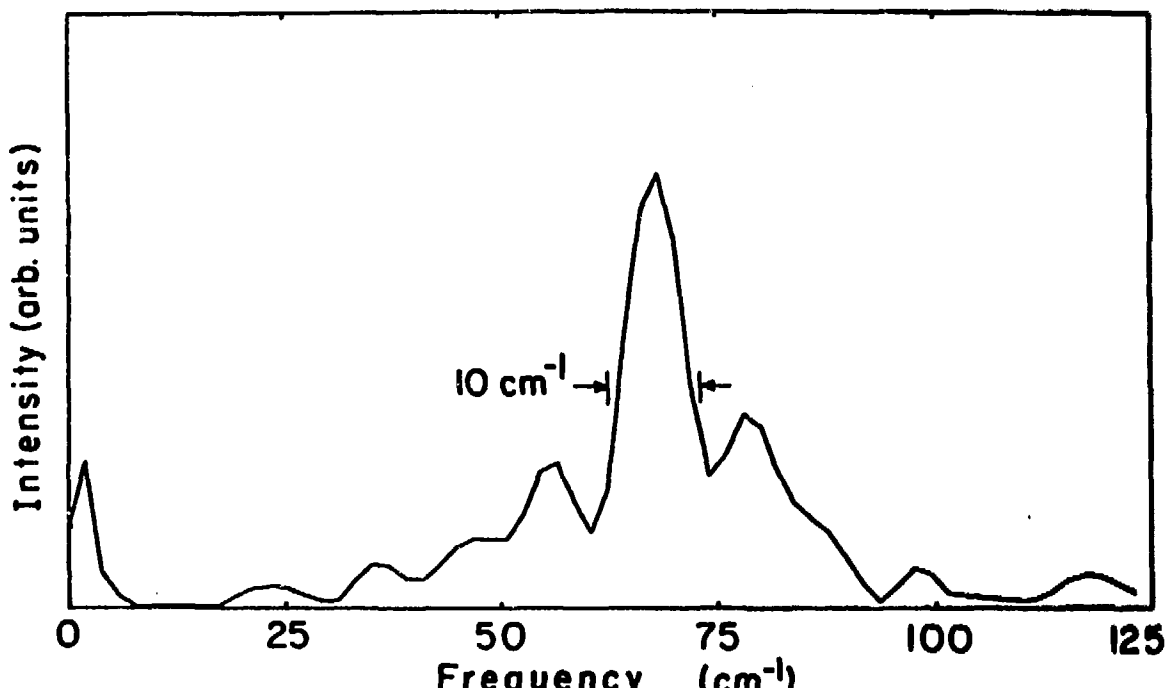

Fig. 2

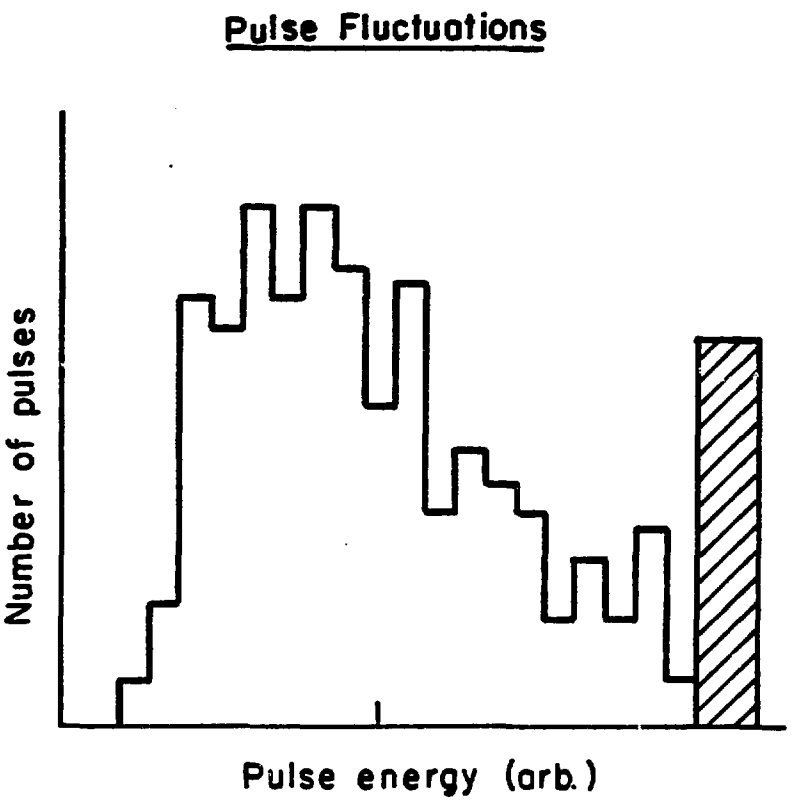

Fig. 3